

AN ABSTRACT OF THE THESIS OF

Xiao-Yan Chen for the degree of Doctor of Philosophy in  
Physics presented on June 8, 1988.

Title: Analyzing Powers and Cross Sections of Inclusive Polarized  
Proton Scattering on  $^{208}\text{Pb}$

Redacted for Privacy

Abstract approved: \_\_\_\_\_  
L. Wayne Swenson

Inclusive polarized proton-nucleus scattering at 290 and 500 MeV was performed using a  $^{208}\text{Pb}$ (51 mg/cm<sup>2</sup>) target. A broad range (0-250 MeV) of excitation energy has been studied over the 4° - 27° angular range. The measured analyzing power and cross section of the continuum are compared with the recent DWIA model calculations. The analyzing power and cross section of low-lying states are compared with the DWBA model calculation. The cross section in the continuum region is found to be dominated by single-step quasifree scattering. The analyzing power angular distributions of continuum peaks support RIA model predictions, and indicate the presence of relativistic medium effects.

Analyzing Powers and Cross Sections of  
Inclusive Polarized Proton Scattering on  $^{208}\text{Pb}$

by

Xiao-Yan Chen

A THESIS

submitted to

Oregon State University

in partial fulfillment of  
the requirements for the  
degree of

Doctor of Philosophy

Completed June 8, 1988

Commencement June 1989

APPROVED:

Redacted for Privacy

\_\_\_\_\_  
Professor of Physics in charge of major

Redacted for Privacy

\_\_\_\_\_  
Head of department of Physics

Redacted for Privacy

\_\_\_\_\_  
Dean of Graduate School

Date thesis is presented June 8, 1988

Typed by Xiao-Yan Chen for Xiao – Yan Chen

## Table of Contents

<u>Chapter</u>	<u>Page</u>
<b>1 Introduction</b>	<b>1</b>
<b>2 Theory</b>	<b>8</b>
2.1 Surface Response Model . . . . .	9
2.2 RIA Model . . . . .	11
2.3 Quasifree Kinematics . . . . .	12
2.4 Schrödinger optical Model . . . . .	13
2.5 Dirac Optical Model . . . . .	16
<b>3 Experimental</b>	<b>18</b>
3.1 The In-beam Polarimeter . . . . .	20
3.2 Medium Resolution Spectrometer . . . . .	23
3.3 The MRS Detector . . . . .	26
3.4 The MRS Trigger . . . . .	27
3.5 Data Stream . . . . .	28
3.6 Dispersion Matching Technique . . . . .	31
3.7 Experiment 319 . . . . .	33
<b>4 Data Analysis</b>	<b>35</b>
4.1 Data Replay . . . . .	35
4.2 Overall MRS Chamber Efficiency . . . . .	36
4.3 Normalizations . . . . .	42
4.4 Cross Sections and $A_y$ . . . . .	45

4.5	Continuum . . . . .	47
4.6	Low-lying states . . . . .	49
<b>5</b>	<b>Results and Discussions</b>	<b>52</b>
5.1	The Continuum at $E_p = 290$ MeV . . . . .	55
5.2	The continuum at $E_p = 500$ MeV . . . . .	72
5.3	Discussion of Continuum Results . . . . .	88
5.4	The Low-lying States . . . . .	90
5.5	Conclusion . . . . .	108
	<b>Bibliography</b>	<b>122</b>

## List of Figures

<u>Figure</u>	<u>Page</u>
1    An idealized proton scattering experiment . . . . .	2
2    A typical spectrum from position sensitive detector. . . . .	3
3    Quasifree peak kinematics for $^{208}\text{Pb}$ at 200 MeV . . . . .	14
4    The general layout of TRIUMF . . . . .	19
5    A schematic of in-beam polarimeter. . . . .	21
6    The layout of medium resolution spectrometer . . . . .	24
7    The schematic of medium resolution spectrometer . . . . .	25
8    The schematic of the MRS triggers . . . . .	29
9    The principle of dispersion matching . . . . .	32
10   A 2-D histogram for particle identifications. . . . .	37
11   A spectrum without aberration corrections. . . . .	38
12   A spectrum after aberration corrections. . . . .	39
13   A 2-D spectrum of $\theta_{pc}$ vs focal plane XFK. . . . .	40
14   A spectrum before channel rebin. . . . .	43
15   A spectrum after channel rebin. . . . .	44
16   Some spectra from $E_p=290$ MeV data. . . . .	48
17   Fitting of low-lying states. . . . .	51
18   Normalization check using $\text{CH}_2$ at $E_p=500$ MEV . . . . .	53
19   Normalization check using elastic $p\text{-}^{208}\text{Pb}$ at $E_p = 500$ MeV . . . .	54
20   Normalization check using elastic $p\text{-}^{208}\text{Pb}$ at $E_p = 300$ MeV . . . .	56
21   Continuum spectrum of $\theta_{Lab}=4^\circ$ , $E_p=290$ MeV . . . . .	59
22   Continuum spectrum of $\theta_{Lab}=6^\circ$ , $E_p=290$ MeV . . . . .	60

23	Continuum spectrum of $\theta_{Lab}=8^\circ$ , $E_p=290$ MeV . . . . .	61
24	Continuum spectrum of $\theta_{Lab}=10^\circ$ , $E_p=290$ MeV . . . . .	62
25	Continuum spectrum of $\theta_{Lab}=12^\circ$ , $E_p=290$ MeV . . . . .	63
26	Continuum spectrum of $\theta_{Lab}=14^\circ$ , $E_p=290$ MeV . . . . .	64
27	Continuum spectrum of $\theta_{Lab}=18^\circ$ , $E_p=290$ MeV . . . . .	65
28	Continuum spectrum of $\theta_{Lab}=22^\circ$ , $E_p=290$ MeV . . . . .	66
29	Continuum spectrum of $\theta_{Lab}=26^\circ$ , $E_p=290$ MeV . . . . .	67
30	The $A_y$ vs $\theta$ of quasifree peak at $E_p=290$ MeV. . . . .	68
31	The spin up and spin down spectra of $4^\circ$ at $E_p=290$ MeV . . . . .	69
32	Representative data and surface response calculations at 290 MeV.	71
33	The continuum spectra of $5^\circ$ , at $E_p=500$ MeV. . . . .	74
34	The continuum spectra of $7^\circ$ , at $E_p=500$ MeV. . . . .	75
35	The continuum spectra of $9^\circ$ , at $E_p=500$ MeV. . . . .	76
36	The continuum spectra of $11^\circ$ , at $E_p=500$ MeV. . . . .	77
37	The continuum spectra of $13^\circ$ , at $E_p=500$ MeV. . . . .	78
38	The continuum spectra of $17^\circ$ , at $E_p=500$ MeV. . . . .	79
39	The continuum spectra of $19^\circ$ , at $E_p=500$ MeV. . . . .	80
40	The continuum spectra of $21^\circ$ , at $E_p=500$ MeV. . . . .	81
41	The continuum spectra of $23^\circ$ , at $E_p=500$ MeV. . . . .	82
42	The continuum spectra of $25^\circ$ , at $E_p=500$ MeV. . . . .	83
43	The continuum spectra of $27^\circ$ , at $E_p=500$ MeV. . . . .	84
44	The $A_y(\theta_L)$ vs $\theta$ of quasifree peaks at 500 MeV. . . . .	86
45	Representative data and surface response calculation at 500 MeV.	87
46	Elastic Scattering Data and NOPM Calculations at 300-MeV. . . .	93
47	Elastic Scattering Data and NOPM Calculations at 500-MeV. . . .	94
48	Elastic scattering data and ROPM calculations of 300-MeV. . . . .	95
49	Elastic scattering data and ROPM calculations of 500-MeV. . . . .	96

50	$3^-$ (2.61 MeV) data and NOPM calculations, at $E_p = 290$ MeV . .	98
51	$5_1^-$ (3.20 MeV) data and NOPM calculations, at $E_p = 290$ MeV . .	99
52	$5_2^-$ (3.71 MeV) data and NOPM calculations, at $E_p = 290$ MeV . . .	100
53	$2^+$ (4.09 MeV) data and NOPM calculations, at $E_p = 290$ MeV . .	101
54	$4^+$ (4.32 MeV) data and NOPM calculations, at $E_p = 290$ MeV . .	102
55	$3^-$ (2.61 MeV) data and NOPM calculations, at $E_p = 500$ MeV . . .	103
56	$5_1^-$ (3.20 MeV) data and NOPM calculations, at $E_p = 500$ MeV . . .	104
57	$5_2^-$ (3.71 MeV) data and NOPM calculations, at $E_p = 500$ MeV . . .	105
58	$2^+$ (4.09 MeV) data and NOPM calculations, at $E_p = 500$ MeV . .	106
59	$4^+$ (4.32 MeV) data and NOPM calculations, at $E_p = 500$ MeV . . .	107
60	$3^-$ (2.61 MeV) data and ROPM calculations, at $E_p = 290$ MeV . .	109
61	$5_1^-$ (3.20 MeV) data and ROPM calculations, at $E_p = 290$ MeV . .	110
62	$5_2^-$ (3.71 MeV) data and ROPM calculations, at $E_p = 290$ MeV . .	111
63	$2^+$ (4.09 MeV) data and ROPM calculations, at $E_p = 290$ MeV . .	112
64	$4^+$ (4.32 MeV) data and ROPM calculations, at $E_p = 290$ MeV . .	113
65	$3^-$ (2.61 MeV) data and ROPM calculations, at $E_p = 500$ MeV . .	114
66	$5_1^-$ (3.20 MeV) data and ROPM calculations, at $E_p = 500$ MeV . .	115
67	$5_2^-$ (3.71 MeV) data and ROPM calculations, at $E_p = 500$ MeV . .	116
68	$2^+$ (4.09 MeV) data and ROPM calculations, at $E_p = 500$ MeV . .	117
69	$4^+$ (4.32 MeV) data and ROPM calculations, at $E_p = 500$ MeV . .	118



## List of Tables

<u>Table</u>		<u>Page</u>
1	The focal plane response to MRS at $E_p=500$ MeV. . . . .	58
2	Quasifree peak positions vs $\theta_{Lab}$ at $E_p=290$ MeV. . . . .	58
3	The renormalization of surface response calculations to the data at 290 MeV. . . . .	73
4	Quasifree peak positions vs $\theta_L(^{\circ})$ at $E_p=500$ MeV. . . . .	73
5	Renormalization factor of surface response calculations to the data at 500 MeV. . . . .	92
6	Proton + $^{208}\text{Pb}$ Non-relativistic Optical Model Parameters. . . . .	92
7	Proton + $^{208}\text{Pb}$ Relativistic Optical Model Parameters. . . . .	121

# Analyzing Powers and Cross Sections of Inclusive Polarized Proton Scattering on $^{208}\text{Pb}$

## 1 Introduction

A proton scattering experiment can be idealized as in Figure 1.  $E_i$  is the incident proton energy and  $E_f$  is the final scattered proton energy. Polarized protons from the accelerator bombard a thin target under study. The majority of the protons will be un-scattered, pass through the target and be intercepted by the beam dump. A small fraction of the incident protons will interact with target nuclei and be scattered. A magnetic dipole spectrometer in the scattering plane intercepts scattered protons at scattering angle  $\theta$  within solid angle  $\Delta\Omega$ . These scattered protons are bent through radii proportional to their momenta by the magnetic dipole. The scattered protons with different momentum are therefore spatially separated and subsequently detected by the position sensitive detector at the exit of the magnetic dipole spectrometer. A typical spectrum from the position sensitive detector is shown in Figure 2. The spectrum can later be converted into a momentum spectrum or energy spectrum.

According to the recent literature [1], the energy spectrum of the inclusive protons scattered in our present study can be sub-divided into four broad categories in view of their excitation energies,  $E_x$ : 1) Elastic scattering, which is located at  $E_x = 0$ , 2) Inelastic scattering to bound states, which are usually peaked in the range  $0 < E_x < 10$  MeV. They are discrete, well separated nuclear states with definite angular momenta and parities. 3) Inelastic scattering to the continuum which forms the majority of the total reaction production in the spectrum, and 4) inelastic scattering to the giant resonance states, which are located

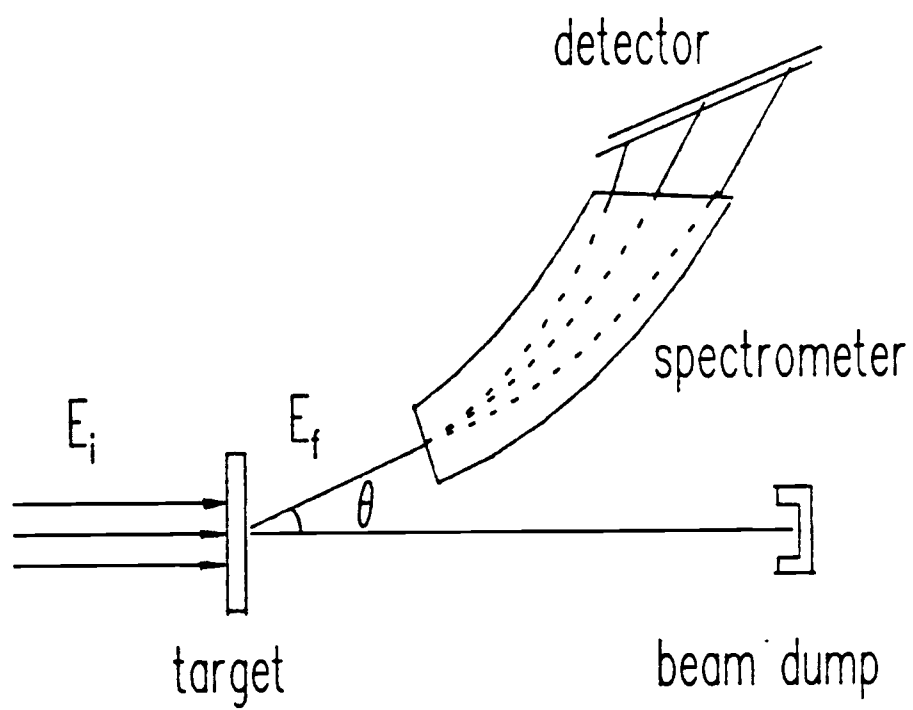


Figure 1: An idealized proton scattering experiment

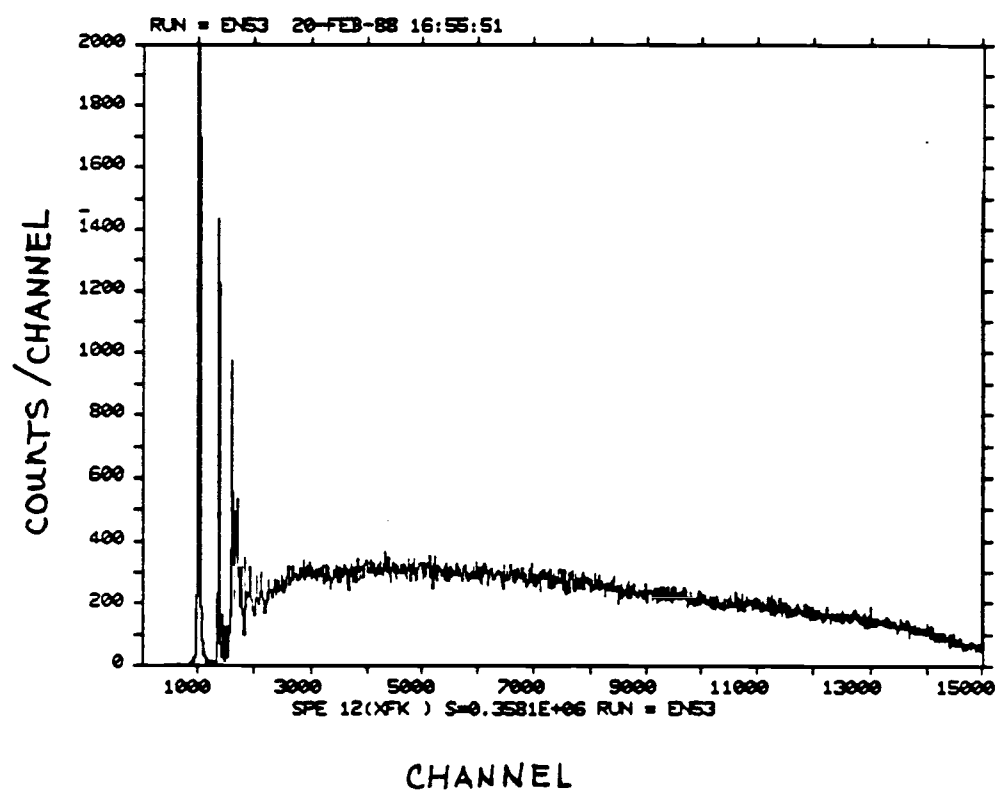


Figure 2: A typical spectrum from position sensitive detector.

around 9 MeV to 25 MeV depending on the target and observed as broad collective nuclear structures above the continuum in the spectrum.

In the first 2 categories, the spectrum is determined by the detailed nuclear structure effects, and the reaction leading to these events is dominated by single-scattering. This low excitation energy region has been considered important in nuclear structure studies because simple relationships between initial and final states of the target are not lost by passage through complicated intermediate states, and hence are reflected in the observed spectra. In category 3), the reaction mechanism is recently believed to be dominated by single-step quasifree scattering with a mixture of multiple-scattering.[2],[3]. In category 4), the spectrum is determined by collective nuclear properties. It is found to be rich in information, but due to the presence of many broad and overlapping resonances, the search for the higher angular momentum resonances faces difficulties. [4].

Over the past few years, measurements were made at TRIUMF, LAMPF, and SACLAY on elastic and inelastic scattering from medium and heavy targets such as  $^{40}\text{Ca}$  and  $^{208}\text{Pb}$  at energies of 200 MeV to 1000 MeV. Recent experimental developments have also enabled measurement of complete sets of spin observables for elastic scattering, as summarized in Ref.[5] and [6]. From the above mentioned experiments, the angular distributions of differential cross section, analyzing power and the spin rotation were obtained up to  $50^\circ$  in the center of mass. In the region of inelastic scattering to the low lying states, measurements of cross sections were also made in the energy range 35 MeV to 800 MeV using  $^{208}\text{Pb}$ ,  $^{40}\text{Ca}$  and  $^{58}\text{Ni}$  as target nuclei as summarized in Ref. [7] and [8], not many data exit for more spin sensitive quantities, for example analyzing powers and spin observables. In the past ten years, the inclusive electron and proton scattering experiments on nuclei reveal a broad peak in the continuum spectrum, approximately 100 MeV wide, which corresponds to a quasifree processes in which an individual nucleon has been

directly knocked out of the nucleus by the incoming projectiles as indicated in [9], [10] and [11]. Only in the recent years, has the development of intense polarized proton beams enabled measurements of spin observables over a large momentum transfer region with reasonable beam time allocations. Using polarized protons of 200 MeV, a recent experiment [12] found that the shape and magnitude of the analyzing power angular distribution  $A_y(\theta)$  for the inclusive quasifree peak to be similar to that of the free nucleon-nucleon scattering over the angular range of  $5^\circ$  to  $14^\circ$ . Since the experiment was giant resonance oriented, high momentum transfer data were not available. There are no existing data on  $A_y(\theta)$  angular distributions for the quasifree peak over a broad angular range including high angles. It is also of interest to see if there is any significant deviation of the  $A_y(\theta)$  angular distributions from free NN scattering at the quasifree peak for various proton bombarding energies.

Due to the lack of a fundamental theory of strong interactions, proton scattering is usually described by various models. The angular distributions of differential cross sections and analyzing powers of the elastic scattering have been traditionally well explained by optical model in Schrödinger approach with relativistic kinematics. Recent development of optical models in the Dirac approach has also offered a good alternative to describe cross sections and analyzing powers [13]. Based on the Schrödinger approach to optical model, the low lying states were reported to be reasonably reproduced [7]. There have been very few reported applications of the Dirac optical model to low lying states. New microscopic models using non-relativistic and relativistic impulse approximations have been successfully used to describe cross sections, analyzing powers and spin observables of elastic scattering in another fashion; see Ref.[6]. Using the simplified assumption of a nucleon-nucleon interaction in the nuclear medium, including Pauli blocking correction

and Fermi motion averaging as well as some other medium modifications, relativistic and non-relativistic impulse approximations have been used to describe quasifree inelastic scattering (Ref.[3], [2] and [14]). These calculations [3] show that the spin observables exhibit a sensitivity to relativistic effects and the cross sections are sensitive to medium effects. Specific to the analyzing power, the relativistic impulse approximation predicts the quasifree values to decrease for large scattering angles due to the relativistic medium effects, while the non-relativistic prediction is that it is the same as the free NN value.

This dissertation deals with inelastic scattering to the bound states and inelastic scattering to the continuum. In July 1986, an experiment on inclusive proton scattering was carried out using the 290-MeV polarized beam at TRIUMF on a  $^{208}\text{Pb}$  target. The cross sections and the analyzing powers of the continuum were obtained over the angular range of  $4^\circ$  to  $26^\circ$ , for excitation energies extending up to 180 MeV. Inelastic scattering data to the low-lying states were also obtained over the same angular range at the time. In July 1987, the second phase of the inclusive proton scattering experiment on the same target was undertaken using 500 MeV polarized protons. The cross sections and the analyzing powers were obtained at angles of  $5^\circ$  to  $27^\circ$ , while the excitation energy covered extended up to 250 MeV. Cross sections and analyzing powers of the low-lying states were also obtained over the same angular range.

This dissertation attempts to compare the experimental results of the continuum measurements at  $E_p = 290$  MeV and  $E_p = 500$  MeV with the recent relativistic and non-relativistic impulse approximation predictions. The analyzing power angular distributions at  $E_p = 290$  MeV and 500 MeV are compared with the free NN interaction (Fermi motion averaged) and the NN interaction in the relativistic medium. The presence of relativistic medium effects will be manifest by deviations from the free NN interaction. If there are no relativistic medium

effects, the results of the 500-MeV data (which are less influenced by multiple scattering than the 290 MeV data) should be closer to the free NN calculations; Any relativistic effects that reflected on continuum data should in one way or another be reflected in the low-lying states as well, thus we will also compare the data of low-lying states with the phenomenological relativistic and non-relativistic optical model calculations. The theoretical formalism is in chapter 2, details relating to the experiments are described in chapter 3, details regarding to the data analyses are in chapter 4. The final results and the discussions are in chapter 5.



## 2 Theory

Scattering of a proton from the target nucleus is essentially a many-body problem; it can be viewed as the scattering to a system of bound nucleons. The standard way of dealing with this kind of problem is to approximate the interactions between the projectile and the many-body nucleons with a two-body interaction and treat the problem either microscopically or macroscopically, by solving the two-body problem either in the context of non-relativistic or relativistic dynamics. In the microscopic method, the two-body interaction refers to the projectile and the individual target nucleons. The interaction between the projectile and the target nucleus is the sum of the two body interactions. The attractive features of the microscopic approach appear in the intermediate energy range of 200 MeV to 1 GeV, in which two nucleons inside a nucleus scatter approximately as if they were in free space, while the presence of the other nucleons has little effect. Therefore, the individual projectile-nucleon scattering can be approximately described by free nucleon-nucleon scattering amplitude. This is called the impulse approximation. The free nucleon-nucleon scattering amplitude can be solved with accuracy. However, difficulties arise especially at the low momentum transfer or low excitation energy where the use of the impulse approximation is questionable. In the macroscopic method, the two-body interaction is between the projectile and the whole nucleus. The nucleus is phenomenologically replaced by an optical body which is characterized by the average optical potentials. The average optical potentials have no relationships among themselves and depend solely on experimental elastic scattering data. Therefore, the macroscopic approach is suitable for describing the inelastic scattering to the low-lying states. Discrepancies might appear with this approach when describing the inelastic scattering in the region of high excitation

energy or large momentum transfer. The method depends critically on determination of the optical potential parameters without ambiguity from fits to elastic scattering data.

Our data cover the regions where the microscopic models and macroscopic models perform at their best. The models described in the following sections are to be compared with the data.

## 2.1 Surface Response Model

This is a recent microscopic model applying non-relativistic impulse approximation to inclusive quasifree scattering. The theory is based on the distorted wave impulse approximation which allows the nucleon-nucleon cross section to be factorized from the nuclear response. In the surface response model, the double differential cross section for inelastic proton-nucleus scattering as developed by Bertsch, Scholten and Esbensen [2,20] has the form

$$\frac{d^2\sigma}{d\Omega dE} = N_{\text{eff}} \sum_{T,S} \left[ \frac{d\sigma_{NN}}{d\Omega} \right]_{T,S} S_{T,S}(q, E) \quad (1)$$

where  $\left[ \frac{d\sigma_{NN}}{d\Omega} \right]_{T,S}$  is the free nucleon-nucleon scattering cross section in different isospin-spin channels, and is calculated from the accurate free nucleon-nucleon scattering amplitudes as indicated in ref.[2].  $N_{\text{eff}}$  is the effective number of target particles participating in the proton-nucleus scattering, and is determined by Glauber theory for single scattering. To give a rough idea of the value of  $N_{\text{eff}}$  for  $^{208}\text{Pb}$ , it is of the order of 25 out of 208 nucleons. The surface response functions  $S_{T,S}(q, E)$  are functions of the momentum transfer  $q$  and the excitation energy  $E$ . The surface response functions are generated by the scattering operator and the wavefunctions that are satisfied by the requirement of finite nuclear matter and

the Glauber theory. The wavefunctions are eigenstates of the potential well

$$V = \frac{V_0}{1 + e^{z/a_0}} \quad (2)$$

in which  $V_0 = -45$  MeV and  $a_0 = 0.75$  fm are chosen according to the optical potentials for heavy nuclei [2]. The finite nuclear size requirement is taken care of by a semi-infinite nuclear matter approximation. The scattering operator is

$$O(q, r) = \frac{e^{iq \cdot r}}{(1 + e^{(z_0 - z)/a_0})^{1/2}} \quad (3)$$

for single scattering. The cutoff function in the scattering operator is consistent with the  $N_{\text{eff}}$  calculations from Glauber theory. Finally, the Pauli blocking corrections are applied to the calculations. The medium corrections of the nucleon-nucleon scattering in the nuclear medium are reflected in the  $N_{\text{eff}}$  and  $S_{T,S}(q, E)$  calculations.

The calculation of the effective analyzing power for the isospin-spin channels can be easily extended from the technique used to calculate the cross section. The effective analyzing power is found to have the following form:

$$\bar{A}_y = \frac{\sum_{T,S} S(T, S) I_0(T, S) A_y(T, S)}{\sum_{T,S} S(T, S) I_0(T, S)} \quad (4)$$

in which  $I_0(T, S)$  is the differential cross section and  $A_y(T, S)$  is the analyzing power of free nucleon-nucleon scattering in isospin-spin channels, which can be calculated from nucleon-nucleon scattering amplitude in free space.  $S(T, S)$  is the surface response functions in isospin-spin channels, and is actually independent

of the T and S in the case of the free surface response (without considering the residual interactions), see ref. [2]. We use the free surface response. As one can see from the equation 4, the medium corrections on the effective analyzing power are eventually canceled out. The analyzing power is therefore expected to be similar to the free nucleon-nucleon scattering.

## 2.2 RIA Model

A relativistic impulse approximation version of the quasifree scattering to the continuum has been developed by Horowitz and Iqbal [3]. This is the most recent model using a microscopic Dirac approach for studying inelastic proton scattering. The single proton-nucleus scattering, described by Dirac nucleon-nucleon scattering in the medium is investigated near the maximum of the quasifree peak in the continuum. In this model, spin observables near the quasifree peaks rather than the cross sections are studied to avoid some of the complicated distortions [3].

In a relativistic impulse approach the nucleon-nucleon interaction depends on the four-component Dirac wave functions. The lower components of these wave functions are said to be enhanced in the medium. The model characterizes the enhancement by an effective nucleon mass  $m^*$ ; the two nucleon scattering amplitude is then changed from  $K(m)$  for nucleon-nucleon interaction in free space into  $K(m^*)$  for nucleon-nucleon scattering in the medium as:

$$K(m^*) = 2ik_c \bar{U}(1', m^*) \bar{U}(2', m^*) \hat{F} U(1, m^*) U(2, m^*) \quad (5)$$

where  $\hat{F}$  is the  $4 \times 4$  matrix of interaction,  $U$  is the spinor in the space of two nucleons.  $1(1')$  describes the spin and momentum of the incoming(outgoing) first particle,  $k_c$  is the momentum in the two-body center of mass frame. Finally,

Fermi momentum averaging and Pauli blocking corrections are included in the calculations. The model calculates the spin observables under the following representation of the nucleon-nucleon scattering amplitude:

$$K(m^*) = \frac{1}{2}[a + b + (a - b)\sigma_{1n}\sigma_{2n} + (c + d)\sigma_{1m}\sigma_{2m} + (c - d)\sigma_{1l}\sigma_{2l} + e(\sigma_{1n} + \sigma_{2n})] \quad (6)$$

An evaluation is performed in between eqs. (5) and (6) to obtain  $a$ ,  $b$ ,  $c$ ,  $d$ ,  $e$ . It is then a simple matter to calculate spin observables for quasifree scattering. The analyzing power is, for example,

$$A_y = \frac{\text{Re}(a^*e)}{\frac{d\sigma}{d\Omega}} \quad (7)$$

and the differential cross section is

$$\frac{d\sigma}{d\Omega} = \frac{1}{2}(a^*a + b^*b + c^*c + d^*d + e^*e) \quad (8)$$

The important  $m^*$  is calculated using the transmission probability weighted average density, while the transmission probability is calculated from the Eikonal formalism in Dirac fashion. Details are in ref. [3].

### 2.3 Quasifree Kinematics

The position, in excitation energy, of the quasi-elastic peak is found to follow free NN kinematics closely. However, an improved phenomenological representation may be obtained by including binding corrections due to the nuclear medium. In this prescription, the centroid of the quasifree scattering in excitation energy is

given by

$$E_{x0} = T_0 - \left[ \frac{(T_0 + V_0 - B)\cos^2\theta}{1 + \frac{(T_0 + V_0)}{2mc^2}\sin^2\theta} - V_0 \right] \quad (9)$$

where  $T_0$  is the kinetic energy of the incident proton,  $V_0$  is as the average nuclear well depth (20 MeV for  $^{208}\text{Pb}$  target), and  $B$  represents the average nuclear binding energy (9 MeV for  $^{208}\text{Pb}$  target). This phenomenological approach was found to be in good agreement with quasifree peak positions observed in a study of  $^{208}\text{Pb}(p, p')$  at 200 MeV [12], as shown in Figure 3.

## 2.4 Schrödinger Optical Model

The spherical optical potential for nucleon-nucleon scattering has the following conventional form:

$$U(r) = V_c - V_0 f(r, R_0, a_0) - iW f(r, R_i, a_i) + \left( \frac{\hbar}{m_\pi c} \right)^2 \frac{1}{r} \frac{\partial}{\partial r} \times \\ [V_{so} f(r, R_{s1}, a_{s1}) + iW_{so} f(r, R_{s2}, a_{s2})] \vec{\sigma} \cdot \vec{L} \quad (10)$$

where  $V_c$  is the Coulomb potential,  $V_0$  and  $W$  are the central real and imaginary potentials, and  $V_{so}$  and  $W_{so}$  are the real and imaginary spin-orbit terms. The radial dependence of the nuclear potentials is given by Woods-Saxon functions, which have the form

$$f(r, R, a) = \frac{1}{(1 + e^{(r-R)/a})} \quad (11)$$

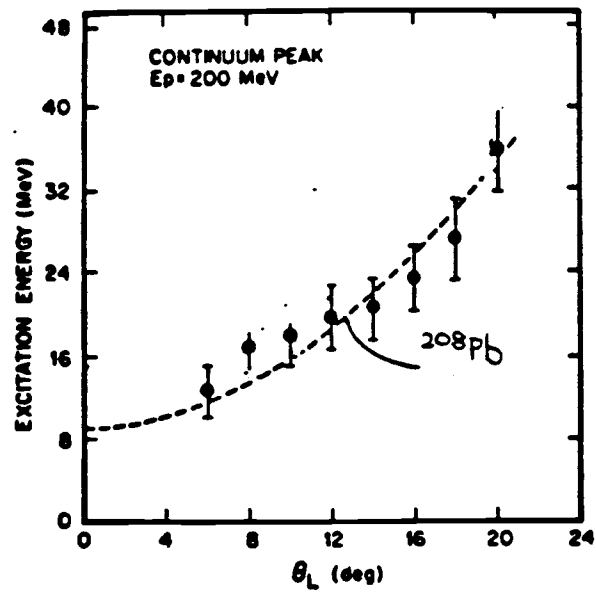


Figure 3: Quasifree peak kinematics for  $^{208}\text{Pb}$  at 200 MeV

To obtain correct optical potentials, twelve parameters from central real and imaginary , and spin-orbit real and imaginary potentials are adjusted to fit the elastic scattering data.

The inelastic scattering to low-lying collective nuclear states is usually described in terms of the deformation of optical potential. The optical potentials are deformed according to the surface deformation

$$R = R_0[1 + \sum_{LM} \alpha_{LM} Y_L^M(\theta, \phi)] \quad (12)$$

The deformed potentials are calculated using the first order Taylor expansion in the spherical coordinates. The transition multipole moments of the deformed parts for each of the real and imaginary optical potential terms have the form

$$U_L(r) = \beta_L(2L + 1)^{-\frac{1}{2}} R \frac{dU(r - R)}{dr} \quad (13)$$

where  $\beta_L$  is the deformation parameter of the optical potential. The deformation lengths ( $\beta R$ ) for all the potential terms are kept the same to ensure the same nuclear deformations, i.e.

$$\beta_0 R_0 = \beta_1 R_1 = \beta_{s1} R_{s1} = \beta_{s2} R_{s2} \quad (14)$$

Observables such as differential cross sections and analyzing powers for transitions to low-lying states are usually calculated using the deformed potentials in Distorted Wave Born Approximation (DWBA) or coupled channel approximation. If the channel coupling is weak so that no further adjustment is needed in the optical potentials, simple DWBA may be used to calculate the differential cross



sections  $(d\sigma/d\Omega)_L$ . Then for each excited low-lying state, the deformation length is extracted from the data according to:

$$(\beta_L R)^2 = (\beta_L R)_{DWBA}^2 \left( \frac{d\sigma}{d\Omega} \right)_{\text{measured}} / \left( \frac{d\sigma}{d\Omega} \right)_L \quad (15)$$

where the  $(\beta_L R)_{DWBA}$  is taken to be 1.0 fm.

## 2.5 Dirac Optical Model

The Dirac Optical model is phenomenological and based on the Dirac equation. A detailed discussion of the model may be found in ref. [13] and citations therein. The optical potential consists of two parts:  $U_0(r)$  is the complex vector potential and  $U_s(r)$  is the complex scalar potential. The Dirac equation with these potentials is ( $\hbar=c=1$ )

$$[\vec{\alpha} \cdot \vec{p} + \beta(m + U_s(r)) + (U_0(r) + V_c(r))]\psi(\vec{r}) = E\psi(\vec{r}) \quad (16)$$

where  $V_c(r)$  is the Coulomb potential,  $E$  is the nucleon total energy in the center of mass frame, and  $m$  is the nucleon mass. The potentials  $U_0(r)$  and  $U_s(r)$  have the same Woods-Saxon form factors same as the Schrödinger type optical potentials. There are also twelve adjustable parameters to fit the elastic scattering data, the same number as the phenomenological Schrödinger equation based optical model. The two component Dirac equation in eq. (16) is usually transferred into a one component equation by substituting the lower part of the component into the upper part, and then solving it in DWBA or in coupled-channel approximation.

The optical potentials are different from the previous section. But the deformations are defined and calculated in the same manner as previously described. If

without further fine tune of the optical potential parameters (except the renormalization as in eq. (15)), the calculated inelastic scattering observables are found to reproduce the data, then the simple DWBA can be used to describe the inelastic scattering in the same manner as in the previous section.

### 3 Experimental

The TRIUMF facility is based on a six - sector isochronous cyclotron which accelerates  $H^-$  ions to 520 MeV. In the view of nuclear and particle physics experiments at intermediate energies, the use of accelerated the  $H^-$  ions creates unique features for the facility as indicated in the following: The machine is capable of producing simultaneously several beams of protons, individually variable in energies. Beam extraction is straightforward. It is obtained by passing part or all of the  $H^-$  circulating beam in the cyclotron through a stripping foil creating protons which are subsequently bent out of the cyclotron field into the beam lines. The radial position of the stripper foil is adjustable to produce continuously variable energies, the stripper height is varied to change the beam intensity. Up to  $1\ \mu A$  for polarized beam and  $100\ \mu A$  for unpolarized beam is obtainable. The Lamb-shift polarized ion source is capable of giving 70% to 80% polarized beam at injection.

As shown in Figure 4, there are two experimental halls, one is the proton hall and the other one is the meson hall. The beam line 4 delivers beam to the two proton hall channels 4A and 4B, and their different experimental target positions. The beam line 4B is limited to accepting no more than  $1\ \mu A$  of extracted beam whether polarized or unpolarized. It is therefore ideal for direct nuclear scattering experiments. Our experiment is performed at BL4B (beam line 4B), target position 4BT2, using the standard medium resolution spectrometer (MRS) facility with polarized beam. The beam transport elements in BL4B up to target position 4BT1 consist of one dipole magnet, two bending magnets and six quadrupole magnets. There are two ways of obtaining initial beam tune information. One is from beam transport calculation, the other is from previous tunes at the same energy. The quadrupole settings determine whether the beam tune is achromatic

BEAMLINES AND EXPERIMENTAL FACILITIES  
 ——— EXISTING ——— PROPOSED

or dispersed. To obtain better energy resolution, the dispersed beam was used in our experiments.

### 3.1 The In-beam Polarimeter

The in-beam polarimeter located at 4BT1 is utilized to measure the incident beam intensity and its polarization. The polarimeter consists of a thin polyethylene target and scintillation counter telescopes which intercept the scattered and recoil protons for both left and right scattering events. The polarimeter measures left and right asymmetries in p-p elastic scattering at a lab angle of  $17^\circ$ . The counter telescopes consist of 2 plastic scintillators to detect the forward scattered protons and 1 scintillator to detect the associated recoil protons at  $70^\circ$ . The schematic of IBP (In-Beam Polarimeter) is shown in Figure 5. The scintillators L1 and L2 are used in combination to detect protons scattered to the left in coincidence, the signal from the counter telescope (L1-L2) is delayed by 43 ns (The interval between the beam bunches) and again placed in coincidence with the conjugate recoil events (from L3) to distinguish the scattering events to the left and accidental events to the left. The scintillators R1, R2 and R3 are used in like manner to detect the scattering to the right. The counts for scattering to the left and to the right are corrected for accidental events. The corrected sum of the left and right triple coincidences is proportional to the total integrated beam charges. The constant of the proportionality depends on energy, and can be found in the TRIUMF users handbook. In the case of incident proton energies of 290 MeV and 500 MeV, the constants are 51.9 and 69.6 counts/sec.nA.(mg/cm<sup>2</sup>) respectively. Knowing the thickness of polyethylene, the beam intensity is calculated from the measured total counts scattered left and right of the in-beam polarimeter. The beam polarization is calculated by

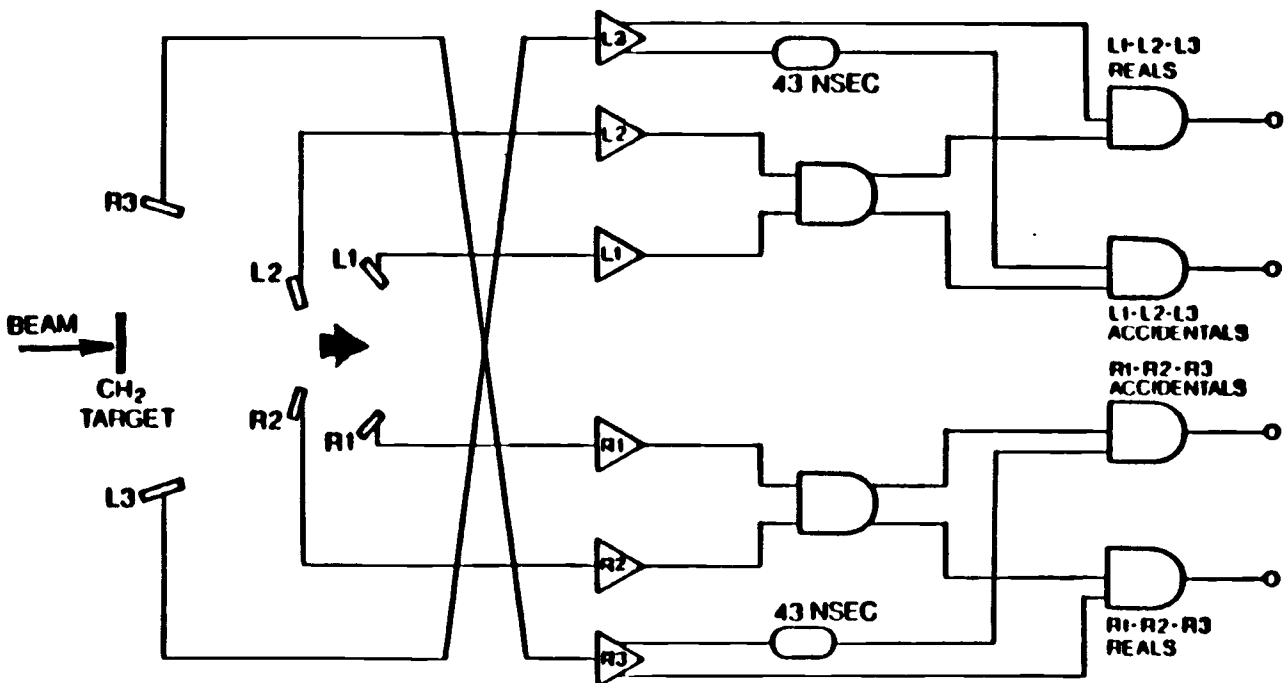


Figure 5: A schematic of in-beam polarimeter.

$$P^\uparrow = \frac{1}{A_y(\text{CH}_2)} \frac{L^\uparrow - L_{\text{acc}}^\uparrow - R^\uparrow + R_{\text{acc}}^\uparrow}{L^\uparrow - L_{\text{acc}}^\uparrow + R^\uparrow - R_{\text{acc}}^\uparrow} \quad (17)$$

$$P^\downarrow = \frac{1}{A_y(\text{CH}_2)} \frac{L^\downarrow - L_{\text{acc}}^\downarrow - R^\downarrow + R_{\text{acc}}^\downarrow}{L^\downarrow - L_{\text{acc}}^\downarrow + R^\downarrow - R_{\text{acc}}^\downarrow} \quad (18)$$

$$P^{\text{off}} = \frac{1}{A_y(\text{CH}_2)} \frac{L^{\text{off}} - L_{\text{acc}}^{\text{off}} - R^{\text{off}} + R_{\text{acc}}^{\text{off}}}{L^{\text{off}} - L_{\text{acc}}^{\text{off}} + R^{\text{off}} - R_{\text{acc}}^{\text{off}}} \quad (19)$$

where  $P^\uparrow$ ,  $P^\downarrow$  and  $P^{\text{off}}$  are the beam polarizations of spin up, spin down and spin off. The total beam charge is

$$\text{COUNT}^\uparrow = \text{Const} * (L^\uparrow - L_{\text{acc}}^\uparrow + R^\uparrow - R_{\text{acc}}^\uparrow) \quad (20)$$

$$\text{COUNT}^\downarrow = \text{Const} * (L^\downarrow - L_{\text{acc}}^\downarrow + R^\downarrow - R_{\text{acc}}^\downarrow) \quad (21)$$

$$\text{COUNT}^{\text{off}} = \text{Const} * (L^{\text{off}} - L_{\text{acc}}^{\text{off}} + R^{\text{off}} - R_{\text{acc}}^{\text{off}}) \quad (22)$$

in which  $\text{COUNT}^\uparrow$ ,  $\text{COUNT}^\downarrow$  and  $\text{COUNT}^{\text{off}}$  are total beam charges of spin up, spin down and spin off. The analyzing power  $A_y$  of  $\text{CH}_2$   $A_y(\text{CH}_2)$  depends on the incident energy. The values for 290 MeV and 500 MeV are 0.370 and 0.466 [15] respectively.

In our experiment, the beam polarization was sequenced by having 2.5 minutes spin up, 2.5 minutes spin down and 0.5 minutes spin off, and so on for the

entire run. The variation of the beam polarization for each spin state is typically  $\pm 0.005$ . The small variation was due to the varying ion source conditions.

### 3.2 Medium Resolution Spectrometer

The MRS (Medium Resolution Spectrometer) consists of a quadrupole magnet and a dipole magnet. It is mounted on the framework which rotates horizontally (non-bend plane) around the scattering chamber to intercept scattered events. Scattered particles accepted by MRS are bent  $60^\circ$  by the dipole and momentum dispersed into a large spatial scale. The combination of the quadrupole magnet and dipole magnet reproduces an image of the target beam spot in an imaginary surface (focal plane) with the momentum well dispersed. The momentum acceptance is  $\pm 10\%$  of the central value, which means roughly that at an incident energy of 500 MeV, one magnetic field setting covers a range of excitation energies of 100 MeV. It therefore has the feature of a large momentum bite. The layout and schematic of MRS are shown on Figure 6 and Figure 7. The MRS can be rotated around the chamber position 4BT2 so that scattering from  $3^\circ$  to  $135^\circ$  can be measured. The FEC (The Front End Chamber) rotates with the MRS while the scattering chamber remain fixed. There are two scattering configurations. In the large angle configuration (LAC), the range of MRS motion is from  $16^\circ$  to  $135^\circ$ . The scattering chamber connects rigidly to the MRS. The unscattered beam exits through a continuation of the beam pipe to the beam dump. The scattered beam, at the attainable angular acceptance of roughly  $3^\circ$  passes through the MRS. An alternative way of monitoring the beam intensity is available in this configuration. A secondary emission monitor (SEM) is located downstream of 4BT2 just in front of the beam dump. The unscattered beam passes first through the clean up quads to be focused, then passes through several gold foils. The number of the



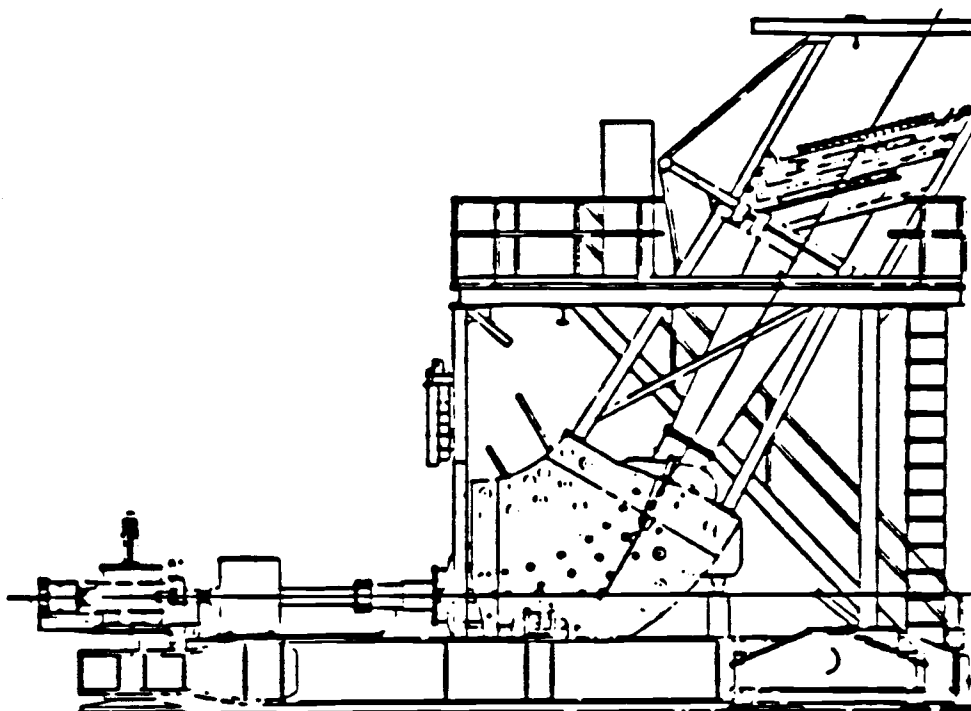


Figure 6: The layout of medium resolution spectrometer

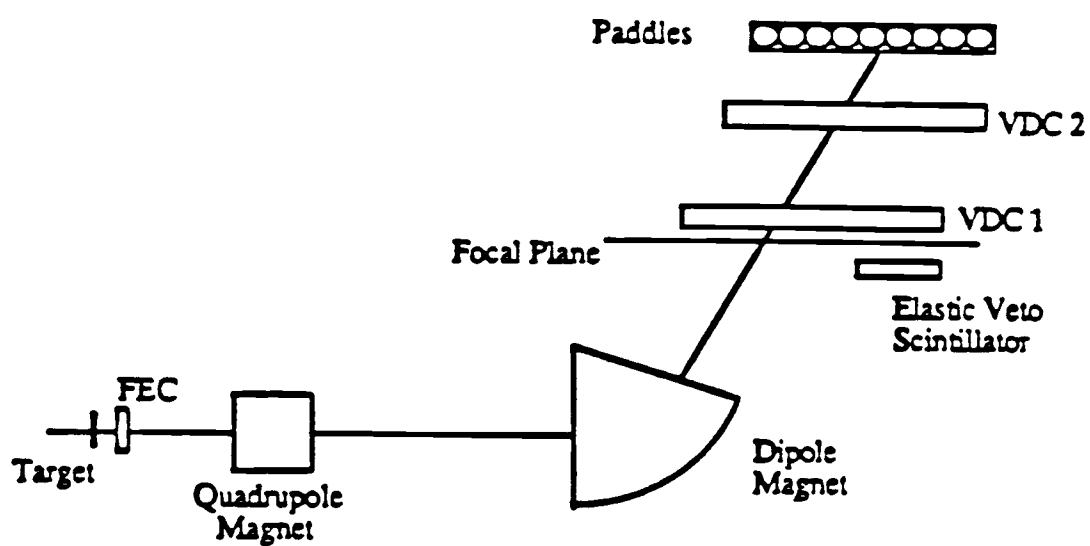


Figure 7: The schematic of medium resolution spectrometer

electrons given off is proportional to the stopping power. The electron current is detected and calibrated by a Faraday cup. In the small angle configuration (SAC), the continuation of beam pipe to the beam dump is removed and replaced by a short extension piece "horn" to connect the scattering chamber with the FEC. The unscattered beam is stopped by a beam blocker before reaching the MRS. The operating range of MRS motion is from  $4^\circ$  to  $15^\circ$ .

### 3.3 The MRS Detector

The coordinates of the trajectories are measured by three sets of wire chambers. The FEC is the first particle detector that the scattered beam encounters. It consists of 4 wire planes ( $8\text{cm} \times 8\text{cm}$  for each of them), two in horizontal or non-bend plane Y as ( $Y_0$  ,  $Y_0'$ ), the other two in vertical or bend plane X as ( $X_0$  ,  $X_0'$ ). Each plane contains alternating anode and cathode wires, so that the spatial position according to the X and Y coordinates of the particle when passing FEC can be determined, and therefore allows ray-tracing back to the target for correction of aberrations and determination of MRS solid angle.

The remaining two sets of wire chambers are the Vertical Drift Chambers (VDC1 and VDC2). They are located 37 cm apart, set at  $45^\circ$  with respect to the scattered protons and about 4m from the exit of the dipole. These chambers contain two wire planes which give coordinates in the X and U ( $30^\circ$  to X) directions of the passing particles. This information is then geometrically transformed into X and Y ( $90^\circ$  to X) coordinates with a spacial resolution of  $150\text{ }\mu\text{m}$ . The combination of the two VDCs gives an image of the scattered particles on the focal plane within the acceptance of MRS. As a consequence of the Dipole and Quadruple optics, the image reproduced from the VDCs in the X direction along the focal plane is actually a spectrum that can either be scaled by the momentum of the scattered

particles or excitation energy in the target, while the image on FEC is a global image of scattered beam from a spot on the target with momenta of scattered particles heavily degenerated.

Ten plastic scintillator trigger paddles are located above the VDCs. Their function is to restrict the momentum acceptance of the focal plane by disabling certain regions of the focal plane in the trigger and therefore reduce the amount of uninteresting data. In our case, ten of the scintillator paddles are used to construct the largest focal plane or maximum momentum acceptance the MRS can provide for one magnetic field setting. To obtain spectra over a broader momentum scale, three different dipole and quadrupole magnetic field settings are used ( 3 momentum bites), each momentum bite provides us an interval of about 60 MeV of excitation energy for  $E_p = 290$  MeV. The spectra from different bites are usually overlapped in a certain range.

The elastic veto scintillator is placed just bellow the focal plane at the position where the elastically scattered particles will pass through. It is used to inhibit the detection of the elastic scattering events so that the inelastic scattering events can be registered without recording too many elastic scattering events. For a pre-scaling factor of 1000, one elastic scattering event out of 1000 is registered. It increases the amount of interesting inelastic scattering data on tape for small angle measurements.

### 3.4 The MRS Trigger

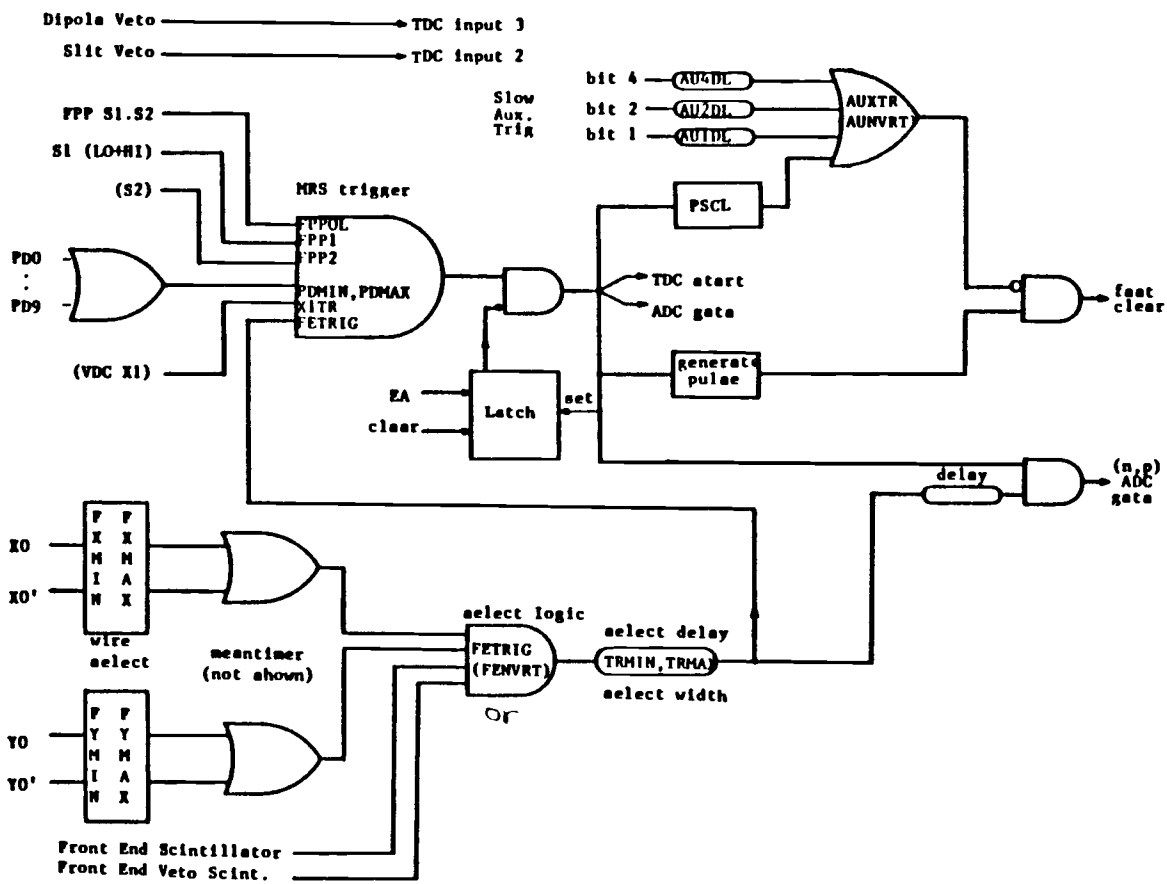
An minimum requirement for a scattered event detected by MRS is a coincidence between a signal from the front end chamber (with appropriate time delay) and signals from VDCs. The time of flight of particles through the MRS is also obtained from these signals. Particles with the same momentum but different mass

or  $(E/|\vec{p}|)$  will drift at different speeds and therefore have different time of flights. A coordinate based on the time of flight called TTB and the corresponding spectrum is generated for the use of identifying protons from others. The scintillator paddles are also 'and' in the trigger, on one hand to select the interesting region in focal plane, and on the other hand to register the energies lost in the paddles. Particles with different charge and mass  $(ZE/|\vec{p}|)$  will have different energy lost in the scintillator paddles. A coordinate called ESUM (the maximum energy deposited in the scintillators) and the corresponding spectrum is generated to distinguish protons from others (mainly deuterons). The combination of the time of flight and the pulse height from scintillator paddles is used for the particle identification. The two dimensional spectrum called SPID (TTB vs ESUM) is generated for the purpose of rejecting non-proton events. The elastic veto scintillator is added in the trigger at low angles when the elastic scattering dominates the scattered events. An illustration of MRS triggers is shown in Figure 8.

### 3.5 Data Stream

The events that satisfy the MRS trigger conditions generate signals in the individual detectors. The signals are first routed to CAMAC (computer interface) crates where they are digitized by TDCs (Time to Digital Converter) and ADCs (Amplitude to Digital Converter). The CAMAC system reads the scaler and scaler rates for each of the detectors as well as the signals from TDC's and ADC's in the order specified by the DACS (Data Acquisition Control System on Eclipse/S200 computer). These events including scalers and scaler rates are transferred in the same order by DACS to the buffers in the computer. The majority of the events in the buffers are transferred directly onto tapes to be analyzed off line. A small fraction of the events in the buffers are decoded and analyzed on line using the

Figure 8: The schematic of the MRS triggers



same DACS to monitor the data acquisition from run to run. Each MRS detector and IBP detector has a built in pulser; the pulser events, scaler and scaler rates will be sent by DCR (digital control register) to CAMAC should an event be detected. The MRS users make use of the pulser system to monitor the data quality, data acquisition system and overall system dead time from run to run.

The overall system dead time is calculated using either the pulser system or the MRS trigger system. In our experiments, both approaches are used to estimate the dead time, and found to be in agreement within 1.0%. The over all live-time using MRS trigger is

$$LT = \frac{\text{busylatch} - \text{fastclear}}{\text{MRStrigger} - \text{fastclear}} \quad (23)$$

The over all live time using the pulser system is

$$LT = \frac{\text{CPUSLER}}{\text{PULSER}} \quad (24)$$

The live times calculated using the pulser for the spin up, spin down and spin off are

$$LT^{\uparrow} = \frac{\text{CPUSLER}^{\uparrow}}{\text{PULSER}^{\uparrow}} \quad , \quad (25)$$

$$LT^{\downarrow} = \frac{\text{CPUSLER}^{\downarrow}}{\text{PULSER}^{\downarrow}} \quad (26)$$

$$LT^{\text{off}} = \frac{\text{CPUSLER}^{\text{off}}}{\text{PULSER}^{\text{off}}} \quad (27)$$

### 3.6 Dispersion Matching Technique

A dipole magnet in the beam transport system behaves very much like a prism in an optical system. On the one hand, it may be used to disperse a non-monoenergetic and point-like beam into a spatially dispersed beam, for which position is a function of the momentum. The larger the momentum spread of the beam the greater the spatial separation of rays with different momentum. On the other hand, a dipole magnet may be used to focus a slightly spatially dispersed beam to a common point. In both cases, conservation of phase space must be preserved to satisfy the Liouville's theorem. The dispersion matching technique consists of tuning the beam in the dispersed mode so that the incident proton beam has the same dispersion as the MRS dipole. Then with respect to the magnetic dipole, these incident protons can be considered as a monoenergetic "point" source. Particles scattered from the same source point on the target but with different energy loss will be momentum dispersed along the focal plane by MRS dipole while scattered particles of the same energy loss but from different "source point on the target" will be focused to the same position on the focal plane. An illustration of dispersion matching is given in Figure 9. In this way, the energy resolution or the momentum resolution on the focal plane will be ideally independent of the initial beam energy spread. The initial beam dispersion produced by the cyclotron is typically 1 MeV and is in the horizontal plane, perpendicular to the MRS dispersion plane. The dispersion beam is rotated  $90^\circ$  by the twister quads in between 4BT1 and 4BT2 so that it lies in the same plane as the MRS dipole, making dispersion matching possible. Further details relating to TRIUMF and MRS can be found in [15] and [16].



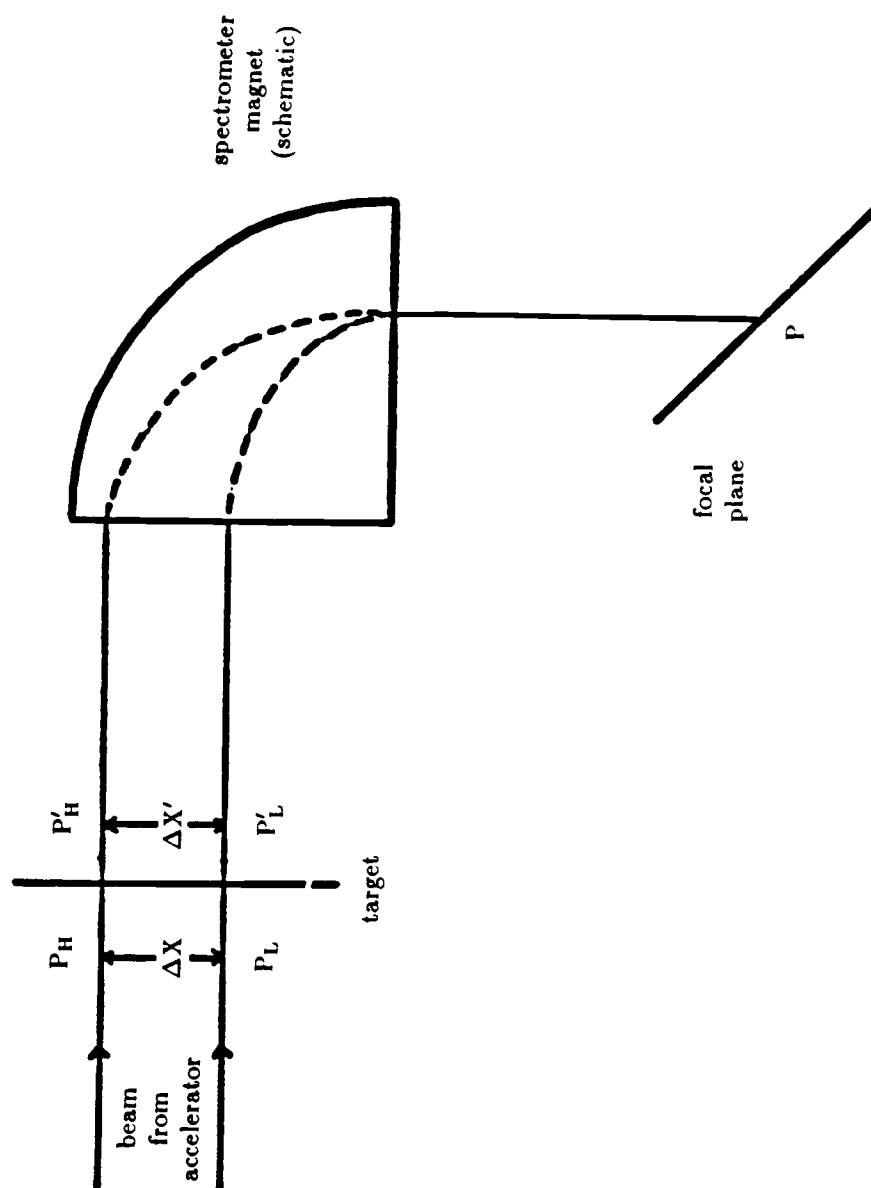


Figure 9: The principle of dispersion matching

### 3.7 Experiment 319

Experiment 319 is a study of the  $^{208}\text{Pb}(\bar{p}, p')$  reaction at 290 MeV and 500 MeV. This experiment is the first measurement of the analyzing power angular distribution for the inelastic continuum and is also intend to provide analyzing powers and cross sections for all resolved low-lying states. Major experimental features of the experiment include maximum utility of the large focal plane momentum acceptance for a single MRS magnetic field setting and the use of up to 3 momentum bites(3 different magnetic field settings) to cover a total range of 0 to 250 MeV of excitation energy. The dispersion matching technique is applied to obtain good energy resolution , especially for the low-lying states. Data taking procedures were carefully followed to assure the quality of data events, both for on-line observation and later off-line analysis. The positions of elastic scattering peaks in the focal plane were checked to avoid the edge of the focal plane where the MRS acceptance is poorer when setting up the MRS magnetic fields. Going from one momentum bite to the other, the MRS magnetic field settings are chosen to achieve about 30 MeV excitation energy overlap so that we can make smooth spectrum connections from bite to bite. The elastically scattered events are important for the study of low-lying states. The elastic scattering rates were scaled down using the elastic veto scintillator to record inelastic scattering, while monitoring the statistics of the elastic events. Elastic scattering was used as one of the overall normalization checks by comparing the angular distribution of elastic cross sections with the existing accurate TRIUMF data [5]. The second normalization check was to use the elementary elastic  $\text{H}(p, p)$  reactions, for which theoretical calculations are available from phase shifts and can be compared with our measured cross sections. The target used for the reaction was a polyethylene target. Details of the normalization procedure leading to the cross sections will be discussed in

the next chapter.

## 4 Data Analysis

The off-line data analysis consists of two major parts. The first part is the replay of data tapes to obtain momentum spectra and the second part, the calculations of absolute differential cross sections, analysing powers and estimates of their statistical errors. The data analyses was also carried out at TRIUMF with the Vax 8600 computer using replay code LISA.

### 4.1 Data Replay

The data replay setup and the replay procedure is essentially the same as the on-line experimental setup and on line data acquisition. Instead of tuning the beam, the MRS transport coefficients are supplied and fine tuned for both SAC and LAC configurations. Instead of being read from CAMAC, the data are now read and decoded from tapes to disk. Data resulting from the experimental configuration, which are called type 2 events contain information from MRS wire chambers and were used together with the MRS transport coefficients to reconstruct trajectories through the MRS spectrometer.

The general philosophy for replay is to identify good events where protons are detected by MRS using available information and keep as many of such uncut events as possible. The good protons should pass through the FEC planes, pass through at least three of the four VDCs planes, and be within the  $\theta_{pc}$  and  $\phi$  acceptances.

Several one and two dimensional histograms were generated to optimize the focal plane resolution and to reject the nonproton events. The two dimensional histogram SPID is used to cut out events other than protons. The energy loss in the scintillator paddles is plotted vs time of flight, as shown in Figure 10.

The initial focal plane coordinate XF is calculated using the two VDC's. The momentum dependent quantity  $\theta$ , which determines the momentum acceptance of MRS in bend plane was corrected to  $\theta_{pc}$ , which is independent of the focal plane position, by tuning the relationship between  $\theta$  and the focal plane coordinate XF. The focal plane coordinate XF is corrected to the final value XFK by making corrections for kinematics and MRS aberrations. The final focal plane position is further corrected to the MRS acceptance, FEC acceptance, and target positions up to second order. The resolution is usually improved by about 30 % after the aberration corrections. Example of typical spectrum for XF and XFK are shown in Figure 11 and Figure 12.

Cuts were set on  $\theta_{pc}$  to make sure the MRS acceptance was flat over the interesting region of the focal plane, as shown in Figure 13. The protons that passed through FEC and VDCs but were not inside the flat  $\theta_{pc}$  acceptance were rejected. The protons detected by MRS produce an image on the X0 plane. The image, gated by  $\theta_{pc}$ , was used to calculate the effective solid angles. The accumulations of the data under the above conditions give us the focal plane spectra xfu, xfd, xfo and etc. corresponding to beam polarizations of spin up, spin down and spin off as counts per channel vs channel number.

## 4.2 Overall MRS Chamber Efficiency

Determination of MRS Chamber efficiency can also be considered as a calibration of MRS chamber. As mentioned in the previous chapter, the MRS chamber system consists of two vertical drift chambers and one front-end chamber with six wire planes (X1, X2, U1, U2, X0, Y0). The physical events do not always map over the entire physical extent of the wire planes. To determine the efficiency for VDCs, an upper limit and lower limit of the active region of the wire planes are set

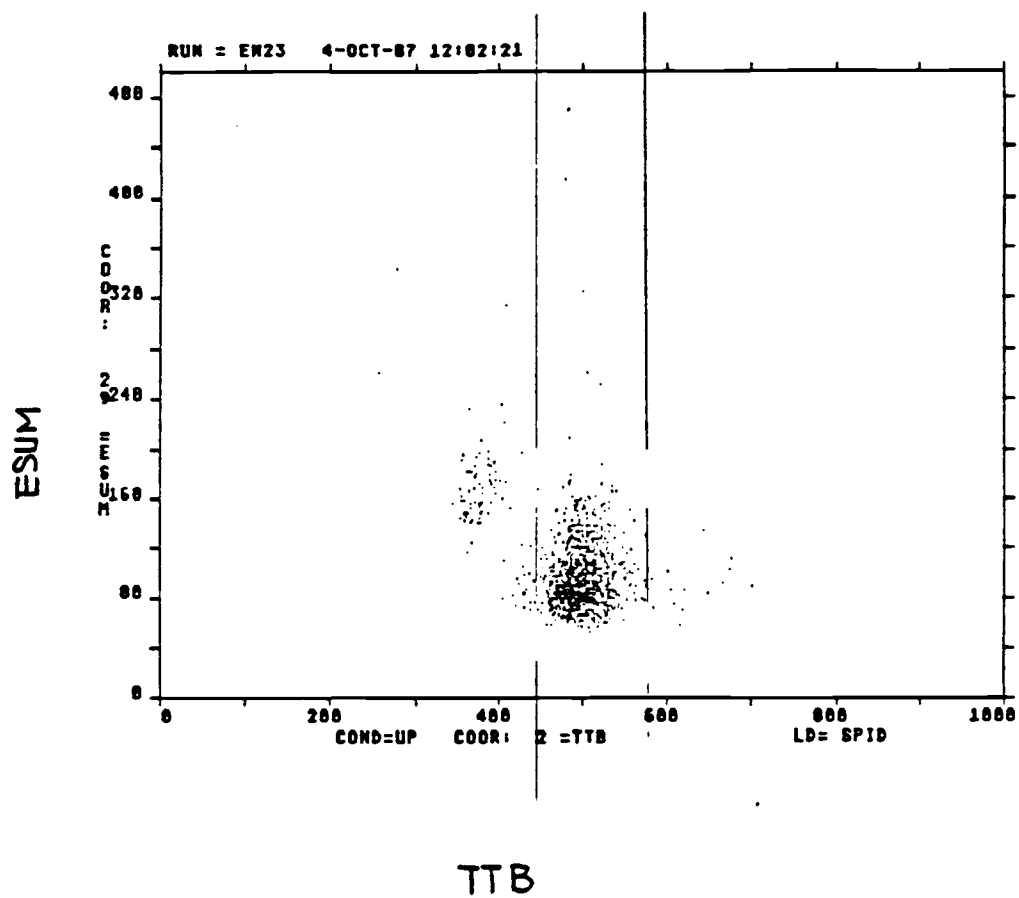


Figure 10: A 2-D histogram for particle identifications.

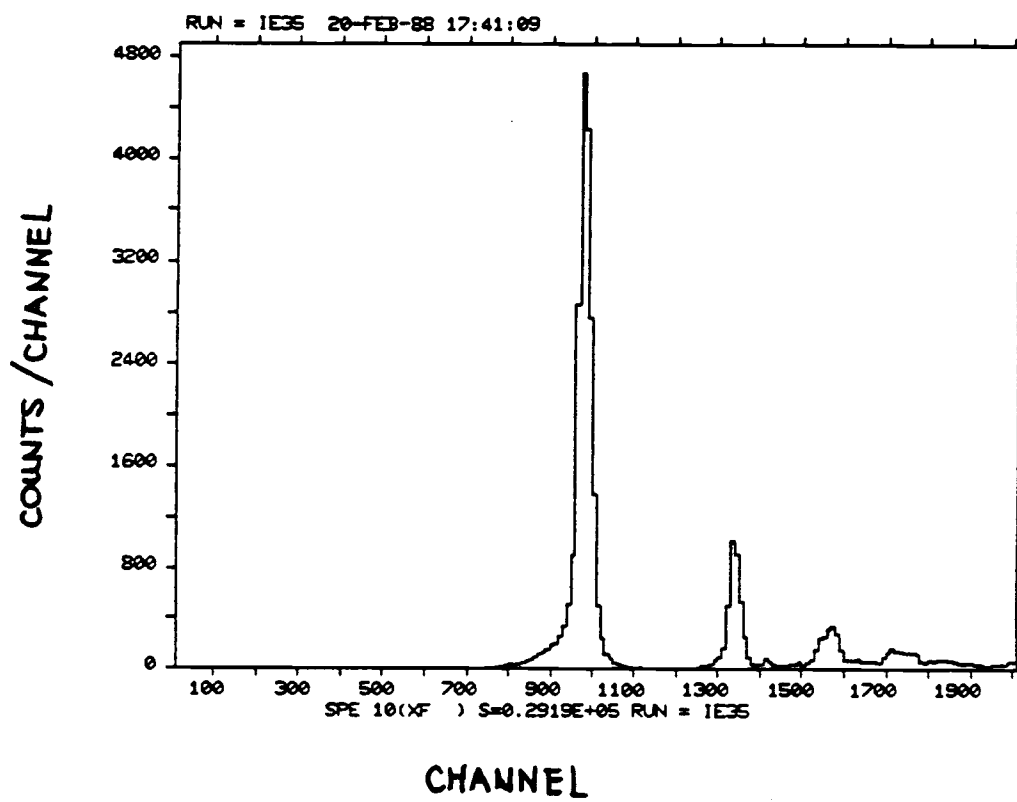


Figure 11: A spectrum without aberration corrections.

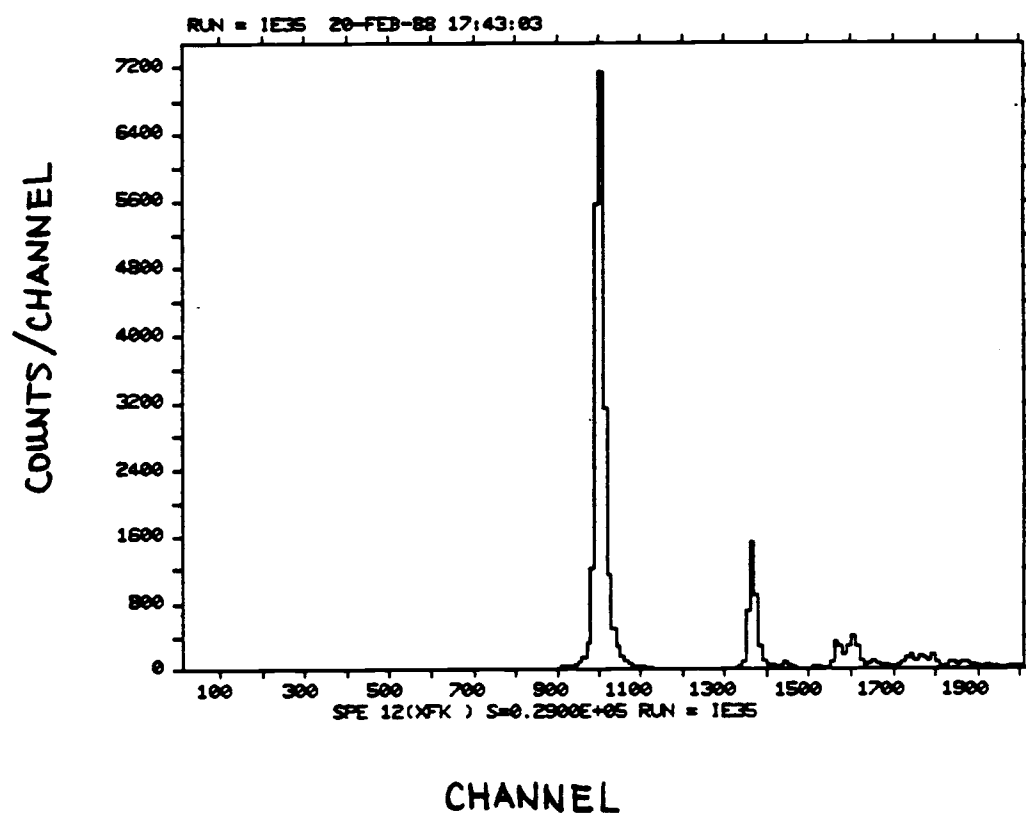


Figure 12: A spectrum after aberration corrections.



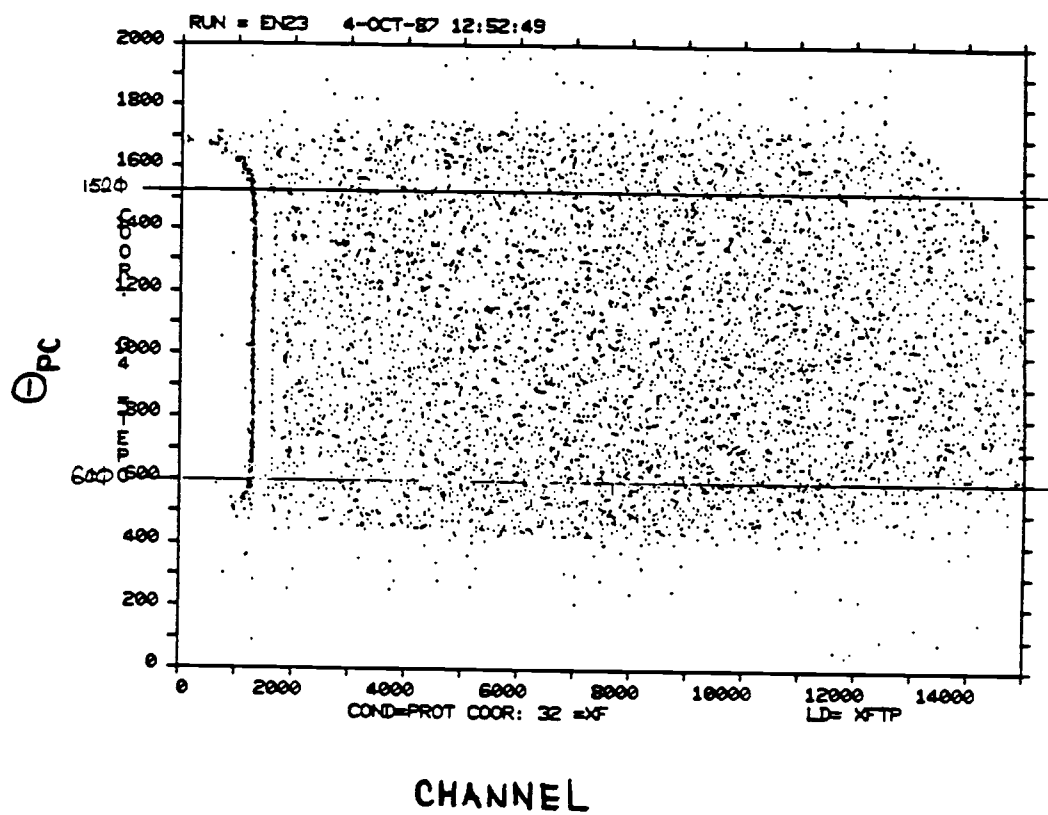


Figure 13: A 2-D spectrum of  $\theta_{pc}$  vs focal plane XFK.

to construct the physically interesting region within the VDCs. If the events fall into all 4 wire planes of the VDCs, the events will be detected. If the events pass through 3 of the 4 wire planes, then one of the wire planes is not “hit”. If four hits are required as a condition of a “good event” then some acceptable proton events are likely missing. That is to say the requirement of 4 out of 4 hits is probably too stringent. Some of the missing events should be included as good protons and used in the later calculations. The detection efficiency for the plane is, for example (X1 wire plane)

$$\epsilon_{X1} = \frac{X1 * X2 * U1 * U2}{X2 * U1 * U2} \quad (28)$$

The efficiency for each VDC wire plane so determined is typically around 99%. The over all efficiency of VDC chamber is therefore

$$\epsilon_{VDC} = \epsilon_{X1} \times \epsilon_{X2} \times \epsilon_{U1} \times \epsilon_{U2} \quad (29)$$

The determination of efficiency for FEC is similar, and should a missing or a multiple “hit” (MMX0) occur on X0 plane or Y0 plane, the protons (the good events) will not be registered by the FEC. The detection efficiency for the X0 plane is

$$\epsilon_{X0} = 1 - \frac{X1 * X2 * U1 * U2 * Y0 * MMX0}{X1 * X2 * U1 * U2 * Y0} \quad (30)$$

The detection efficiency for Y0 plane is

$$\epsilon_{Y0} = 1 - \frac{X1 * X2 * U1 * U2 * X0 * MMY0}{X1 * X2 * U1 * U2 * X0} \quad (31)$$

The over all FEC efficiency is therefore

$$\epsilon_{\text{FEC}} = \epsilon_{X0} \times \epsilon_{Y0} \quad (32)$$

The important thing is to set X0, Y0 in OR mode when setting up the MRS trigger for the data acquisition to cause the MRS overall to trigger on all scattering events. The total MRS chamber efficiency is

$$\epsilon = \epsilon_{X0} \times \epsilon_{Y0} \times \epsilon_{X1} \times \epsilon_{X2} \times \epsilon_{U1} \times \epsilon_{U2} \quad (33)$$

The typical MRS chamber efficiency is around 90%.

### 4.3 Normalizations

The Data replay gives us the energy spectra of scattered protons. The spectra are usually expressed in terms of counts per channel vs channels. The data points are rebinned if necessary to reduce the statistical fluctuations. In the case of SAC, data points are rebinned in 5 channel intervals, while in the case of LAC, 15 to 22 channels are used. Figure 14 and Figure 15 show the spectrum before channel rebin and after channel rebin. As may be seen rebinning results in no apparent loss of energy resolution. The absolute cross section is obtained by multiplying the reaction yield  $N$  (counts/bin) times a normalization factor  $F$ . The normalization factor depend on the number of incident protons ( $n_b$ ), the data acquisition system dead time (DT), the number of scattering centers per unit area in the target ( $n_{\text{Tdx}}$ ), the solid angle of the detector ( $\Delta\Omega$ ) and the MRS chamber efficiency  $\epsilon$ . The normalization factors for the cases of spin up, spin down, spin off are expressed as:

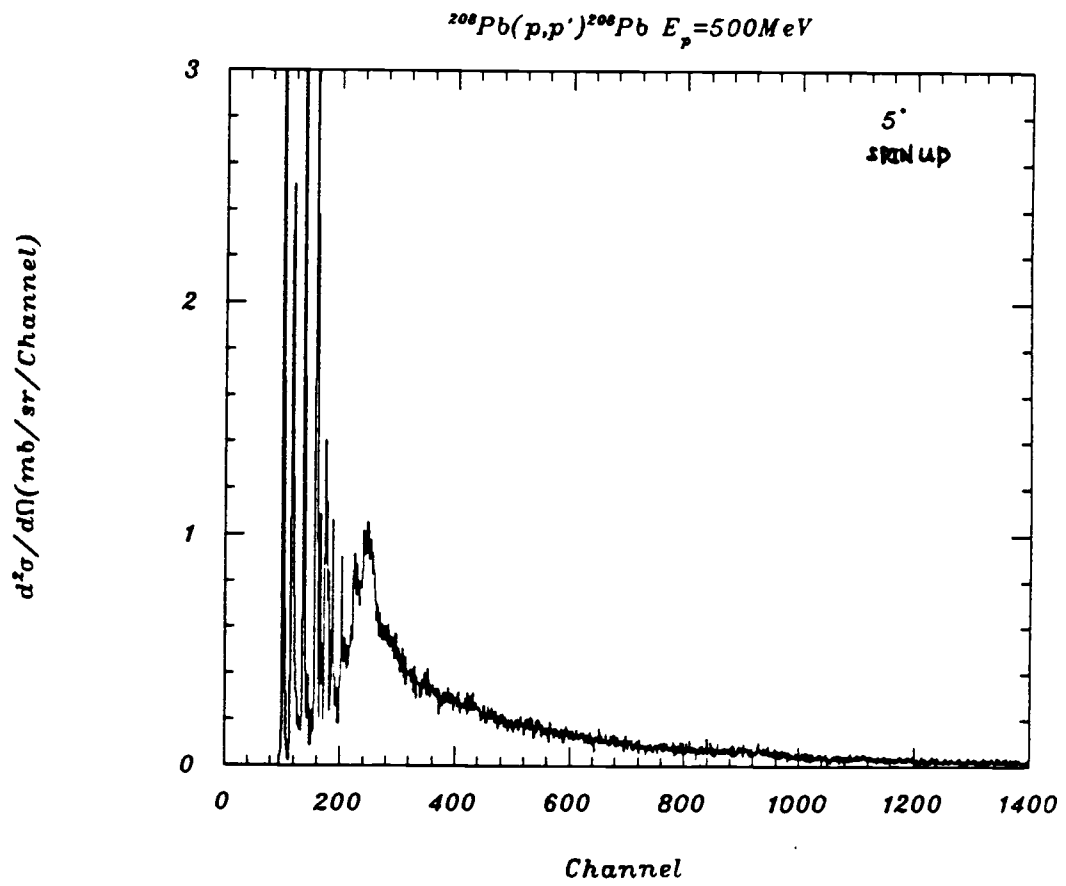


Figure 14: A spectrum before channel rebin.

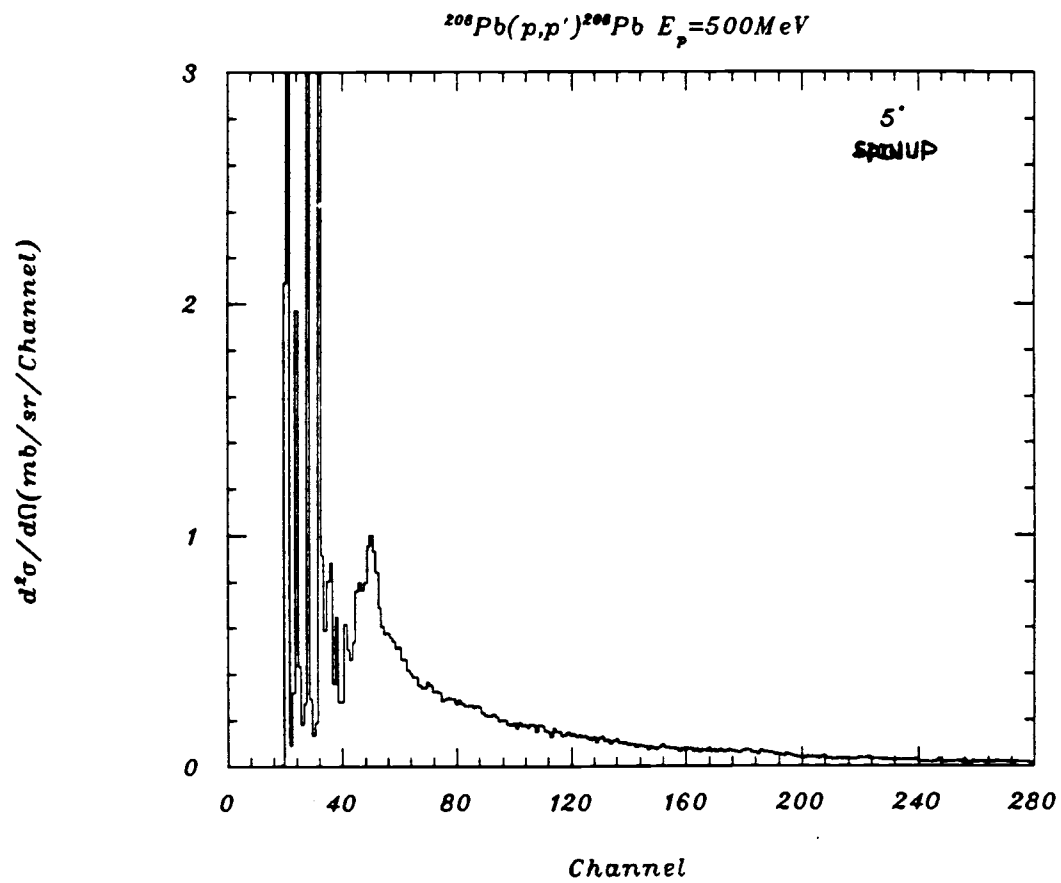


Figure 15: A spectrum after channel rebin.

$$F^{\uparrow} = \frac{1}{\Delta\Omega * n_T dx * LT^{\uparrow} * n_b^{\uparrow} * \varepsilon^{\uparrow}} \quad (34)$$

$$F^{\downarrow} = \frac{1}{\Delta\Omega * n_T dx * LT^{\downarrow} * n_b^{\downarrow} * \varepsilon^{\downarrow}} \quad (35)$$

$$F^{\text{off}} = \frac{1}{\Delta\Omega * n_T dx * LT^{\text{off}} * n_b^{\text{off}} * \varepsilon^{\text{off}}} \quad (36)$$

The double differential cross sections for spin up, spin down and spin off are obtained from the following:

$$\frac{d^2\sigma^{\uparrow}}{d\Omega dE} = \frac{N^{\uparrow} F^{\uparrow}}{\Delta E} \cdot \frac{(mbSr^{-1}/bin)}{(MeV/bin)} \quad (37)$$

$$\frac{d^2\sigma^{\downarrow}}{d\Omega dE} = \frac{N^{\downarrow} F^{\downarrow}}{\Delta E} \cdot \frac{(mbSr^{-1}/bin)}{(MeV/bin)} \quad (38)$$

$$\frac{d^2\sigma^{\text{off}}}{d\Omega dE} = \frac{N^{\text{off}} F^{\text{off}}}{\Delta E} \cdot \frac{(mbSr^{-1}/bin)}{(MeV/bin)} \quad (39)$$

The dispersion of the MRS obtained from the well known excited states for all angles makes it possible to find the analyzing power and cross section at any excitation energy.

#### 4.4 Cross Sections and $A_y$

In general, the polarized differential cross sections depend on the beam polarization  $\vec{P}$  and the analyzing power of the target  $\vec{A}_y$ .

$$\frac{d^2\sigma}{d\Omega dE} \big|_{\vec{P}} = \frac{d^2\sigma}{d\Omega dE} \big|_0 (1 + \vec{P} * \vec{A}_y) \quad (40)$$

The double differential cross sections for spin up and spin down are given by

$$\frac{d^2\sigma}{d\Omega dE}^\uparrow = \frac{d^2\sigma}{d\Omega dE} \big|_0 (1 + P^\uparrow * A_y) \quad (41)$$

$$\frac{d^2\sigma}{d\Omega dE}^\downarrow = \frac{d^2\sigma}{d\Omega dE} \big|_0 (1 - P^\downarrow * A_y) \quad (42)$$

The unpolarized differential cross section  $\frac{d^2\sigma}{d\Omega dE} \big|_0$  and analyzing power  $A_y$  can easily be found to be

$$\frac{d^2\sigma}{d\Omega dE} \big|_0 = \frac{\frac{d^2\sigma}{d\Omega dE}^\uparrow * P^\downarrow + \frac{d^2\sigma}{d\Omega dE}^\downarrow * P^\uparrow}{P^\uparrow + P^\downarrow} \quad (43)$$

$$A_y = \frac{\frac{d^2\sigma}{d\Omega dE}^\uparrow - \frac{d^2\sigma}{d\Omega dE}^\downarrow}{P^\downarrow * \frac{d^2\sigma}{d\Omega dE}^\uparrow + P^\uparrow * \frac{d^2\sigma}{d\Omega dE}^\downarrow} \quad (44)$$

where  $P^\uparrow$  and  $P^\downarrow$  are the absolute values of the beam polarization mentioned in Chapter 3. The statistical errors of the differential cross section and analyzing power are given by

$$\Delta\left(\frac{d^2\sigma}{d\Omega dE} \big|_0\right) = \frac{1}{2} \left[ \left(\frac{d^2\sigma}{d\Omega dE}^\uparrow\right)^2 \left(\left(\frac{\Delta F^\downarrow}{F^\downarrow}\right)^2 + \frac{F^\downarrow}{\frac{d^2\sigma}{d\Omega dE}^\downarrow}\right) + \left(\frac{d^2\sigma}{d\Omega dE}^\downarrow\right)^2 \left(\left(\frac{\Delta F^\uparrow}{F^\uparrow}\right)^2 + \frac{F^\uparrow}{\frac{d^2\sigma}{d\Omega dE}^\uparrow}\right) \right]^{1/2} \quad (45)$$

$$\Delta(A_y) = \frac{2 \frac{d^2\sigma}{d\Omega dE}^\uparrow \frac{d^2\sigma}{d\Omega dE}^\downarrow}{P\left(\frac{d^2\sigma}{d\Omega dE}^\uparrow + \frac{d^2\sigma}{d\Omega dE}^\downarrow\right)^2} \left[ \frac{\Delta F^\uparrow}{F^\uparrow} + \frac{\Delta F^\downarrow}{F^\downarrow} + \frac{F^\uparrow}{\frac{d^2\sigma}{d\Omega dE}^\uparrow} + \frac{F^\downarrow}{\frac{d^2\sigma}{d\Omega dE}^\downarrow} \right]^{1/2} \quad (46)$$

The overall statistical error of normalization factor  $F^\uparrow$  and  $F^\downarrow$  are estimated to be 7%. The unpolarized double differential cross sections eq. 43 were compared with the spin off double differential cross section and found to agree within 3%.

#### 4.5 Continuum

As shown in Figure 16 the nuclear structure features of the spectra present at low-excitation energy gradually disappear as the scattering angle is increased. The histograms are the experimental data. The smooth curves are the calculated quasifree scattering to the continuum. Details with more figures will be discussed in the next chapter. For each angle, the double differential cross sections of spin up, spin down are calculated for each data point. The different momentum bites are then connected together. Data in the continuum for low angles ( $5^\circ$  to  $15^\circ$ ) and for high angles are handled in the slightly different ways at  $E_p=290$  MeV. For 290-MeV data, the nuclear structures above the continuum are negligible at high angles. The measured double differential cross sections for spin up and for spin down at each data point are then used directly to calculate the unpolarized double differential cross sections and analyzing powers. At low angles, the continuum extends underneath resolved nuclear structures at each angle. A formula based on a semi-empirical procedure was used to estimate the continuum in this region. The nuclear structure contribution was then subtracted from the measured cross sections. The phenomenological procedure adopted is to use a Gaussian-like function and a forth order polynomial function to describe the the continuum as indicated in the following equation.



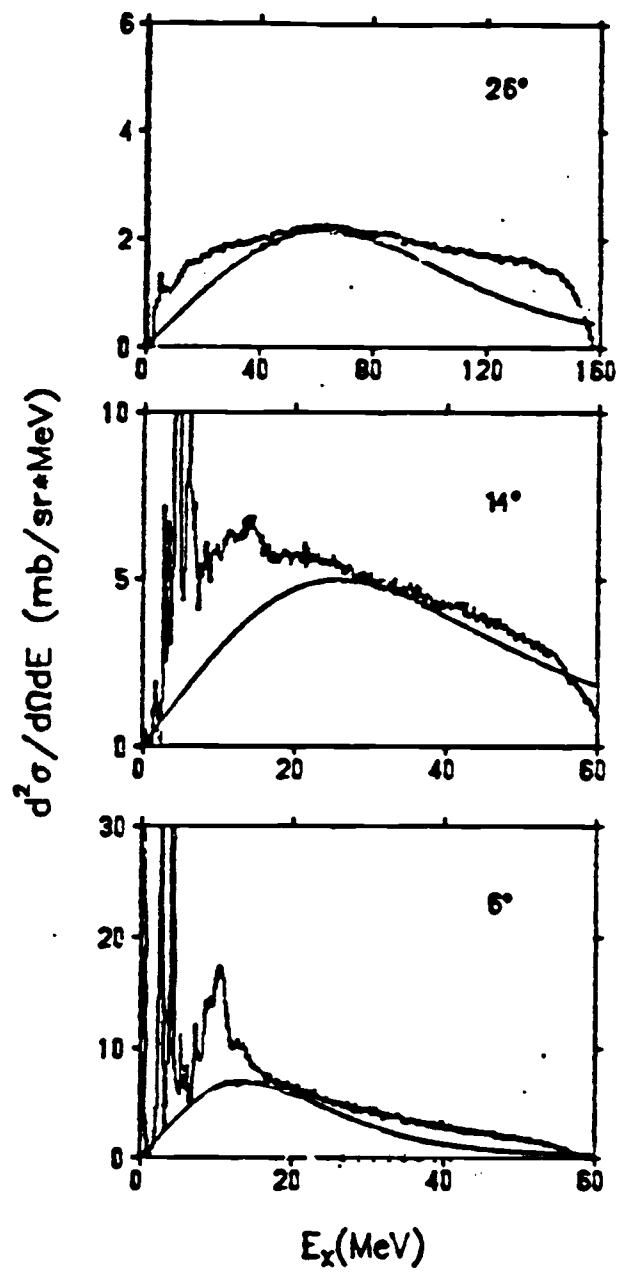


Figure 16: Some spectra from  $E_p=290$  MeV data.

$$N(E_x) = \begin{cases} N_0(1 - e^{\alpha \cdot E_x})e^{-(E_x - E_{x0})/\lambda} & \text{if } E_x < E_{x0} \\ (b_4(E_x - E_{x0})^2 + b_3(E_x - E_{x0}) + b_2) \times \\ (E_x - E_{x0})^2 + N_0(1 - e^{-\alpha \cdot E_{x0}}) & \text{otherwise} \end{cases} \quad (47)$$

The centroid excitation energy  $E_{x0}$  is given by equation (9) and  $\alpha = 0.25 \text{ MeV}$  is a cutoff factor which simulates Pauli blocking effects. The parameter  $\lambda$  is adjusted to reproduce the observed continuum in the nuclear structure region. The phenomenological continuum spectra thus obtained are used to calculate the unpolarized double differential cross sections and analyzing powers at low angles of 290 MeV data. Quasifree peaks are well above the nuclear structure region in the 500 MeV data, and hence the uncorrected spectra are used in the cross section and analyzing power calculations. The results of the analysis will be presented in the next chapter.

#### 4.6 Low-lying states

Once the double differential cross sections for spin up and spin down are established, the decomposition and fitting of the low-lying states may be done. Gaussian functions are chosen to fit the peaks. The general procedure is to use the following Gaussian function

$$F_i(N_i, \sigma, E_i) = \frac{N_i}{\sqrt{2\pi}\sigma} e^{-(E_x - E_i)^2 / 2\sigma^2} \quad (48)$$

in which  $N_i$  parameters are allowed to vary during the  $\chi^2$  minimizations. The parameter  $\sigma$  (the standard deviation) and  $E_i$  (the peak positions) are fixed during fitting. The value of  $\sigma$  is established using the most prominent peak at each angle.

The peak positions  $E_i$  for individual low-lying states are determined using the angles where the reactions have the maximum cross sections. Figure 17 shows the result of fitting spin up, and spin down spectra at a scattering angle of  $10^\circ$ . The cross sections, analyzing powers and their statistical errors are calculated using the eq. (43), (44), (45) and (46). The results of low lying states will be discussed in the next chapter.

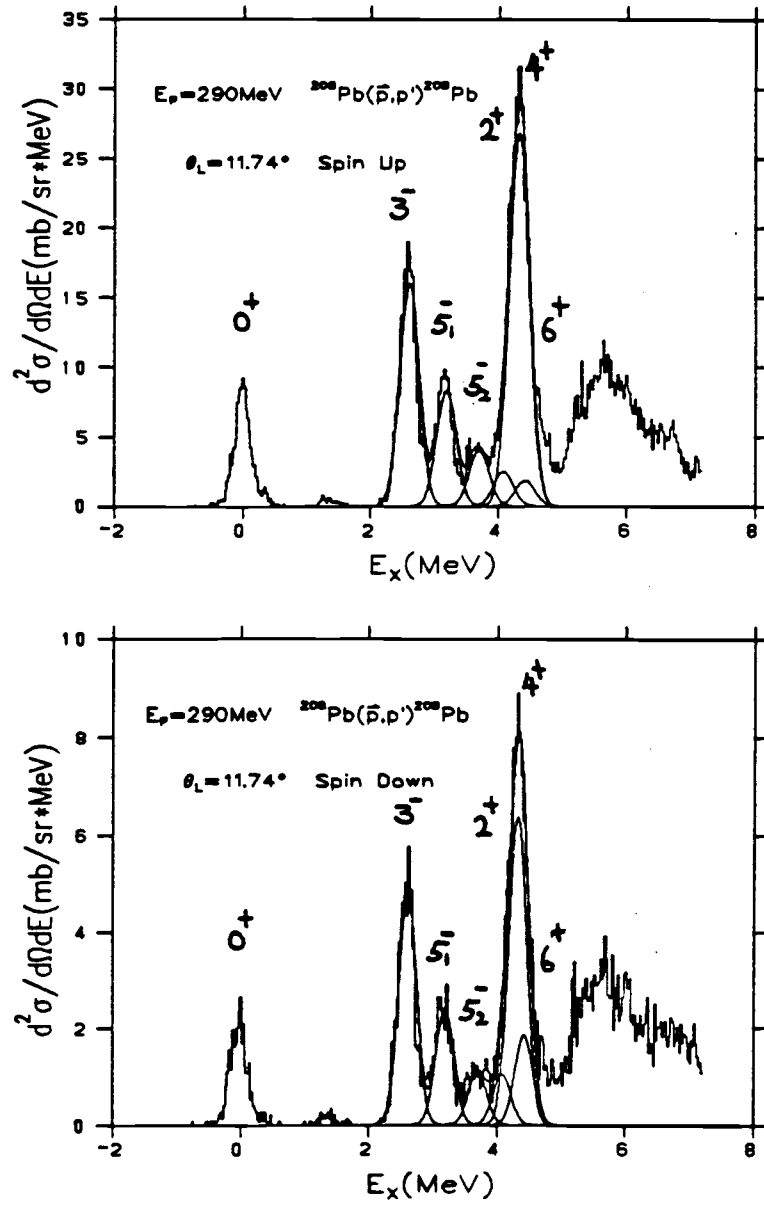


Figure 17: Fitting of low-lying states.

## 5 Results and Discussions

Using the Medium Resolution Spectrometer(MRS) at TRIUMF, we have measured the cross section and analyzing power of inelastic scattering to the continuum and to the low-lying states of  $^{208}\text{Pb}$  (51.0 mg/cm<sup>2</sup>) target nuclei. The incident polarized proton beam energy was chosen to be 290 MeV and 500 MeV. The beam intensity was controlled within the range 0.1 to 2.0 nA. Three other targets were mounted on the same target ladder. They were polyethylene (49.94 mg/cm<sup>2</sup>), ZnS and the blank target frame. The blank target was placed in the scattering position occasionally to check whether or not the incident beam "hit" the target frame causing background. The ZnS target was placed in the scattering position regularly to check beam position at the target. As one of the normalization checks, the CH<sub>2</sub> target was placed to the scattering position at each angle chosen in the experiment to measure the differential cross section of elastic scattering of protons from hydrogen. The replay conditions and solid angles of the p-H elastic scattering are chosen to be the same as those used for proton scattering on  $^{208}\text{Pb}$  at the corresponding angles. The experimental angular distribution of differential cross sections of  $H(\vec{p}, p')$  at available angles are compared with the theoretical p-p elastic scattering results calculated from the code SAID. The comparisons are shown in Figure 18. Agreements is found to be within  $\pm 7\%$ .

As another check of our normalizations, the differential cross section angular distributions of elastic proton scattering from  $^{208}\text{Pb}$  are comparing with previous TRIUMF data [5] on elastic proton scattering to  $^{208}\text{Pb}$ . Our 500-MeV elastic scattering data are compared with the previous 500-MeV TRIUMF data [5] in Figure 19.

Our 290-MeV elastic scattering data and the previous TRIUMF data [5] at

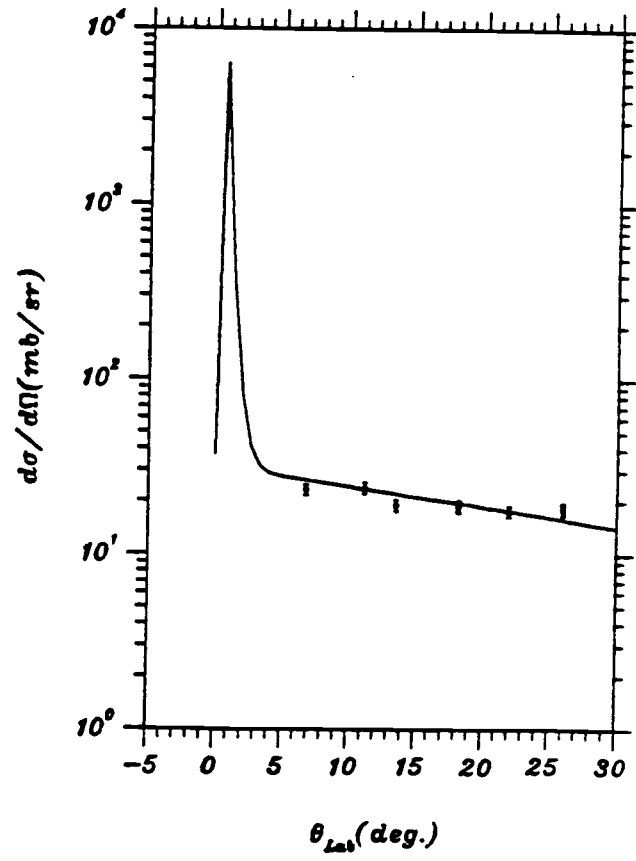


Figure 18: Normalization check using CH<sub>2</sub> at E<sub>p</sub>=500 MEV

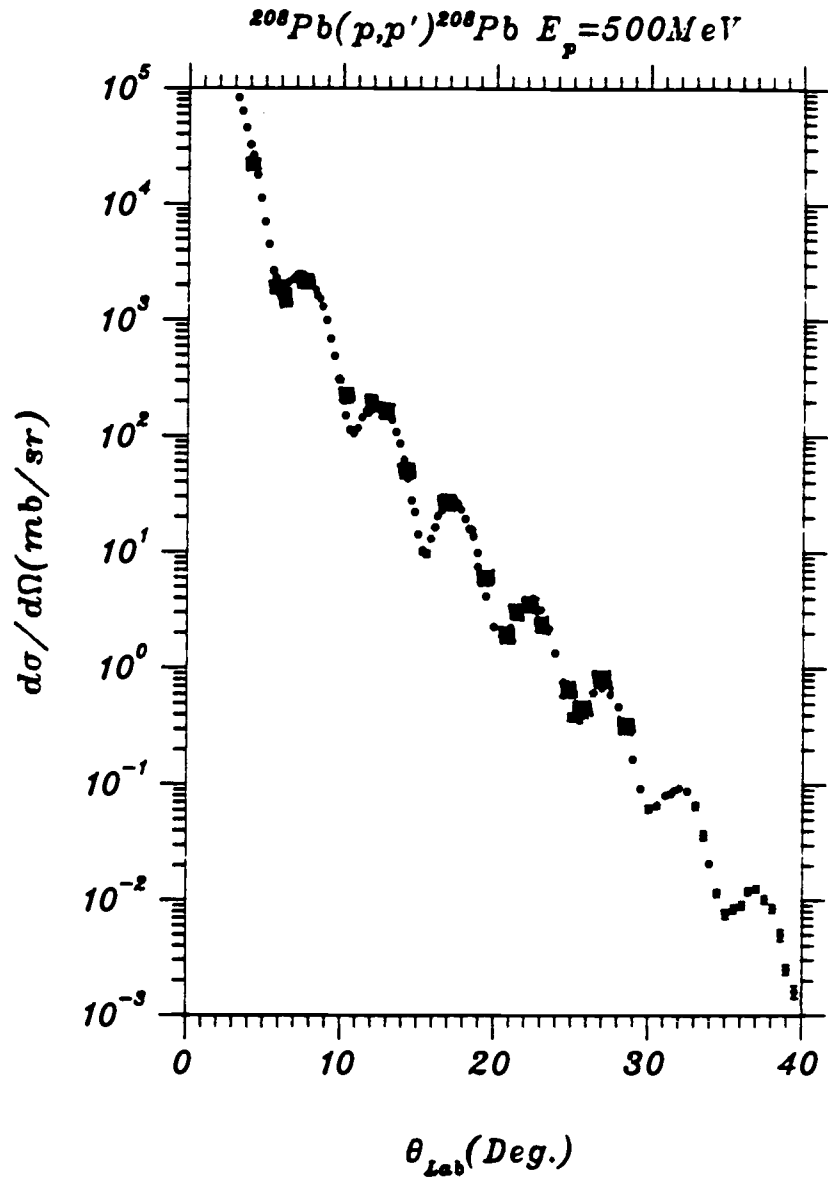


Figure 19: Normalization check using elastic  $p\text{-}^{208}\text{Pb}$  at  $E_p = 500 \text{ MeV}$

300 MeV are first scaled from  $d\sigma/d\Omega$  vs  $\theta_L$  to  $d\sigma/d\Omega$  vs  $q(\text{fm}^{-1})$  and then compare with each other in Figure 20. The agreement between our elastic scattering data and the TRIUMF data of Ref. 5 at both energies is found to be within  $\pm 10\%$ . In Figure 19 and Figure 20, the square points are our present data, the dotted points are previous TRIUMF data.

The focal plane response to the MRS was checked at 500 MeV using the elastic proton scattering on H in the polyethylene target. At the scattering angle of  $18^\circ$ , the elastic scattering events are measured in the first momentum bite and the second momentum bite. In the first bite, the elastic scattering events are found to be located in the high channel number part of our interesting focal plane region, while in the second bite, the events are found to be in the low channel number part of the interesting focal plane region. The two results agree well. At the scattering angle  $\theta = 26^\circ$ , the elastic scattering events are found in the high channel number part of the focal plane of the second momentum bite and in the lower channel in the third momentum bite. The resulting differential cross sections also agree well. As tabulated in table 1, the MRS focal plane responses in different focal plane regions, at different MRS settings, agree to within 3 %.

The results of the two normalization checks and the test of focal plane response of the MRS provides a basis for confidence in our experimental absolute cross section results. The following sections contain results of our proton inelastic scattering to the continuum and to the low-lying states together with discussion.

### 5.1 The Continuum at $E_p = 290$ MeV

The experimental data were taken in July, 1986 and formed the first part of the experiment. The data taken were  $4^\circ, 6^\circ, 8^\circ, 5^\circ, 12^\circ, 14^\circ$  for SAC and  $18^\circ, 22^\circ, 26^\circ$  for LAC. The entire spectrum at each angle for SAC was taken within one



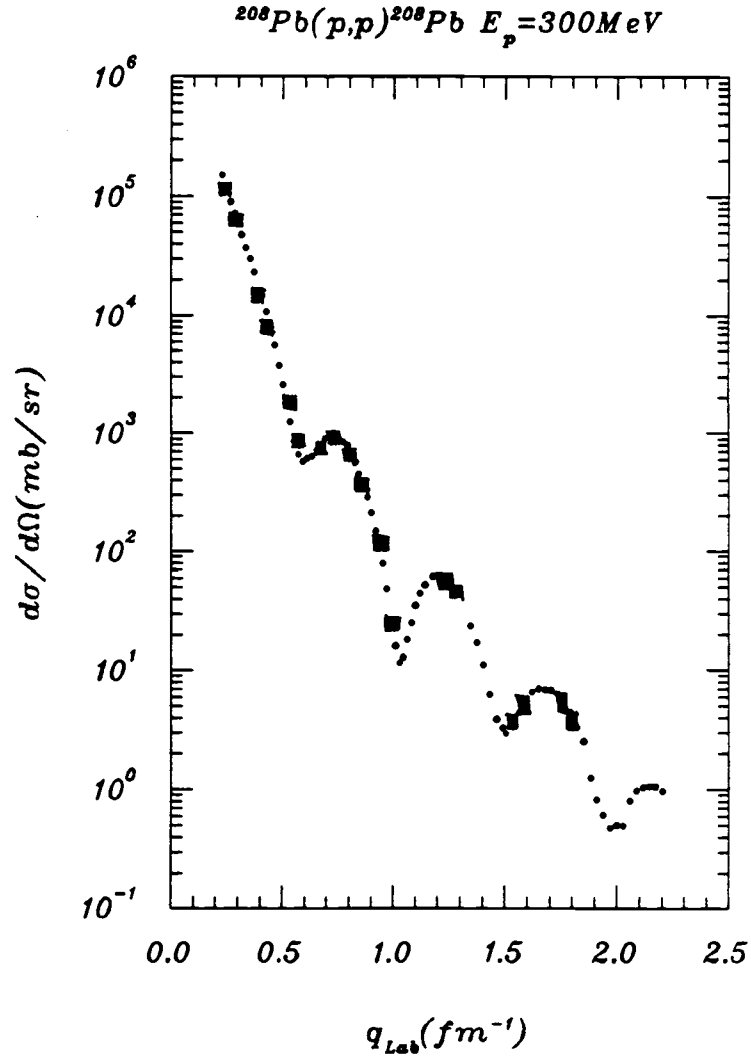


Figure 20: Normalization check using elastic  $p\text{-}^{208}\text{Pb}$  at  $E_p = 300 \text{ MeV}$

momentum bite. The measurements were completed using 3 different momentum bites at each angle for LAC. The quasifree peak positions (qsf) predicted from our empirical formula of eq. 9 are tabulated in table 2. The spectra of differential cross sections and analyzing powers at each angles are shown in Figure 21, 22, 23, 24, 25, 26, 27, 28 and 29.

In Figure 21 to 25(angles  $4^\circ$  to  $12^\circ$ ), the quasifree peaks are found to be in a region of excitation energy which also contains nuclear structures, while at angles above  $12^\circ$ , there is no appreciable nuclear structure in the region of the quasifree peaks. The analyzing power spectrum at each angle is calculated over an integration interval of 3 MeV to reduce the statistical uncertainties. The typical statistical errors for analyzing powers are  $\pm 10\%$ . The uncertainties of the normalization factor as described earlier in chapter 4 are the major contributions to the analyzing power errors. The analyzing power angular distribution for the quasifree peak is compared with RIA model calculations as shown in Figure 30. The points with error bars in Figure 30 are the experimental results. The two other curves are theoretical calculations. The experimental analyzing powers for the quasifree peak at  $14^\circ$ ,  $18^\circ$ ,  $22^\circ$  and  $26^\circ$  are taken directly from the analyzing power spectra at the corresponding angles. The quasifree peak positions are taken from table 2. In order to avoid contamination from the nuclear structure effects at angles  $4^\circ$  to  $12^\circ$ , semi-empirical quasifree spectra are calculated using the prescription of 9 drawn and fitted to the experimental differential cross section spectra of spin up and spin down at each angle. The smooth curves in Figure 31 are these phenomenological continuum spectra of spin up and spin down. As seen in the representative spectra of Figure 31, the giant resonance states dominate the region of 9 MeV to 25 MeV. One could also notice that the giant resonance structures are concentrated slightly more in spin up states than in spin down states. Quasifree peak positions could be better observed with the help of spin up and spin down

Table 1: The focal plane response to MRS at  $E_p=500$  MeV.

$\theta_{Lab}$	1 <sup>st</sup> bite	2 <sup>nd</sup> bite	3 <sup>rd</sup> bite
18°	19.0 (mb/sr)	18.7 (mb/sr)	—
26°	—	18.4 (mb/sr)	17.9 (mb/sr)

Table 2: Quasifree peak positions vs  $\theta_{Lab}$  at  $E_p=290$  MeV.

$\theta_{Lab}(^{\circ})$	qsf (MeV)
4	10.7
6	12.8
8	15.8
10	19.5
12	24.1
14	29.3
18	42.0
22	57.1
26	74.3

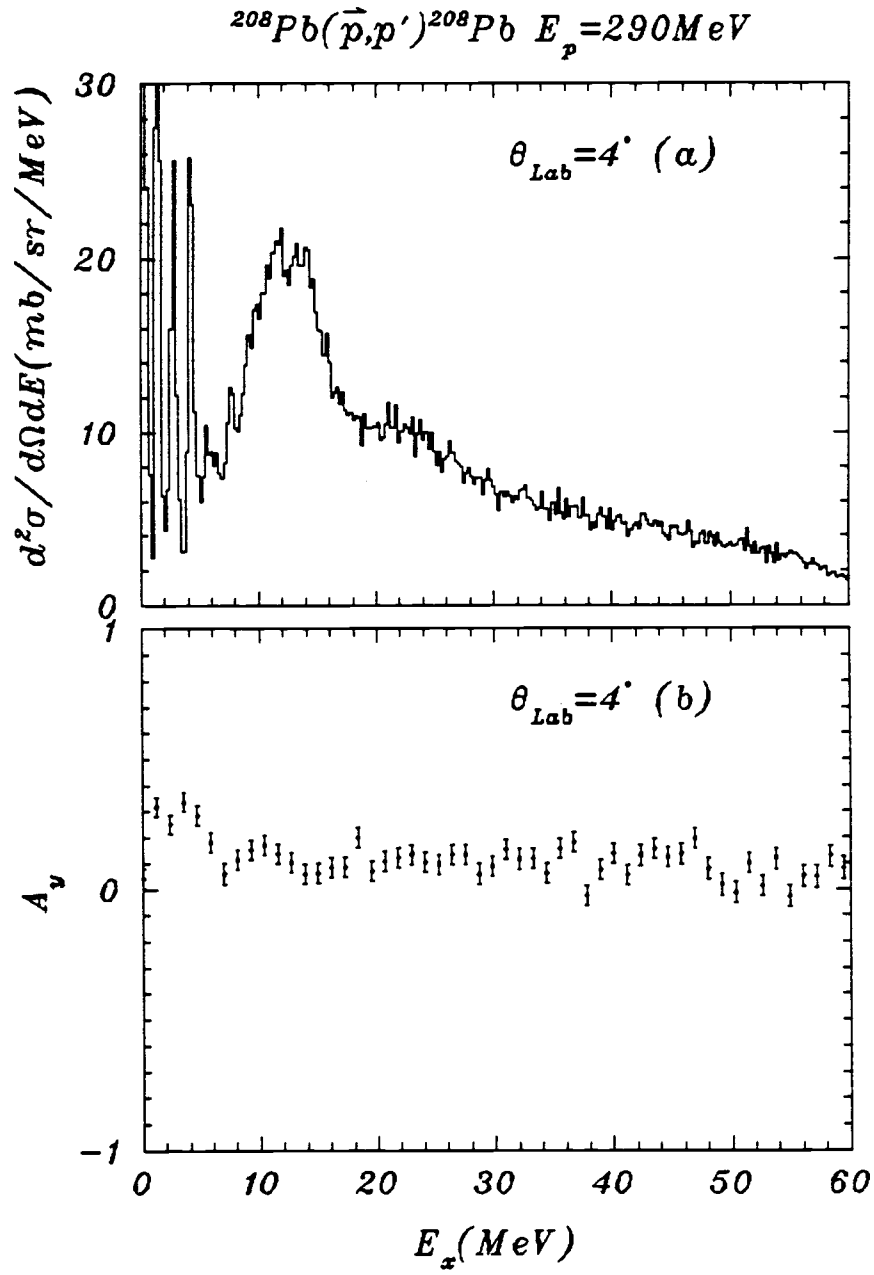


Figure 21: Continuum spectrum of  $\theta_{\text{Lab}} = 4^\circ$ ,  $E_p = 290 \text{ MeV}$

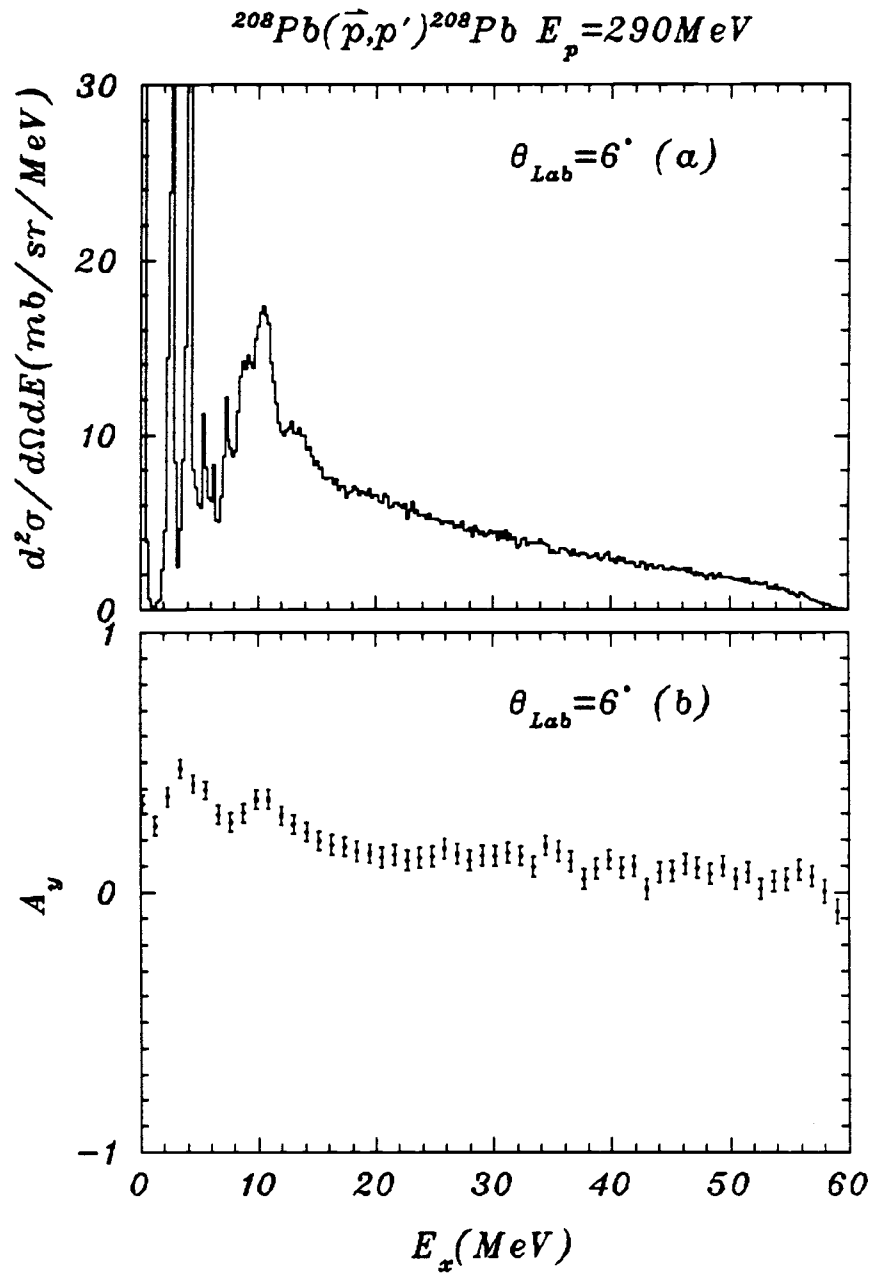


Figure 22: Continuum spectrum of  $\theta_{Lab}=6^\circ$ ,  $E_p=290 \text{ MeV}$

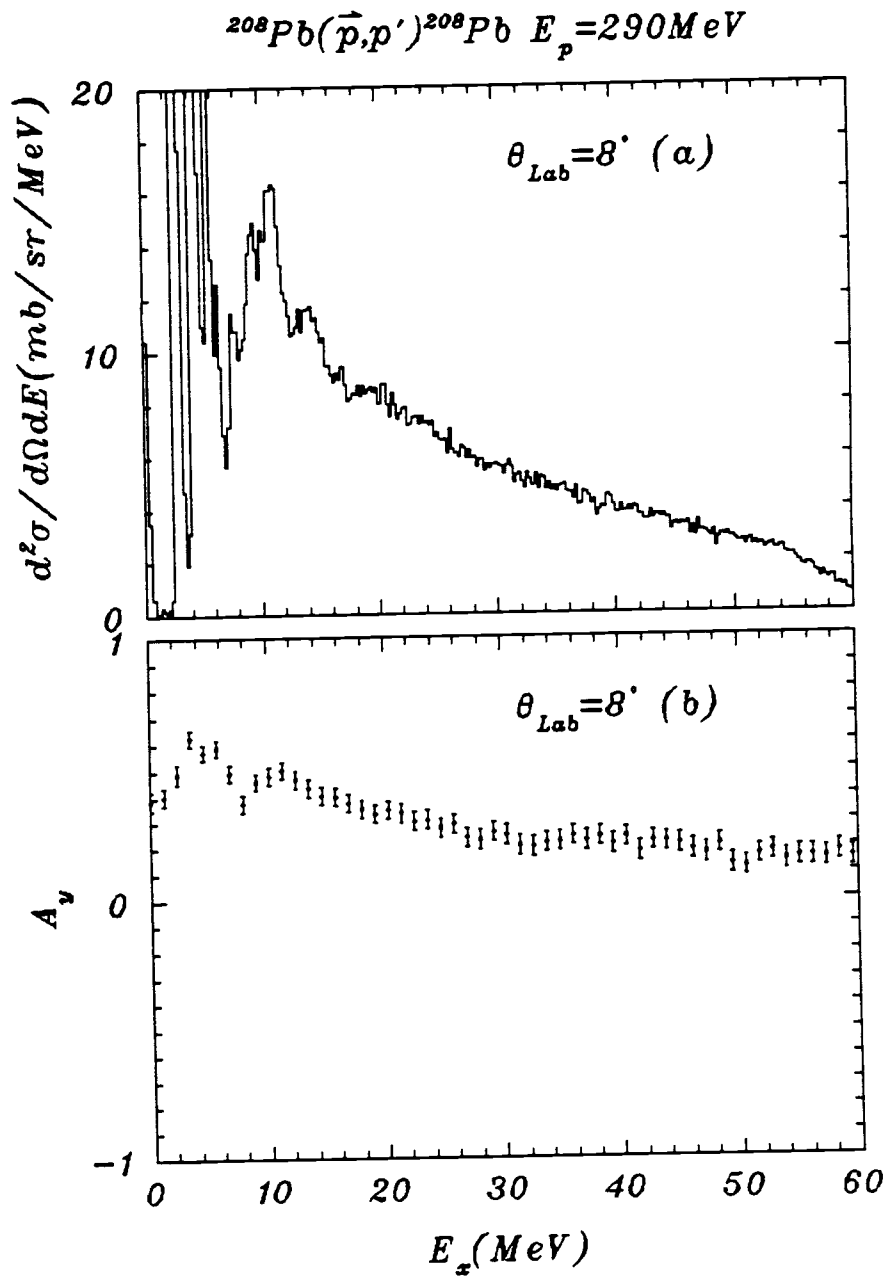


Figure 23: Continuum spectrum of  $\theta_{Lab} = 8^\circ$ ,  $E_p = 290$  MeV

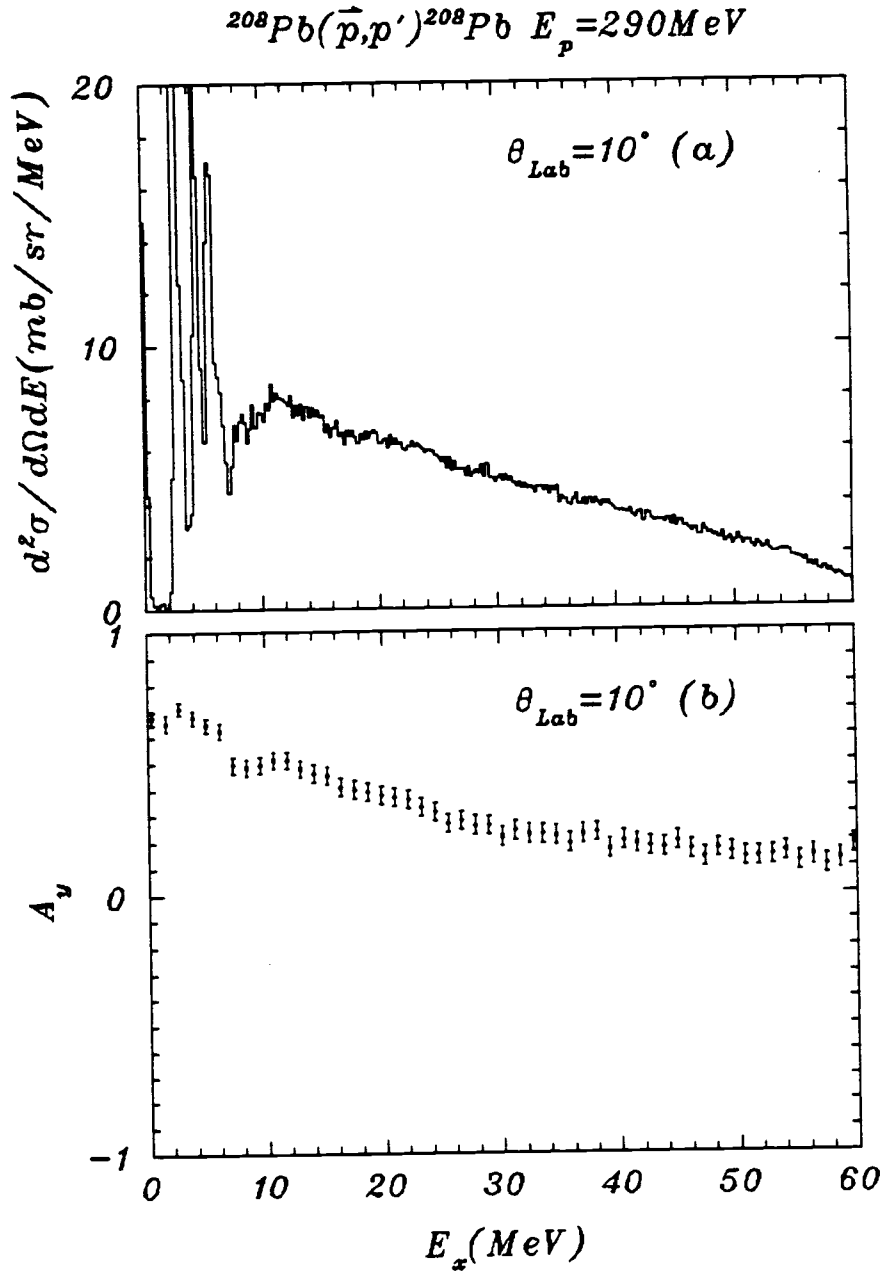


Figure 24: Continuum spectrum of  $\theta_{\text{Lab}} = 10^\circ$ ,  $E_p = 290 \text{ MeV}$

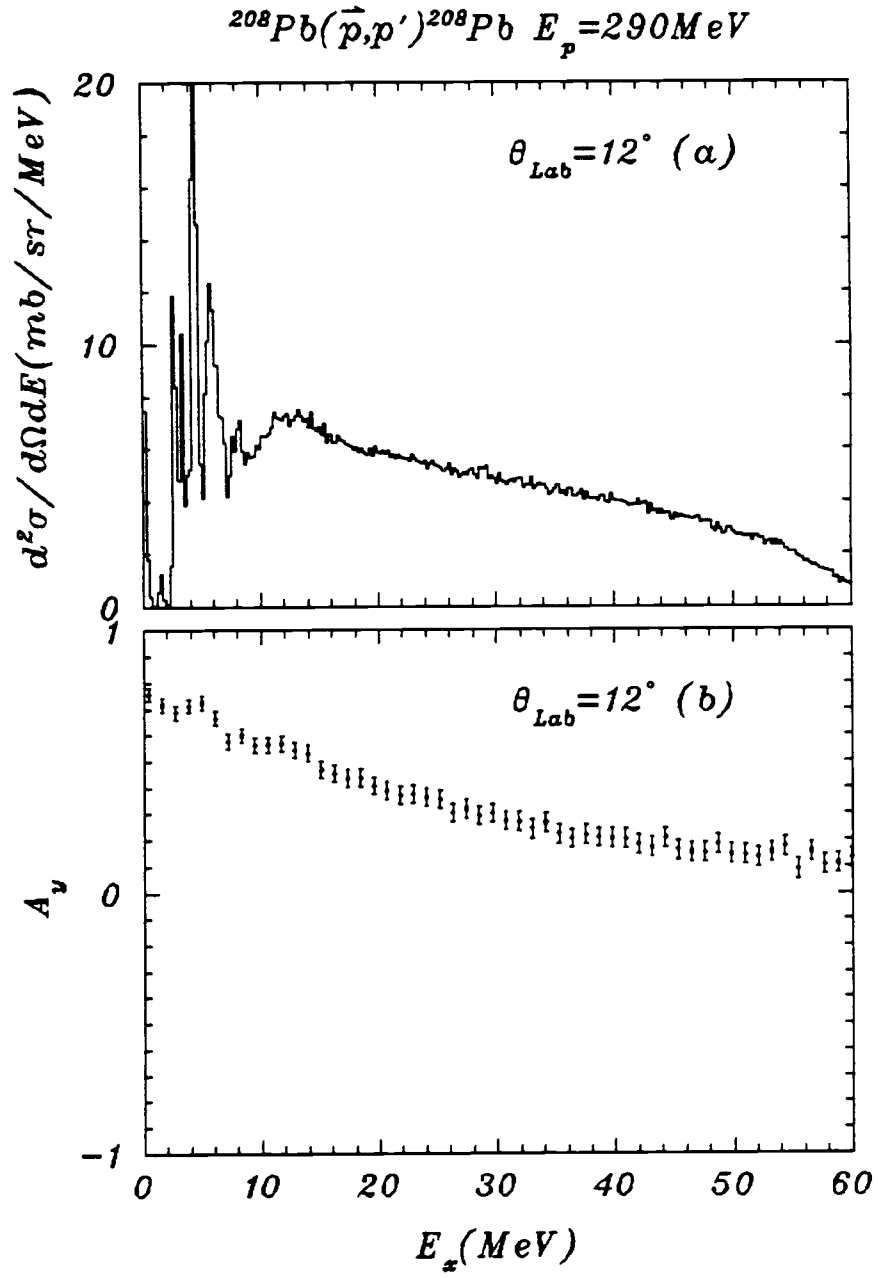


Figure 25: Continuum spectrum of  $\theta_{\text{Lab}} = 12^\circ$ ,  $E_p = 290 \text{ MeV}$



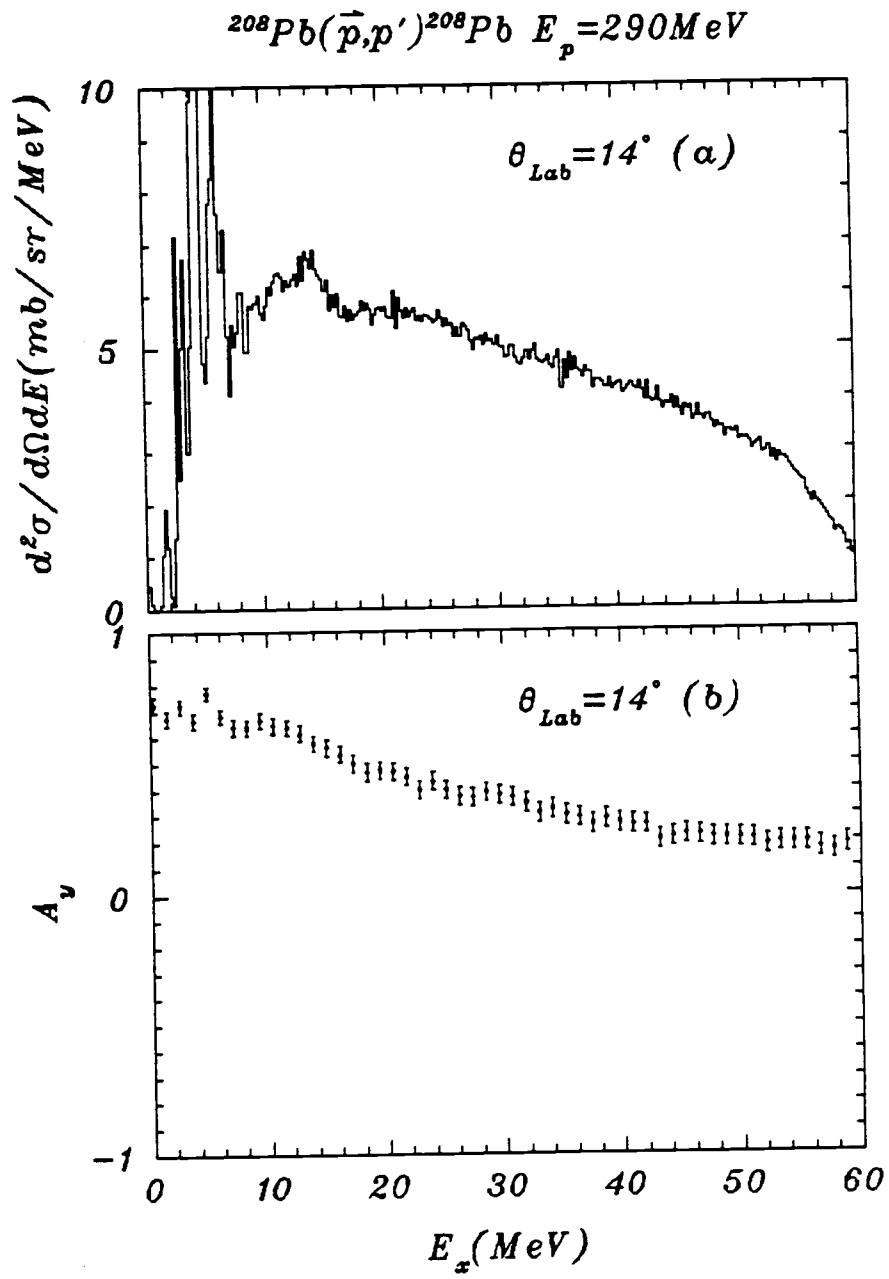


Figure 26: Continuum spectrum of  $\theta_{\text{Lab}} = 14^\circ$ ,  $E_p = 290$  MeV

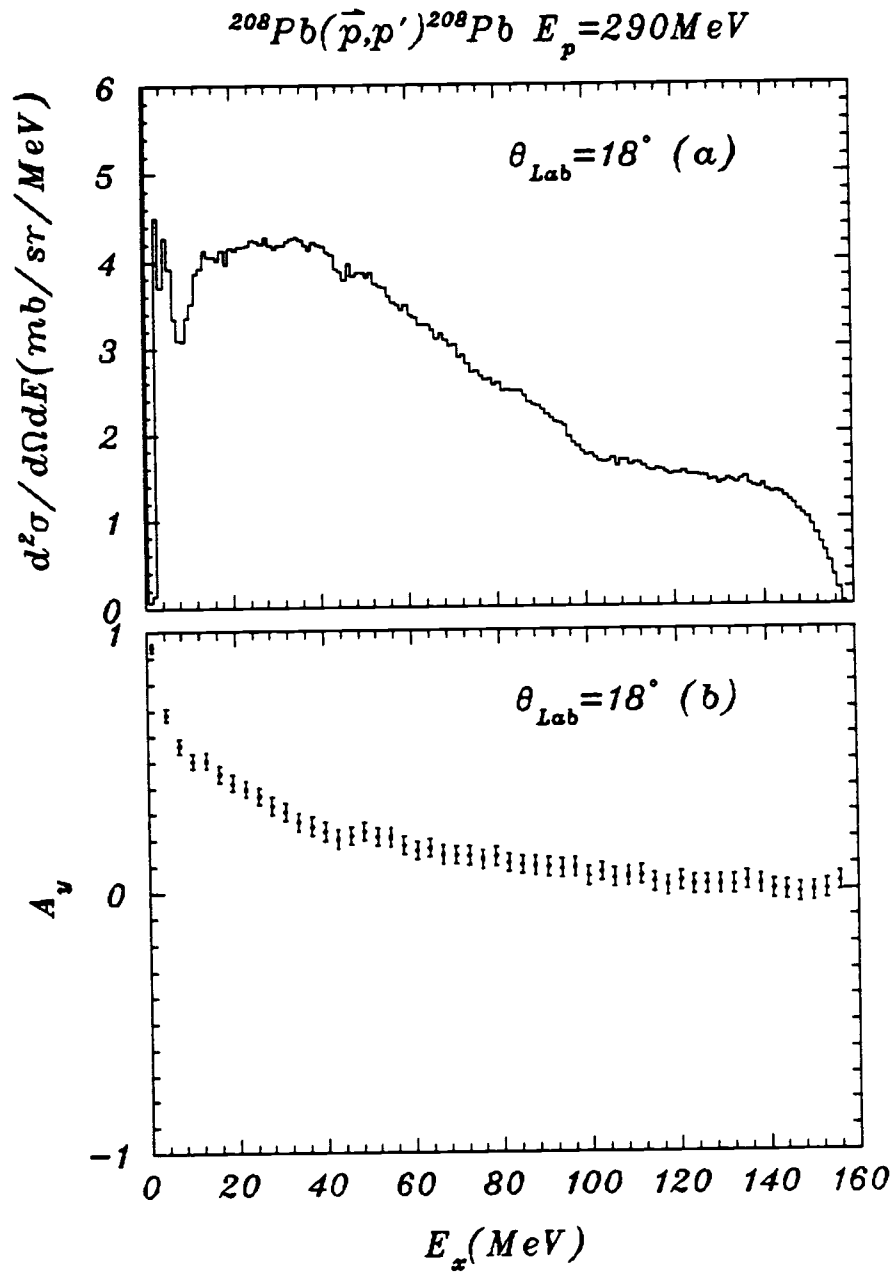


Figure 27: Continuum spectrum of  $\theta_{\text{Lab}} = 18^\circ$ ,  $E_p = 290$  MeV

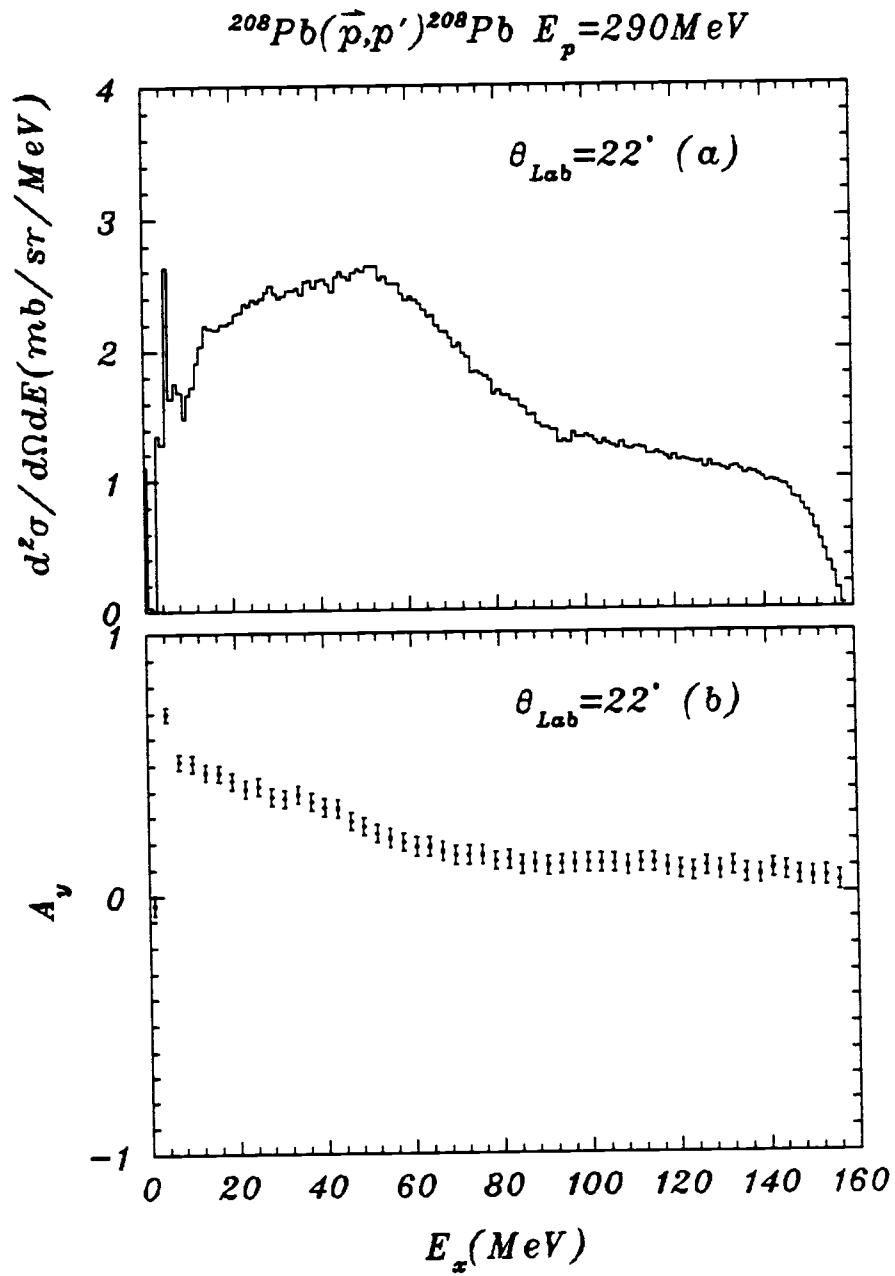


Figure 28: Continuum spectrum of  $\theta_{\text{Lab}} = 22^\circ$ ,  $E_p = 290$  MeV

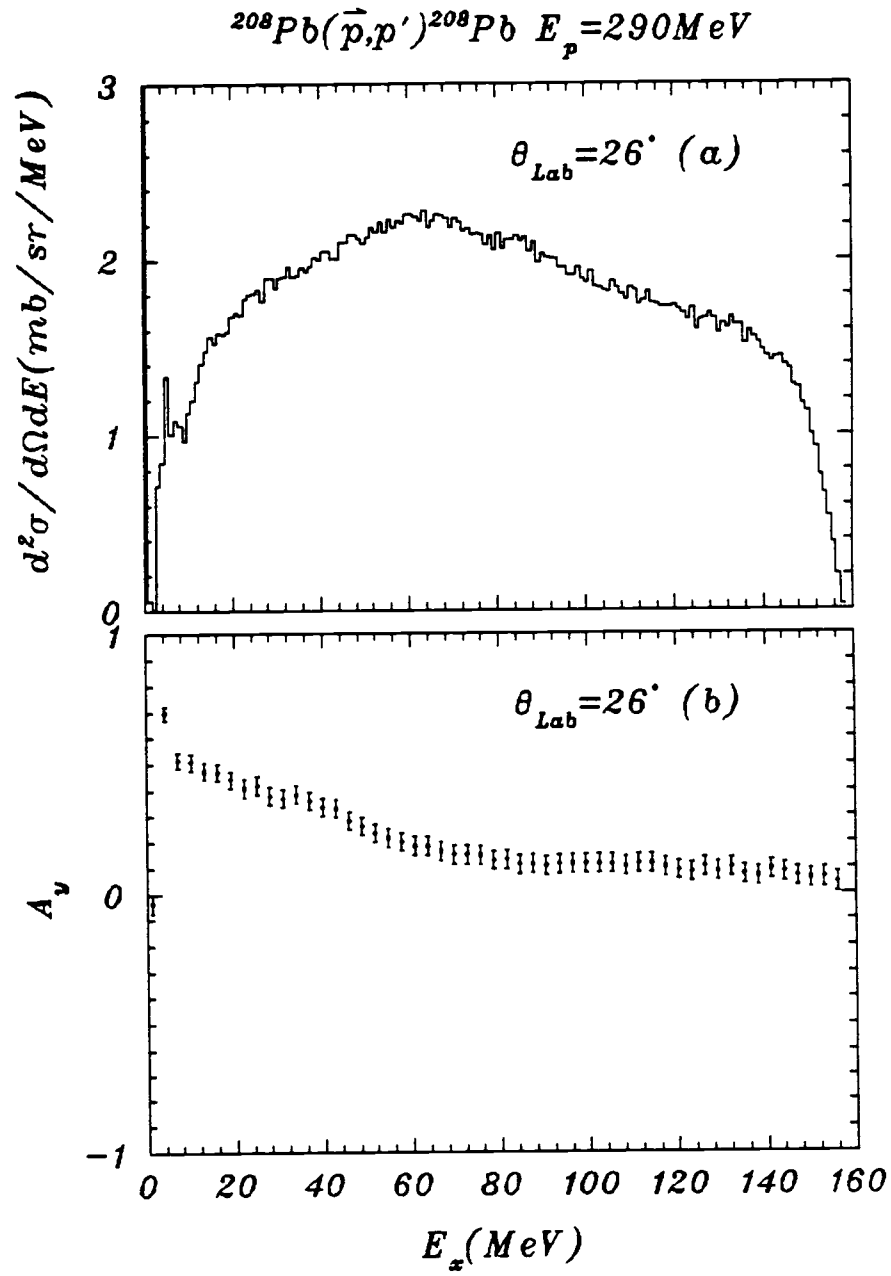


Figure 29: Continuum spectrum of  $\theta_{Lab} = 26^\circ$ ,  $E_p = 290 \text{ MeV}$

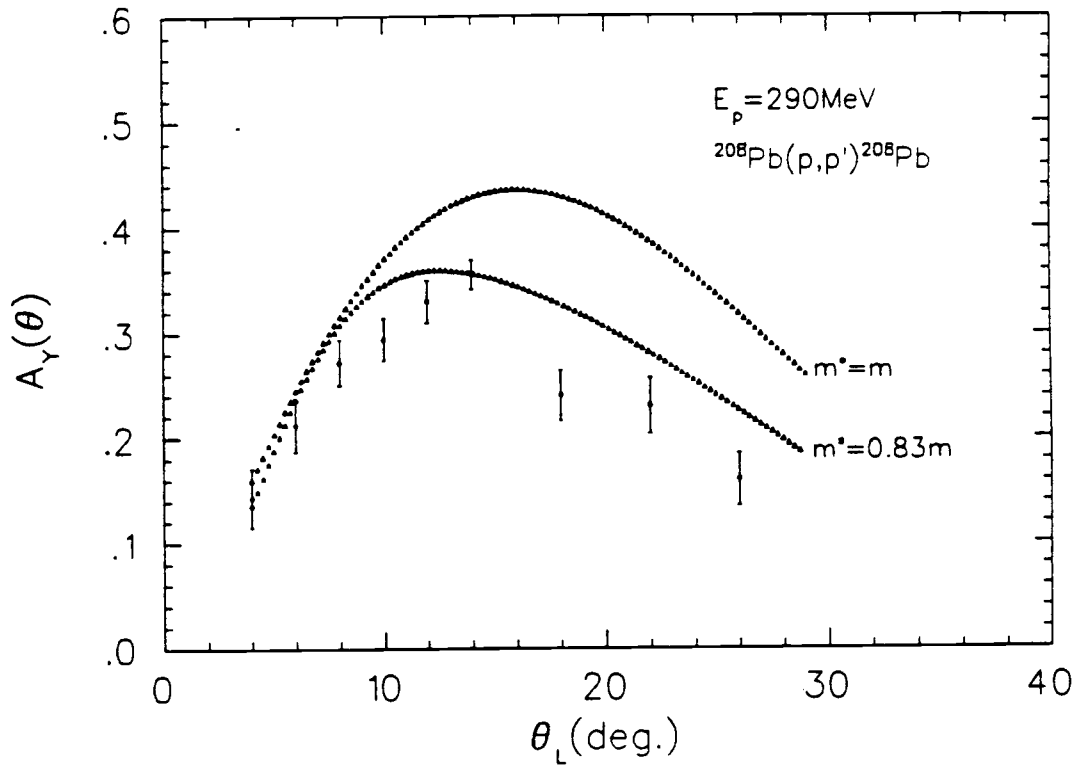


Figure 30: The  $A_y$  vs  $\theta$  of quasifree peak at  $E_p = 290$  MeV.

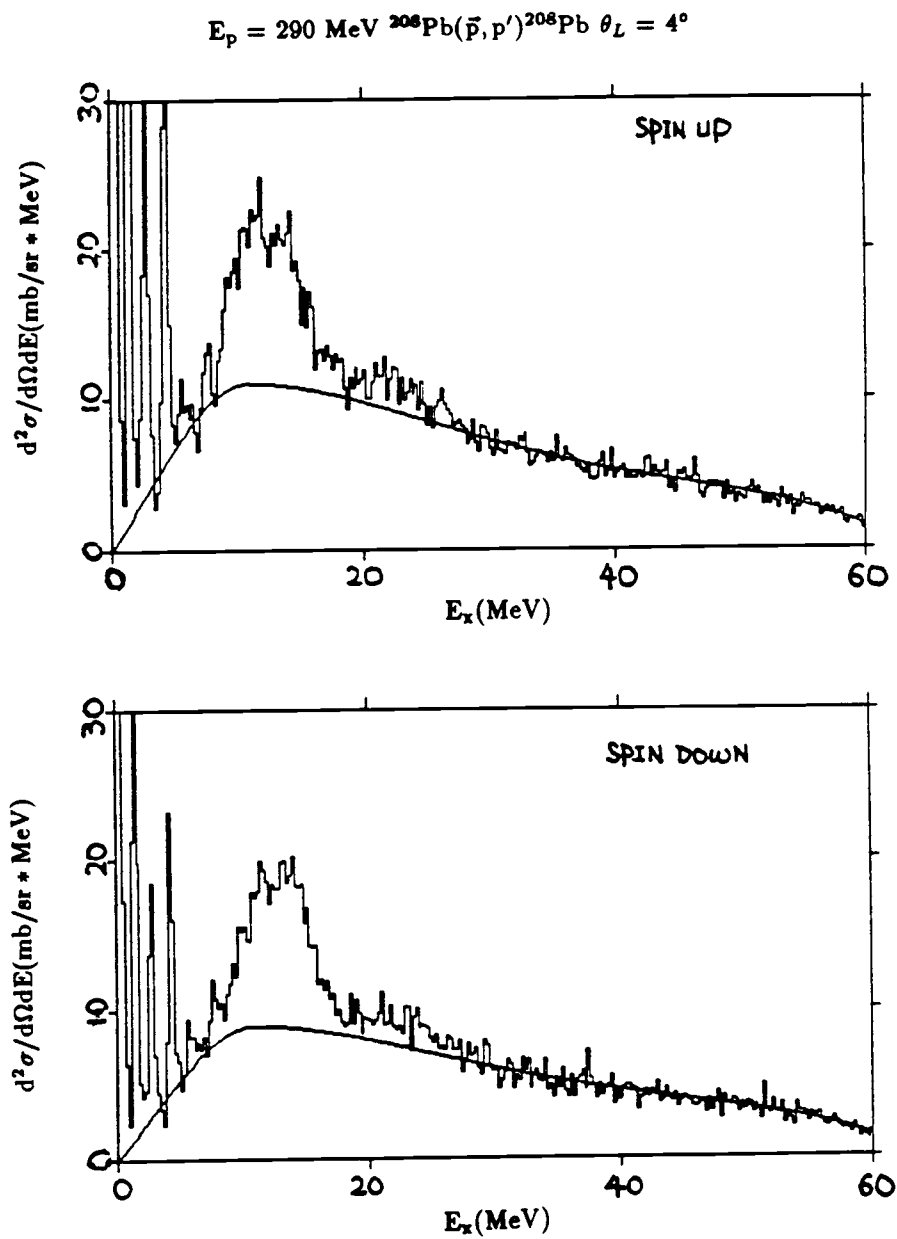


Figure 31: The spin up and spin down spectra of  $4^\circ$  at  $E_p=290 \text{ MeV}$

spectra than the spin off spectra.

The analyzing powers of quasifree peaks indicated in the Figure 30 at the angles of  $4^\circ$  to  $12^\circ$  are calculated from the empirical spectra (smooth curves) mentioned above to exclude contributions from nuclear structure effects in the low excitation energy region (from 9 MeV to 25 MeV). Drawing these curves may seem a little arbitrary, but this approach to the continuum technique has been used successfully in other studies. As an example, the empirical spectra have been drawn underneath giant resonances to subtract the continuum. The giant resonances parameters of  $^{208}\text{Pb}$  and  $^{28}\text{Si}$  so obtained are found to be consistent with the results from other laboratories, details are in ref. [21] and ref. [22].

It is interesting to see the overall behavior of analyzing power vs excitation energy at the available angles. As indicated in Figure 21 to 29, the analyzing power at each angle gradually decreases with increasing excitation energy. However, at the present time, there is no suitable model that can calculate the analyzing power over a broad range of excitation energy.

Figure 30 also shows RIA model calculations of  $A_y(\theta)$  vs  $\theta$  at the quasifree peak. The curve marked  $m^* = 0.83m$  is the calculation which includes the relativistic medium effects. The curve marked with  $m^* = m$  corresponds to the free NN case.

An alternate way to model the inclusive quasifree or continuum spectra is to use the semi-infinite slab surface response model of Bertsch, Schölton and Esbensen as mentioned in chapter 2. The spectra of experimental differential cross sections vs excitation energy are compared with the surface response calculations of this model in Figure 32. The comparison is shown at  $6^\circ$ ,  $10^\circ$  and  $26^\circ$ . The calculated spectrum at each angle is in agreement with the global shape of the experimental continuum spectrum. The magnitudes of spectra are theoretically overestimated. Renormalization factors (rnf) at the available angles are used to scale

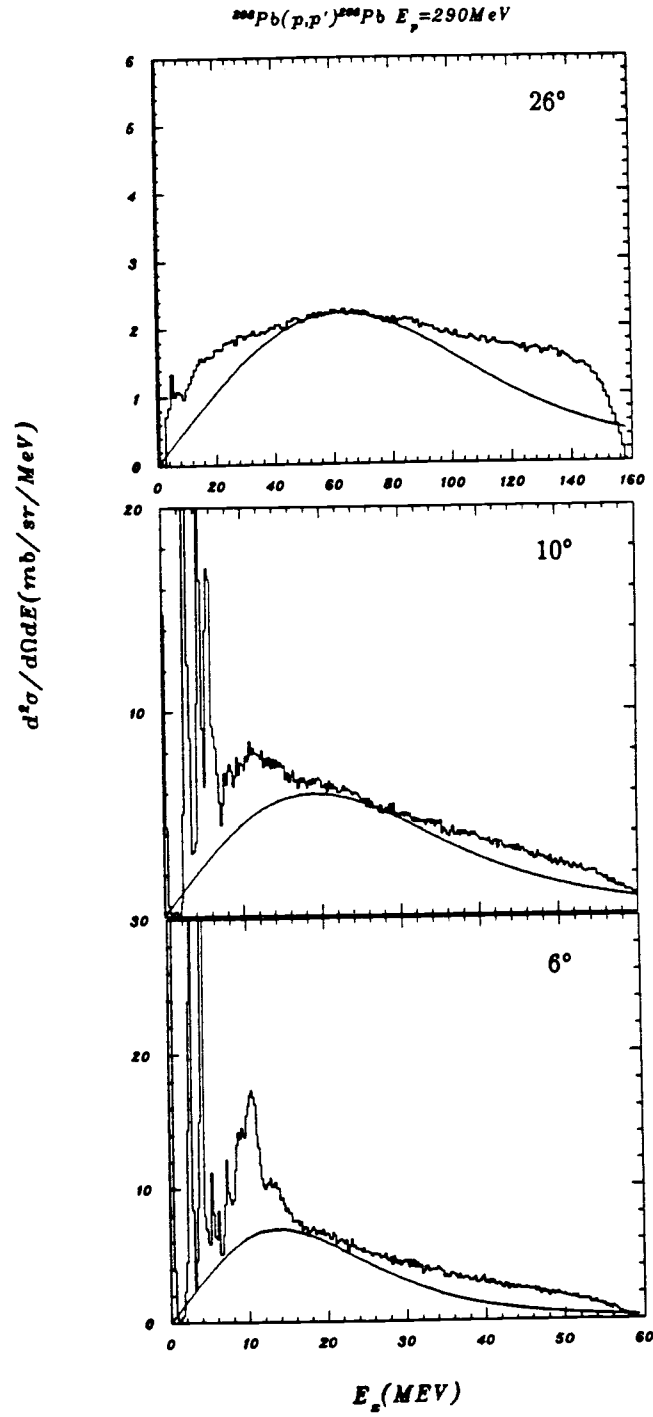


Figure 32: Representative data and surface response calculations at 290 MeV.



the theoretical continuum spectra down to the experimental values. The empirical renormalization factors (rnf) are tabulated in table 3. The theoretical continuum spectra are adjusted only in magnitude, so as to match as closely as possible the non-structure part of spectra beyond the giant resonance region. Peak positions remain unchanged after the renormalizations. This approach with renormalization has also been successfully applied to the study of giant resonances, details are in ref. [21] and [22].

## 5.2 The continuum at $E_p = 500$ MeV

The experimental data for the second part of the experiment were taken in July, 1987. The data were obtained at laboratory angles of  $5^\circ$ ,  $7^\circ$ ,  $9^\circ$ ,  $11^\circ$ ,  $13^\circ$ , for SAC and  $18^\circ$ ,  $22^\circ$ ,  $26^\circ$  for LAC. Efforts were made at this energy to take more data in LAC. Twice as many events were obtained at 500 MeV for large angles as obtained at 290 MeV. During the replay, data at each angle measured in LAC was angle rebinned into two angles, resulting in continuum data for the angles of  $5^\circ$ ,  $7^\circ$ ,  $9^\circ$ ,  $11^\circ$ ,  $13^\circ$ ,  $17^\circ$ ,  $19^\circ$ ,  $21^\circ$ ,  $23^\circ$ ,  $25^\circ$ ,  $27^\circ$  respectively. The analyzing powers were calculated for the same 3-MeV interval of excitation energy. The major contributions to the errors are the same as for the 290-MeV data. The double differential cross sections of spin off spectra and analyzing powers spectra calculated from eqs. (43) and (44) respectively are shown in Figure 33 to 43.

The quasifree peak positions (qsf) predicted from our empirical formula Eq. 9 are listed in table 4 together with qsf' which is the quasifree peak position observed from the experimental spectrum of spin up and spin down. The empirical peak predictions of Eq.9 at angles of  $5^\circ$  to  $13^\circ$  were in agreement with observations from cross section spectra of spin up and spin down. That is,  $qsf = qsf'$  for the  $5^\circ$  to  $13^\circ$  angular range. Discrepancies were found for angles between  $17^\circ$  and

Table 3: The renormalization of surface response calculations to the data at 290 MeV.

$\theta_L(^{\circ})$	rnf
4	1.0
6	1.0
8	1.3
10	1.1
12	1.25
14	1.1
18	1.0
22	0.9
26	1.0

Table 4: Quiafree peak positions vs  $\theta_L(^{\circ})$  at  $E_p=500$  MeV.

$\theta_L (^{\circ})$	qsf(MeV)	qsf'(MeV)
5	13.9	—
7	18.7	—
9	24.9	—
11	32.5	—
13	41.6	—
17	65.3	50.0
19	74.9	55.5
21	91.5	95.0
23	102.1	115.0
25	121.8	135.0
27	132.6	150.0

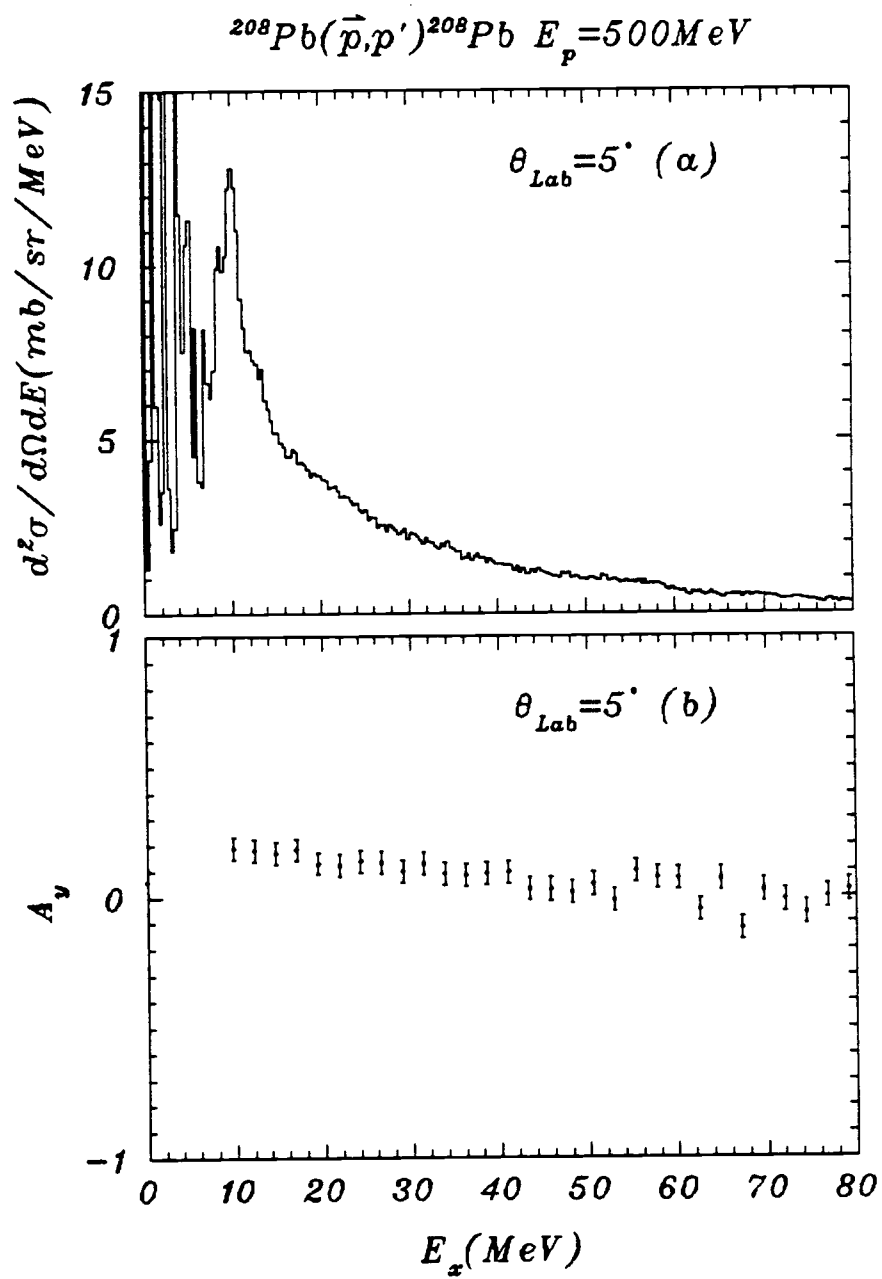


Figure 33: The continuum spectra of  $5^\circ$ , at  $E_p = 500$  MeV.

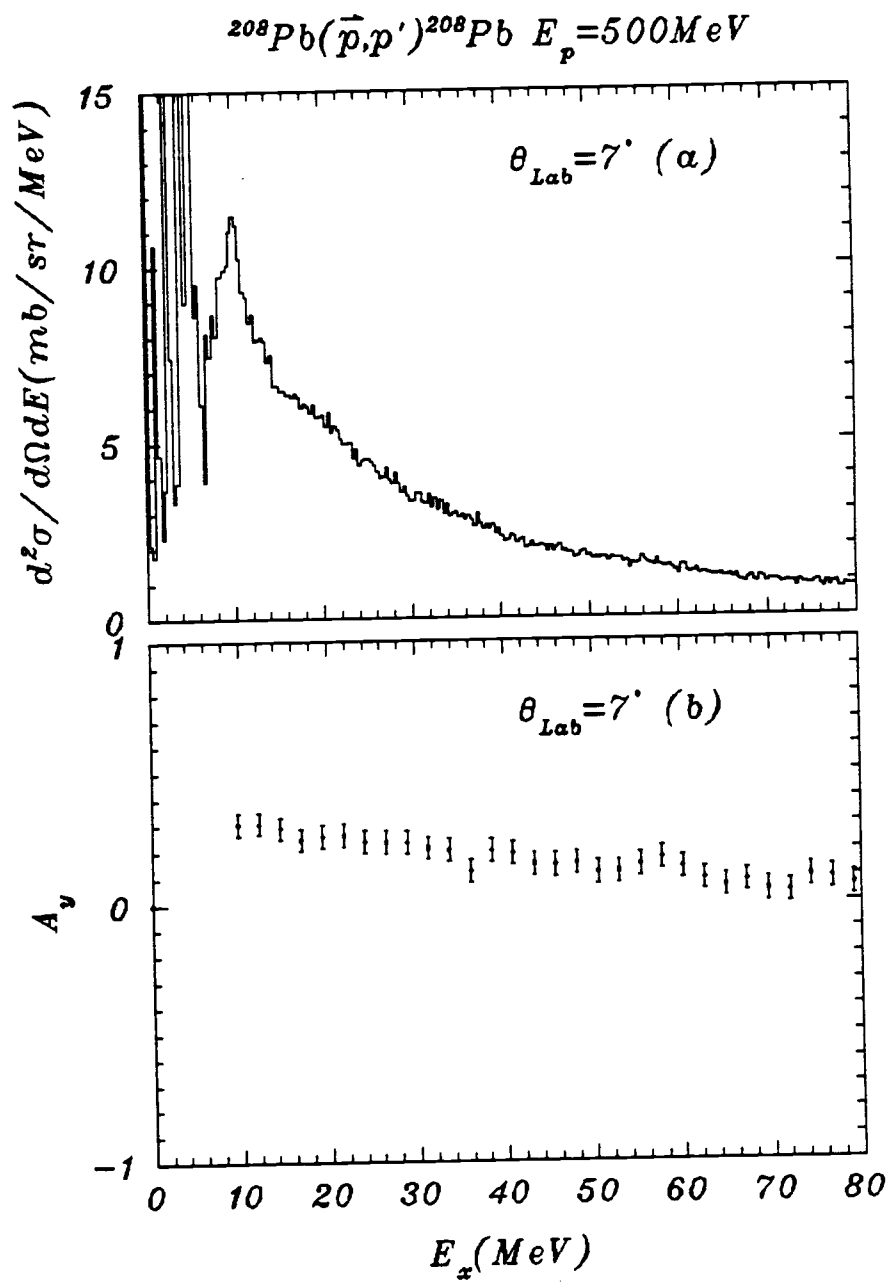


Figure 34: The continuum spectra of  $7^\circ$ , at  $E_p = 500 \text{ MeV}$ .

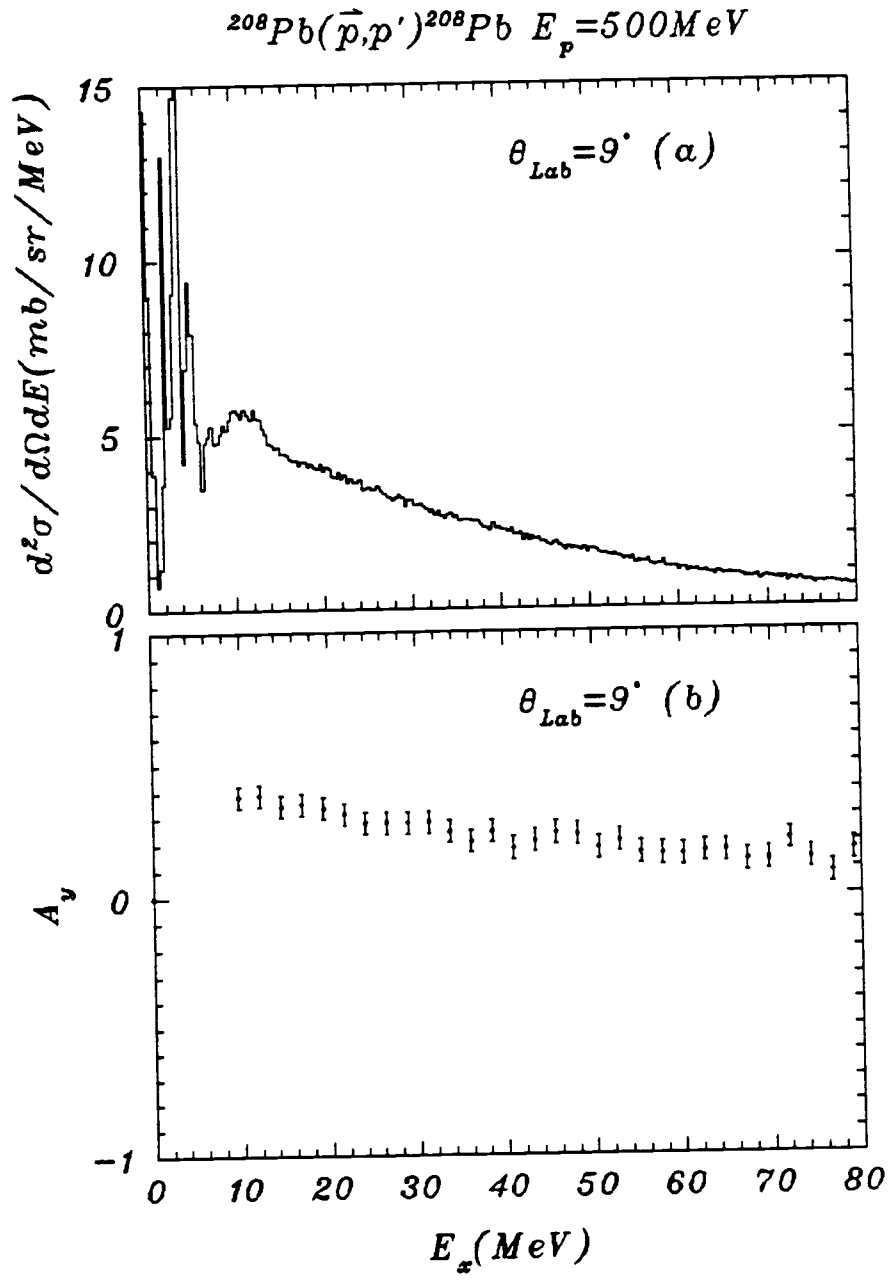


Figure 35: The continuum spectra of  $9^\circ$ , at  $E_p = 500$  MeV.

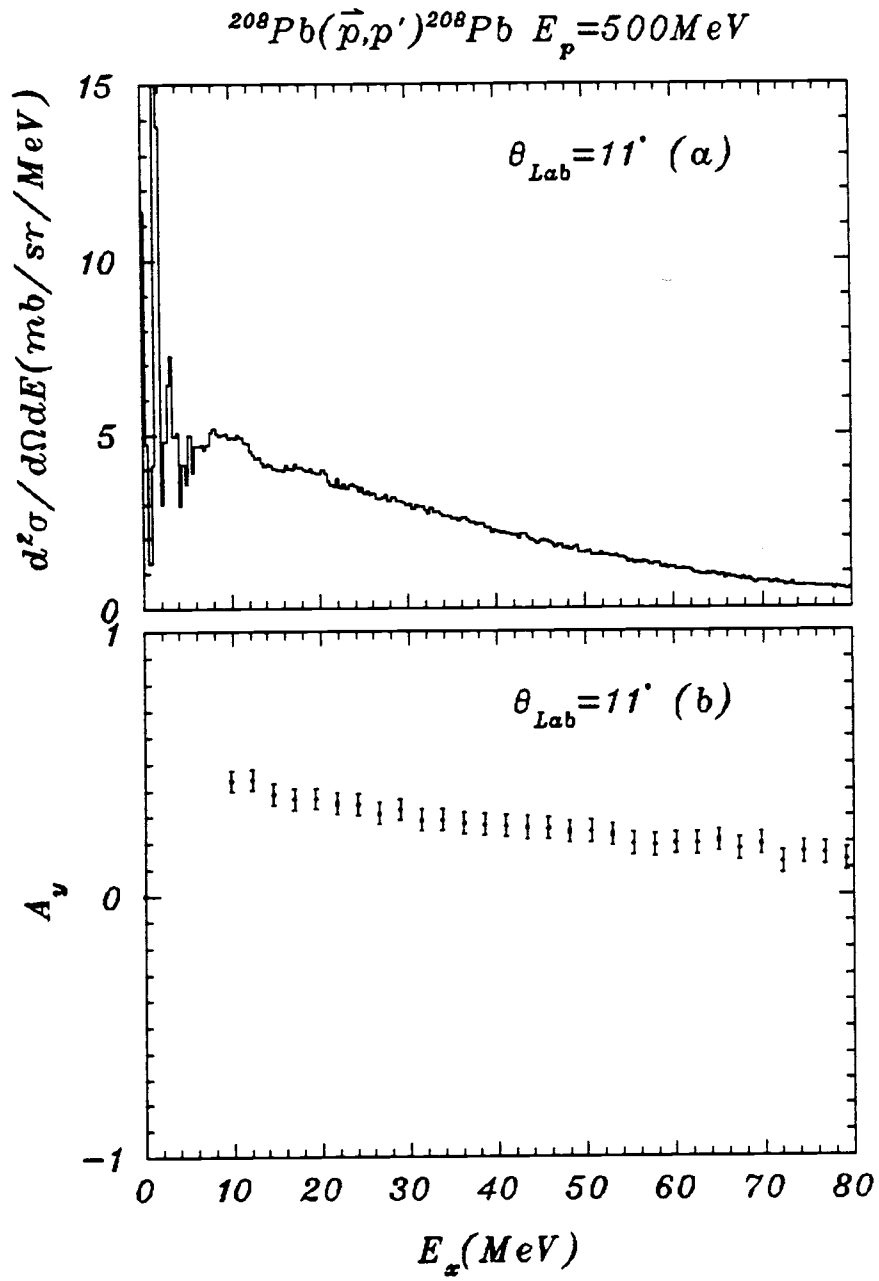


Figure 36: The continuum spectra of  $11^\circ$ , at  $E_p = 500 \text{ MeV}$ .

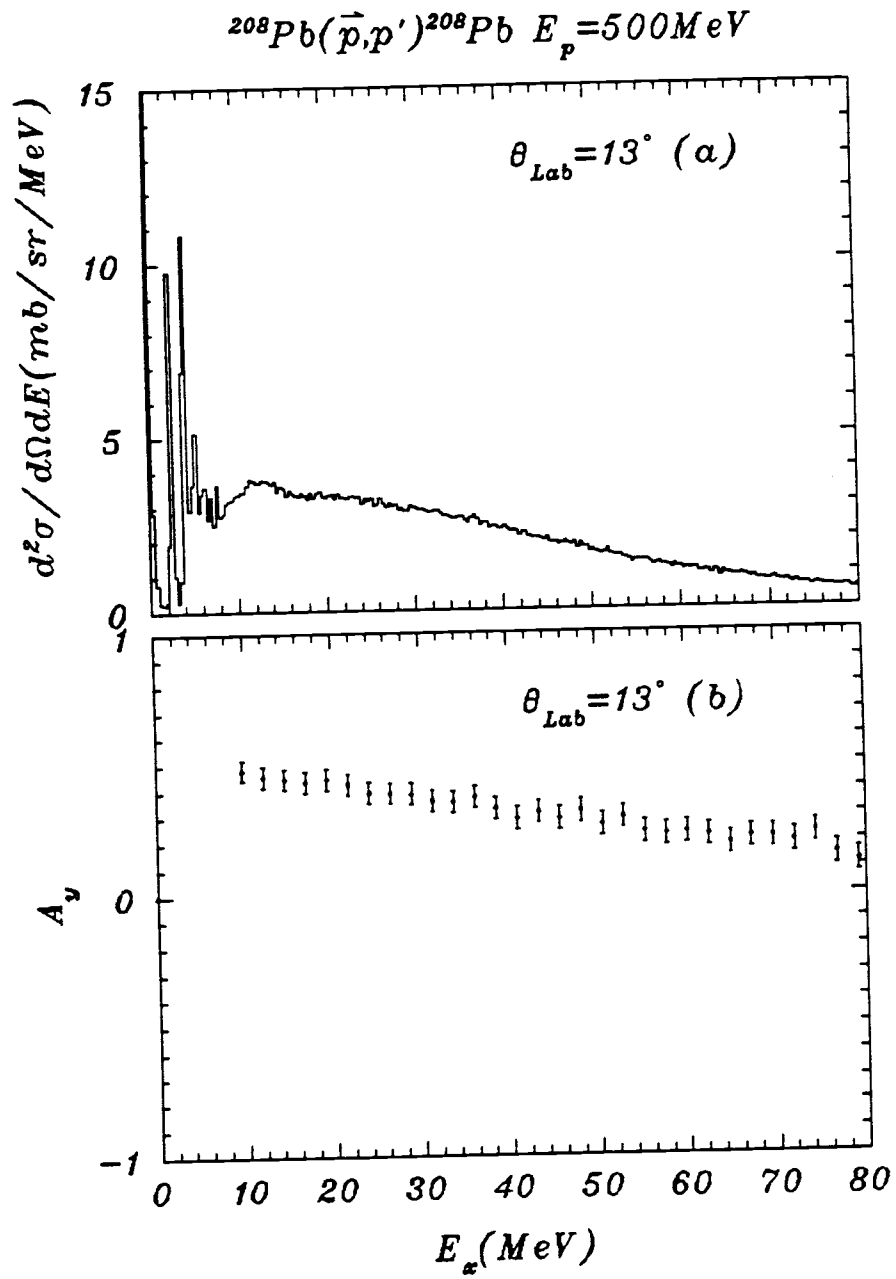


Figure 37: The continuum spectra of  $13^\circ$ , at  $E_p = 500 \text{ MeV}$ .

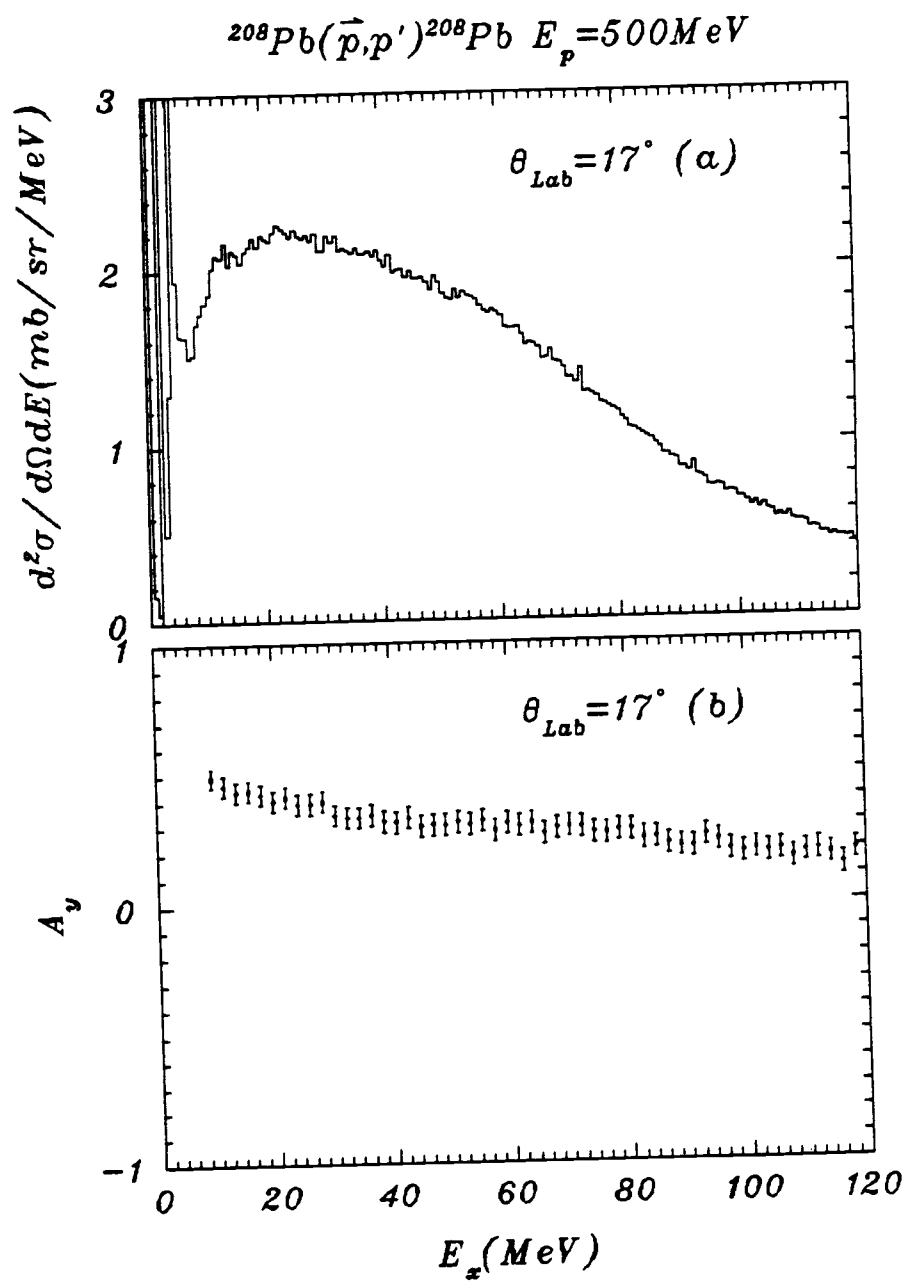


Figure 38: The continuum spectra of  $17^\circ$ , at  $E_p = 500 \text{ MeV}$ .



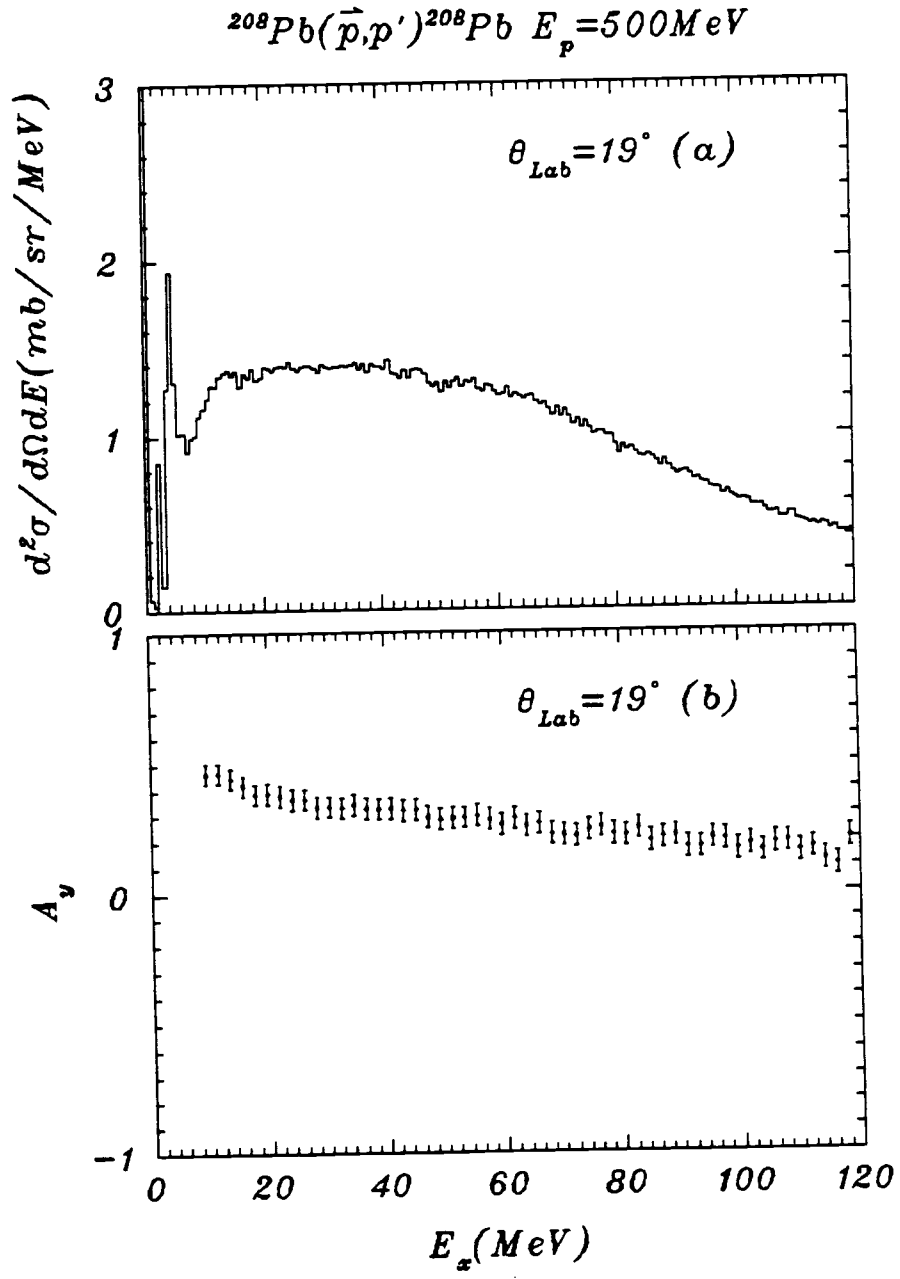


Figure 39: The continuum spectra of  $19^\circ$ , at  $E_p = 500 \text{ MeV}$ .

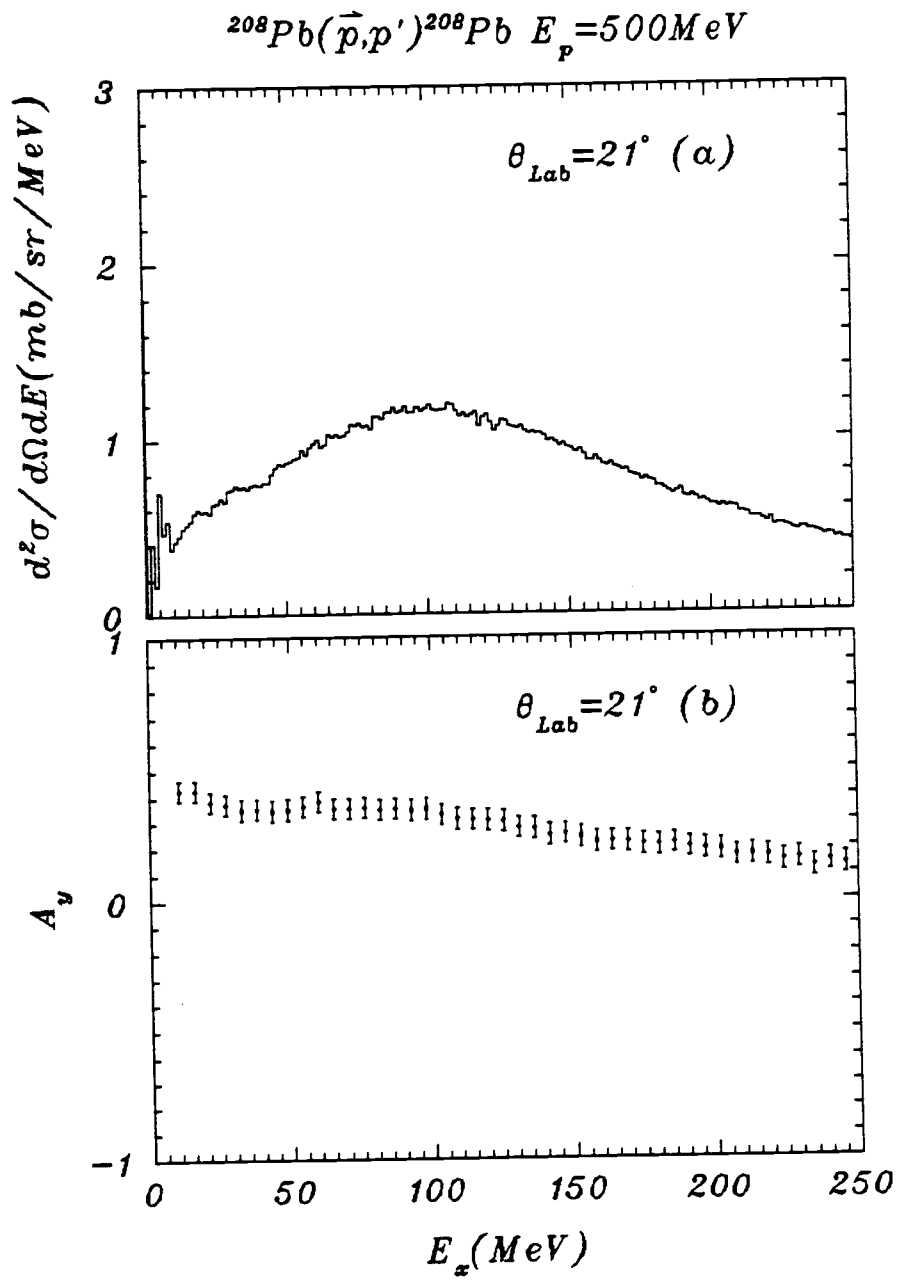


Figure 40: The continuum spectra of  $21^\circ$ , at  $E_p = 500 \text{ MeV}$ .

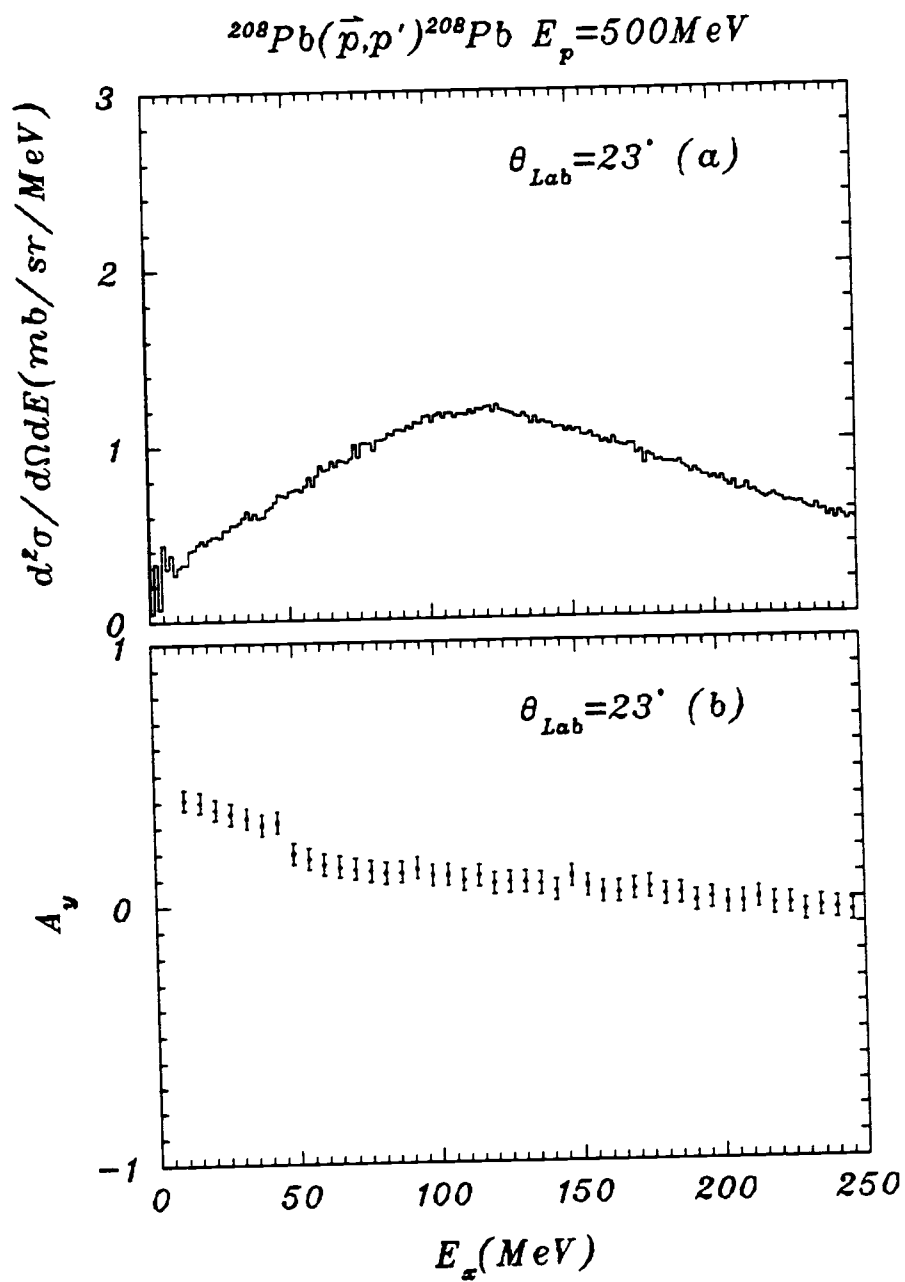


Figure 41: The continuum spectra of  $23^\circ$ , at  $E_p = 500 \text{ MeV}$ .

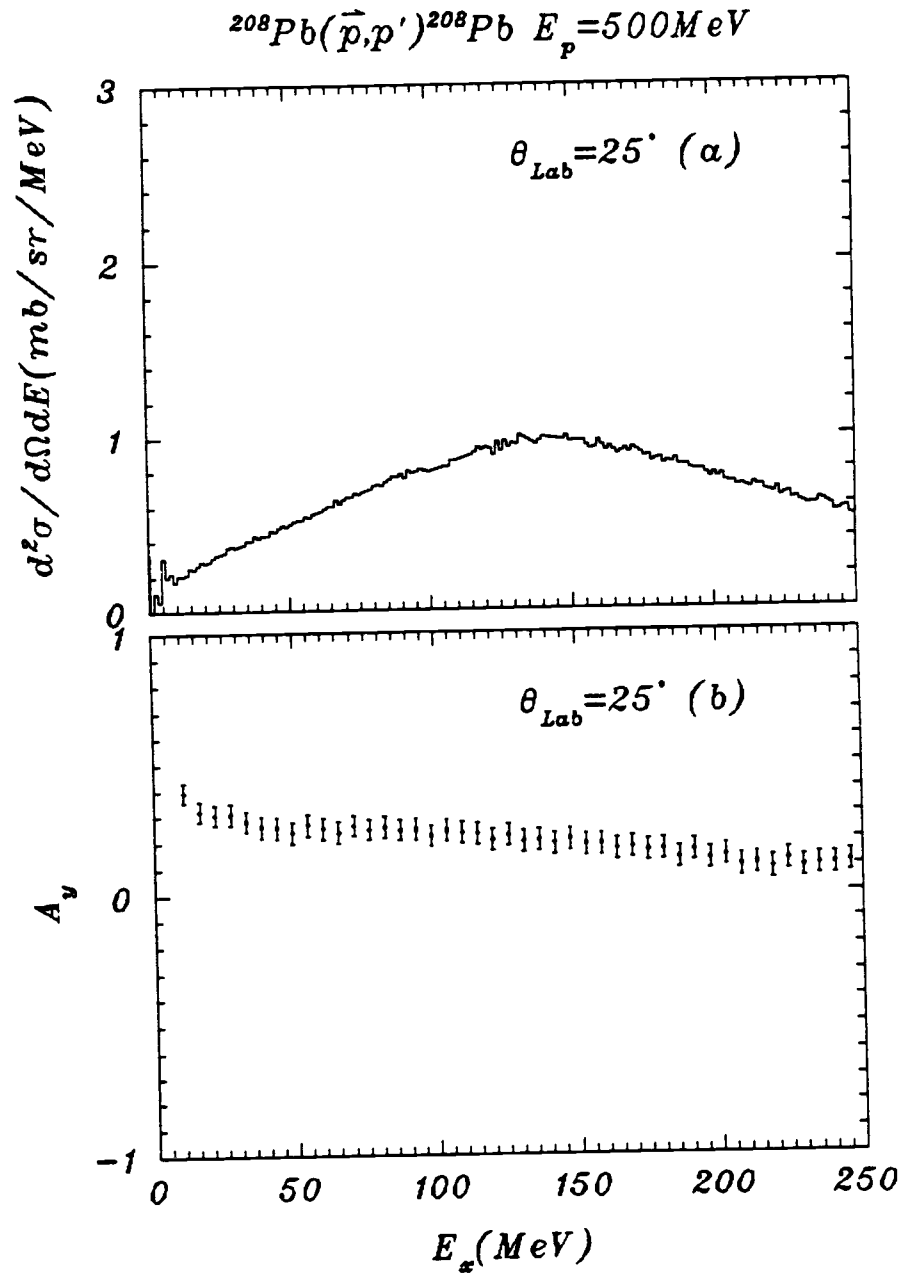


Figure 42: The continuum spectra of  $25^\circ$ , at  $E_p = 500 \text{ MeV}$ .

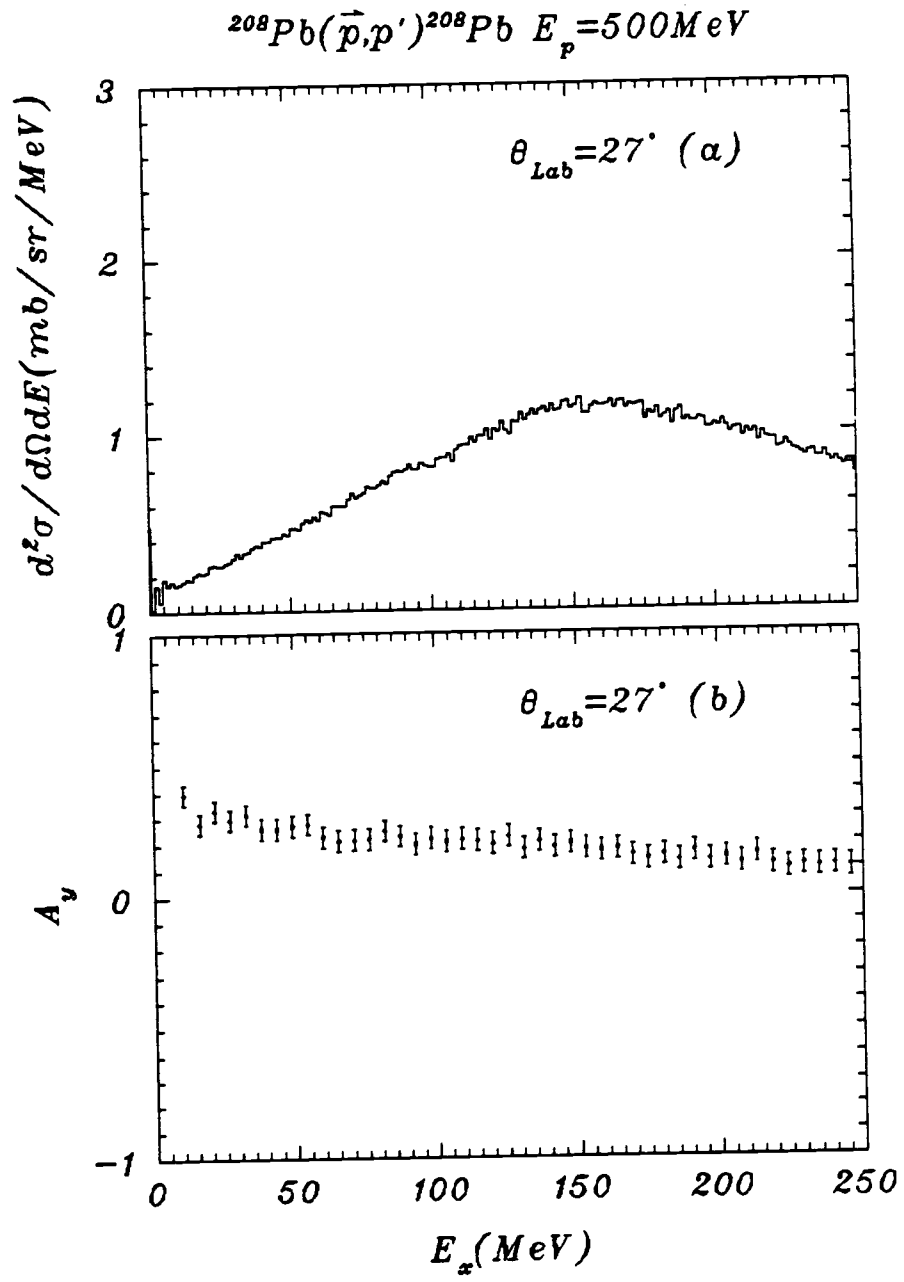


Figure 43: The continuum spectra of  $27^\circ$ , at  $E_p = 500 \text{ MeV}$ .

25°, where the observed quasifree peak positions  $qsf'$  from spin up and spin down spectra differ from the predicted peak positions  $qsf$ . The discrepancies can even be seen from the spin off double differential cross section spectra at angles above 19°, as shown from Figure 40 to 43. The upper spectra in figures are the spin off double differential cross sections and the lower spectra are the analyzing powers spectra. Unlike the data at 290 MeV, the quasifree peak positions at 500 MeV for the angular range studied are not obscured by nuclear structures. Therefore, no phenomenological or artificial model continuum spectra are needed to subtract out giant resonances contribution. The analyzing powers of quasifree peaks are taken directly from the energy distribution of analyzing powers shown in Figure 33 to 43. Since the quasifree peak positions predicted from the empirical formula Eq. (9) do not agree very well at high angles with the observed quasifree peaks, the  $A_y(\theta_L)$  of the quasifree peaks at high angles are calculated at the observed positions  $qsf'$ . The empirical peak prediction Eq.(9) is still applied at low angles, that is, below 21°, where  $A_y(\theta_L)$  for the quasifree peaks are calculated at position  $qsf$  (as listed in table 4) at each angle. The measured analyzing power angular distribution of the quasifree peak so obtained is shown in Figure 44 along with the RIA model calculations. The curve marked  $m^* = 0.86m$  is the calculation with relativistic effects, the other curve marked  $m^* = m$  corresponds to free NN scattering.

The differential cross section spectra are comparing with the surface response model calculations at 5°, 9° and 25° in Figure 45. The histograms in Figure 45 are the experimental differential cross sections, the smooth curves are the surface response model calculations. The model calculations over estimate the cross section spectra in magnitude, but the shape of continuum spectra are well reproduced. Renormalizations of the theoretical calculations to the experimental spectra are performed at each angle. The rnf (renormalization factor) at each angle is listed

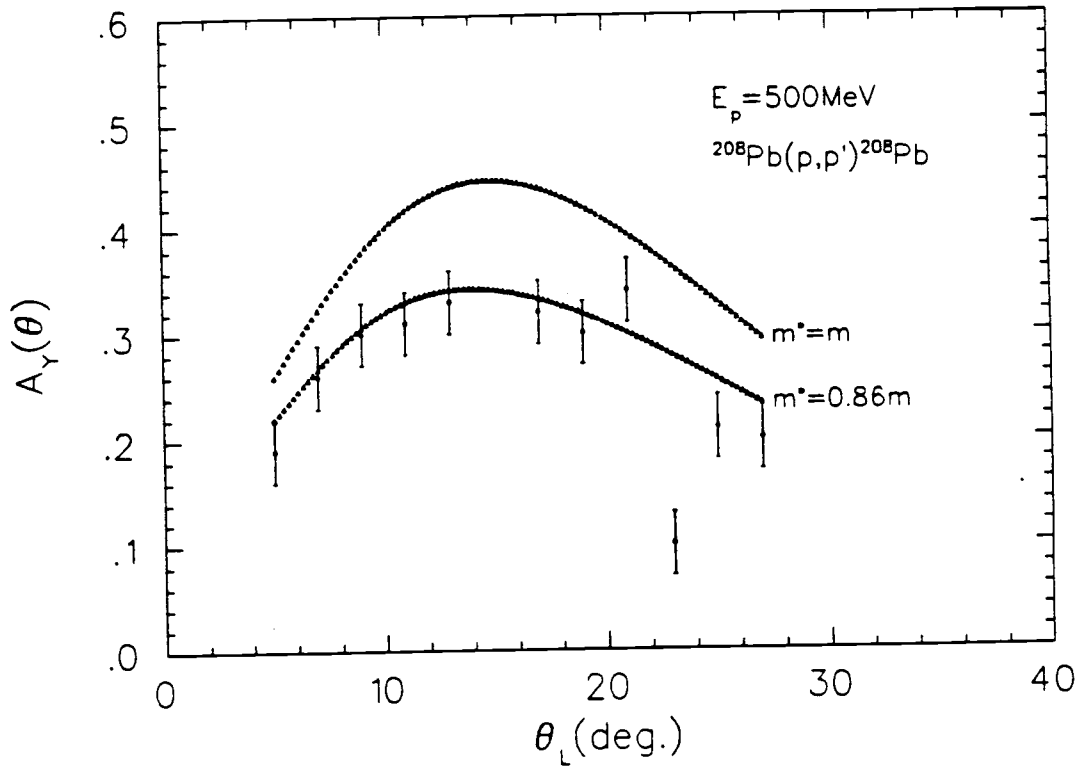


Figure 44: The  $A_y(\theta_L)$  vs  $\theta$  of quasifree peaks at 500 MeV.

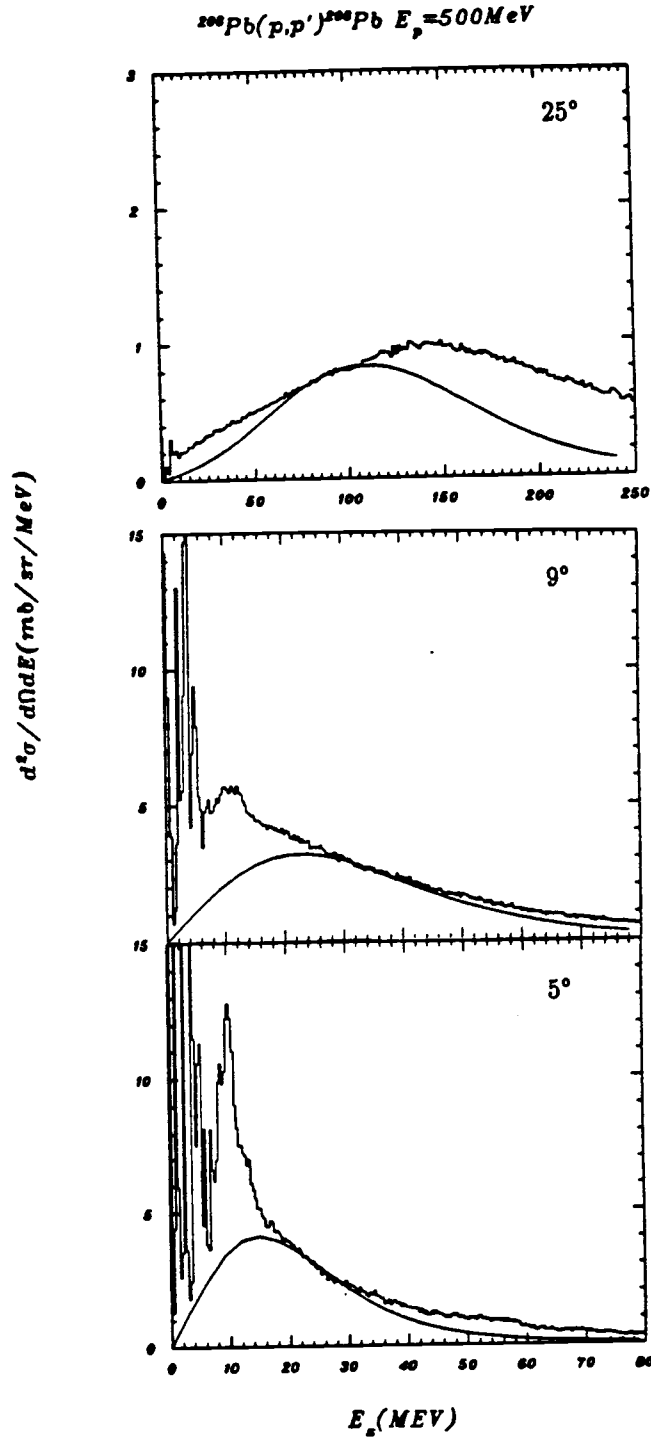


Figure 45: Representative data and surface response calculation at 500 MeV.



in table 5.

### 5.3 Discussion of Continuum Results

The shape of the experimental cross section spectra plotted as  $d^2\sigma/d\Omega dE$  vs  $E_x$  (excitation energy) can be reasonably described by the surface response calculation. The calculated model cross section is scaled down by approximately a factor of 1.2 at  $E_p = 290$  MeV and 2.0 at  $E_p = 500$  MeV. The surface response model calculations described here considered only the single-step quasifree processes, multi-step processes are not taken into account. In the model used here only the free surface response was included, the residual interaction contributions were omitted. In summary, the experimental cross section spectra can be described qualitatively by a free surface response model calculation based on the single-step quasifree processes. At higher excitation energies, multiple scattering can be important. Clearly, more complete theoretical calculations are required to provide better agreement.

The experimental analyzing power angular distributions at the quasifree peak  $A_y(\theta)$  vs  $\theta_L$  are compared with free NN values and model calculations. The experimental  $A_y(\theta)$  at the quasifree peaks was obtained with the help of an empirical method of locating quasifree peak positions, direct observation of quasifree peak positions, empirical continuum spectra and model calculations of continuum spectra. An effort has been made to maintain a systematic approach throughout the analysis. Most of the quasifree-peak analyzing powers are calculated using the directly observed continuum spectra except for 290-MeV data at low angles. The experimental quasifree-peak analyzing power angular distribution results are lower than the free NN values especially at large angles. An interpretation may be that the  $A_y(\theta)$  vs  $\theta$  observable is very sensitive to nuclear medium effects. The RIA

model calculation is based on the Dirac approach, nucleon-nucleon scattering amplitude in the medium, and the single-step quasifree processes. The medium effects are characterized through the use of an effective mass  $m^*$ , which is proportional to the average scalar potential. The replacement of the free nucleon mass  $m$  to the effective nucleon mass  $m^*$  enhances the lower components of the Dirac spinors. Therefore, it is expected under this model assumption that the spin observables of inclusive quasifree scattering will be different from free NN values. According to the theoretical calculations of Horowitz and Iqbal [3], an effective nucleon mass, due to the medium effects  $m^* = 0.83m$  at 290 MeV,  $m^* = 0.86m$  at 500 MeV and  $m^* = 0.90$  at 800 MeV is expected for  $^{208}\text{Pb}$ . The effective mass is predicted to be closer to the free nucleon mass  $m$  at higher incident proton energy. Comparing our analyzing power results with the free NN values ( $m^* = m$ ) and RIA predictions, the free NN values ( $m^* = m$ ) at both proton energies over estimate the experimental data while the RIA calculations are in acceptable agreement with the experimental  $A_y(\theta)$  results at the quasifree peak. Efforts were also made to use the free surface response model to calculate the analyzing powers at the quasifree peak, but due to cancellations of the free surface response medium corrections, the resulting analyzing powers are not different from the free NN values. Whether the addition of multi-step quasifree processes and residual interaction considerations could reproduce our experimental analyzing power angular distribution results is at present unknown.

Recently Smith [14] successfully reproduced the experimental (n,p) scattering continuum cross section data and (p,p') spin-flip scattering continuum cross section data using a semi-infinite slab surface response model which included residual interactions and second-step quasifree processes. The improvements obtained by considering residual interactions are rather significant for the (n,p) and spin-flip (p,p') reactions. However, the semi-infinite slab free surface response model

better reproduces the global shape of inclusive  $(p, p')$  scattering cross section data. The reason for this difference is not clear, but two possibilities are the usage of the semi-infinite slab approximation for finite nucleus system, or the approach used to include residual interactions in the spin zero channel and isoscalar isospin channel.

Analyzing powers plotted as a function of excitation energy at each angle at both incident energies showed negative slope across the continuum. This damping of the analyzing power with increasing excitation energy may possibly be due to the residual interactions, but efforts must be made to improve theoretical models in order to understand the experimental results.

According to our experimental results, the inclusive proton scattering to the continuum is found to be dominated by single-step quasifree scattering. At  $E_p = 290$  and 500 MeV, the continuum spectra of  $^{208}\text{Pb}$  can be qualitatively described by non-relativistic impulse approximation. Our experimental results strongly indicate the presence of relativistic medium effects as represented by the effective mass ( $m^*$ ) of a nucleon in the nuclear medium. Analyzing power vs scattering angle on quasifree peak is a good  $m^*$  observable .

## 5.4 The Low-lying States

As mentioned in the Chapter 3, the optical model calculations of the inelastic scattering to the low-lying states depends on the elastic scattering data. The elastic scattering data obtained at both energies is not extensive enough in angle for a meaningful search of 12 optical model parameters. The previous TRIUMF elastic scattering data at 300 MeV and 500 MeV mentioned earlier were used to search the optical model parameters. Efforts were made to ensure that the optical model parameters at both energies provide a good fit to the elastic scattering cross section and analyzing power data. As a starting point for the analysis, the

initial optical potential parameters are taken from the previous search of optical model parameters. Ref. [17] at 300 MeV. The existing optical model parameters in Ref. [17] at 300-MeV do not fit analyzing power data as well as cross section data. We search on each set of data using the search routine in the computer program ECIS87 [18] and put 5 times larger  $\chi^2$ -weighting factor on analyzing power data. The resulting best fit parameters are summarized in table 6. The fits to the 300-MeV and 500-MeV elastic scattering cross sections and analyzing powers using NOPM (Non-relativistic Optical Model) are shown in Figure 46 and 47. The smooth curves in Figure 46 and 47 are NOPM calculations. Comparing the fit as shown in Figure 46 with the result from ref. [17], improvement is found in the analyzing power fit. The resulting optical model parameters listed in table 6 are slightly different than the ones in ref. [17]. There are no best fit results at 500-MeV in [17]. Using the same code ECIS87, we searched for the Dirac based optical model parameters. The real and imaginary Dirac optical model parameters of scalar ( $U_S(r)$ ) and vector ( $V_0(r)$ ) potentials in Eq.(16) are:  $U_{SR}$ ,  $R_{SR}$ ,  $a_{SR}$ ,  $W_{SI}$ ,  $R_{SI}$ ,  $a_{SI}$ ,  $U_{OR}$ ,  $R_{OR}$ ,  $a_{OR}$ ,  $W_{OI}$ ,  $R_{OI}$  and  $a_{OI}$ . Five times larger  $\chi^2$  weighting factor is placed on the analyzing power data when searching the phenomenological Dirac version of the optical model parameters. The best fit parameters from the ROPM (Relativistic Optical Model) are summarized in table 7. The fits to the 300-MeV and 500-MeV elastic scattering data using ROPM are shown in Figure 48 and Figure 49 respectively.

The fits to the elastic scattering data at both energies for the two versions of the optical models are in reasonable agreement with the data. We tried using the geometry averaging method used in ref. [17], and found the results not to be as good as the best fits. As the incident proton energy increases to 500 MeV, the real part of the optical potentials change from attractive into repulsive. The geometry averaging method might not be a suitable choice in this "critical" region.

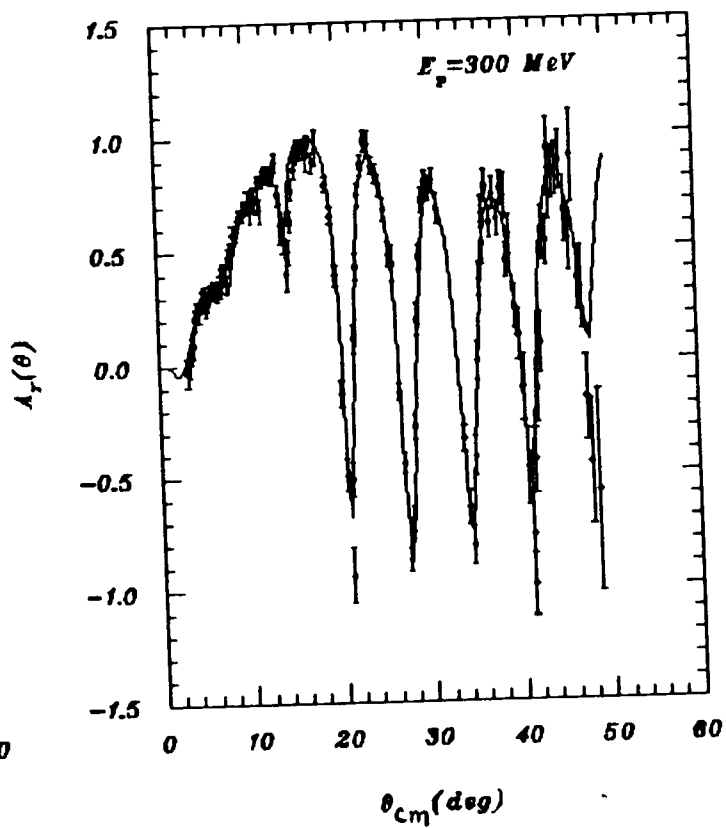
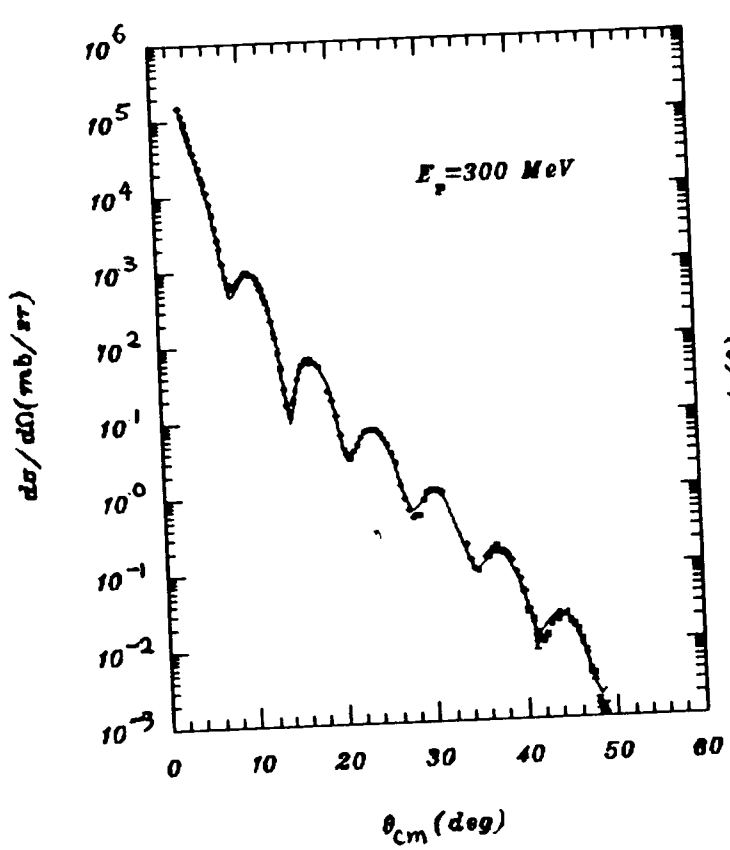
Table 5: Renormalization factor of surface response calculations to the data at 500 MeV.

$\theta_L(^{\circ})$	rnf
5	1.82
7	1.43
9	1.82
11	1.85
13	1.82
17	1.92
19	1.82
21	1.82
23	1.54
25	1.72
27	1.82

Table 6: Proton +  $^{208}\text{Pb}$  Non-relativistic Optical Model Parameters.

	300 MeV	500 MeV
$V_0(\text{MeV})$	6.238	-10.309
$R_0(\text{fm})$	1.329	1.024
$a_0(\text{fm})$	0.617	0.3809
$W(\text{MeV})$	42.534	45.583
$R_i(\text{fm})$	1.028	1.1034
$a_i(\text{fm})$	0.810	0.6348
$V_{so}(\text{MeV})$	2.182	2.0994
$R_{s1}(\text{fm})$	1.110	1.0514
$a_{s1}(\text{fm})$	0.792	0.9368
$W_{so}(\text{MeV})$	-2.866	-0.8744
$R_{s2}(\text{fm})$	0.984	1.1164
$a_{s2}(\text{fm})$	0.780	0.5596

Figure 46: Elastic Scattering Data and NOPM Calculations at 300-MeV.



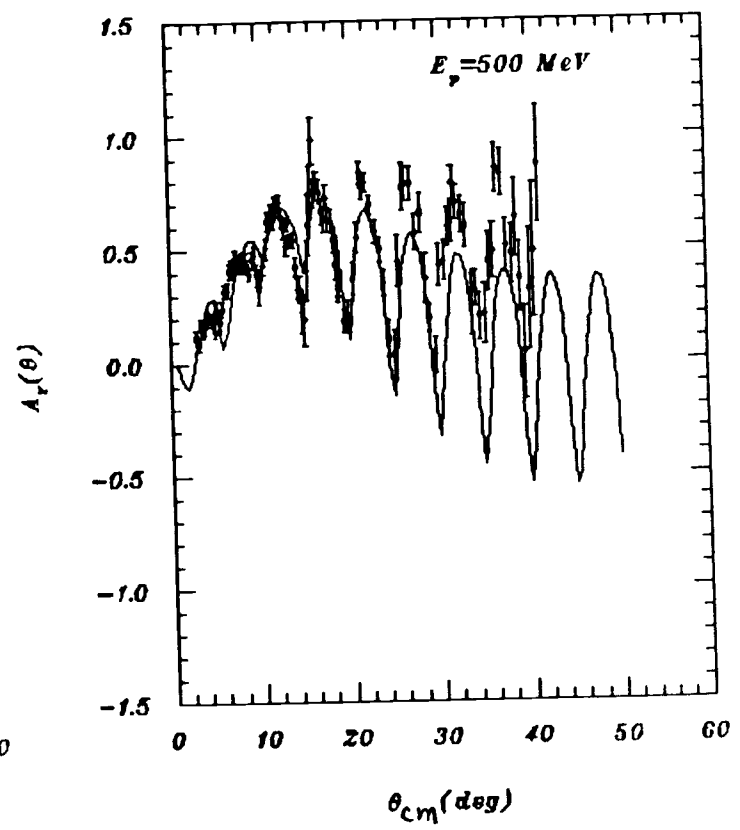
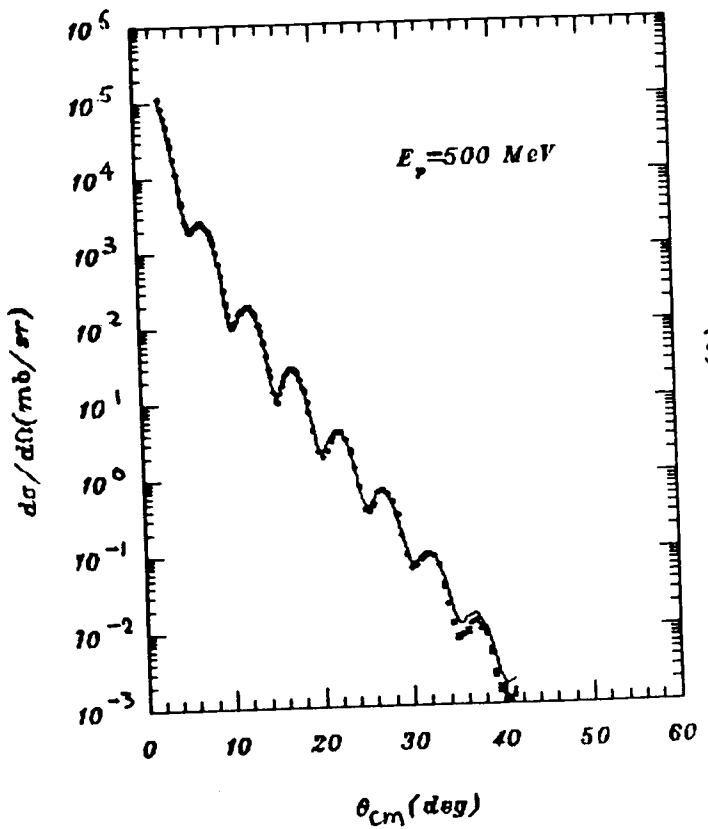


Figure 47: Elastic Scattering Data and NPM Calculations at 500-MeV.

Figure 48: Elastic scattering data and ROPM calculations of 300-MeV.

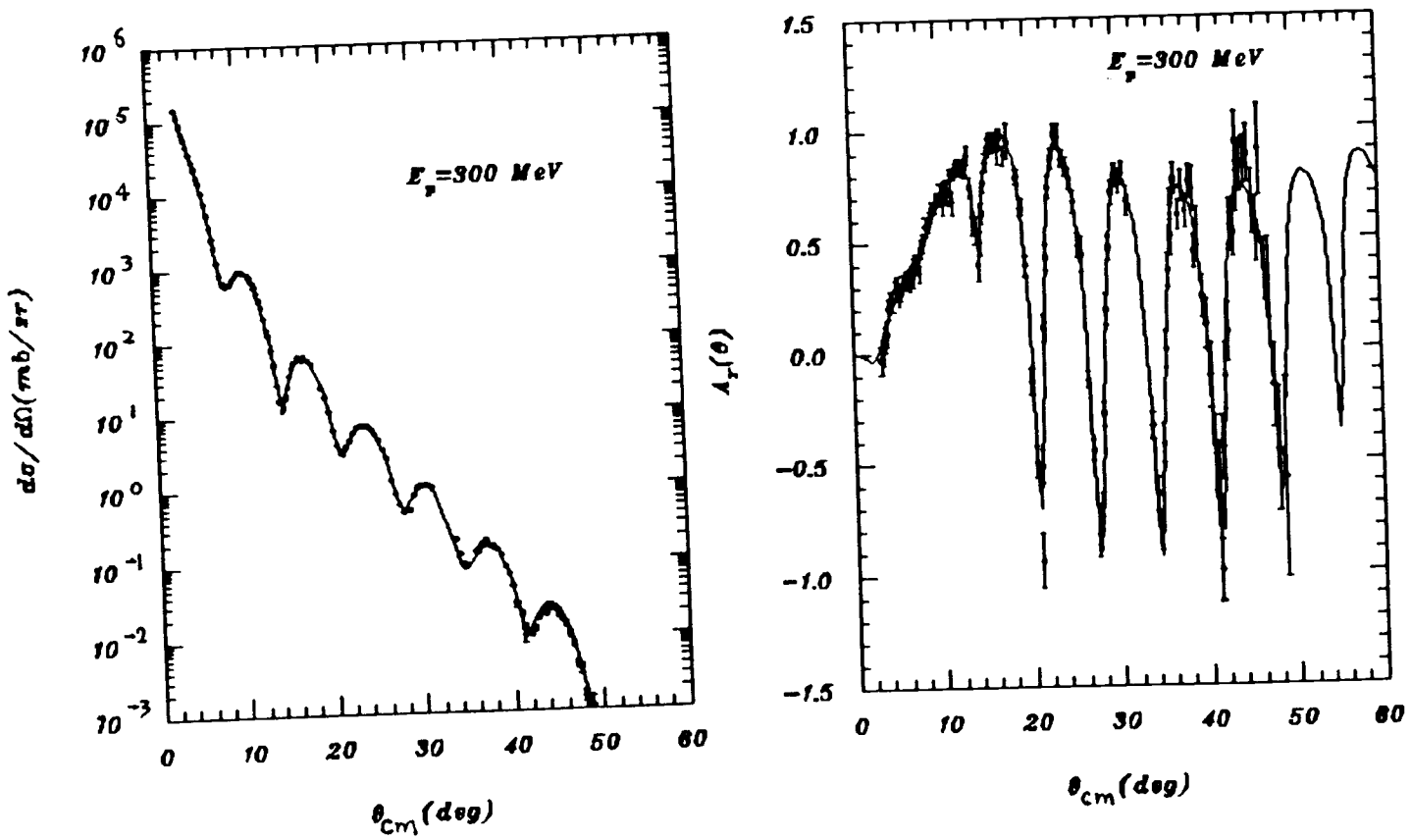
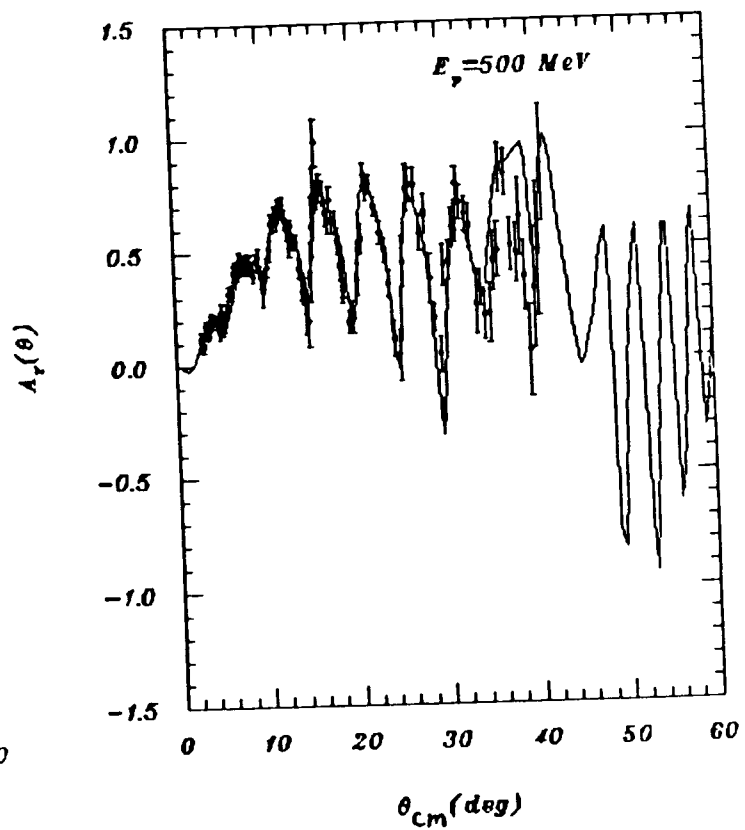
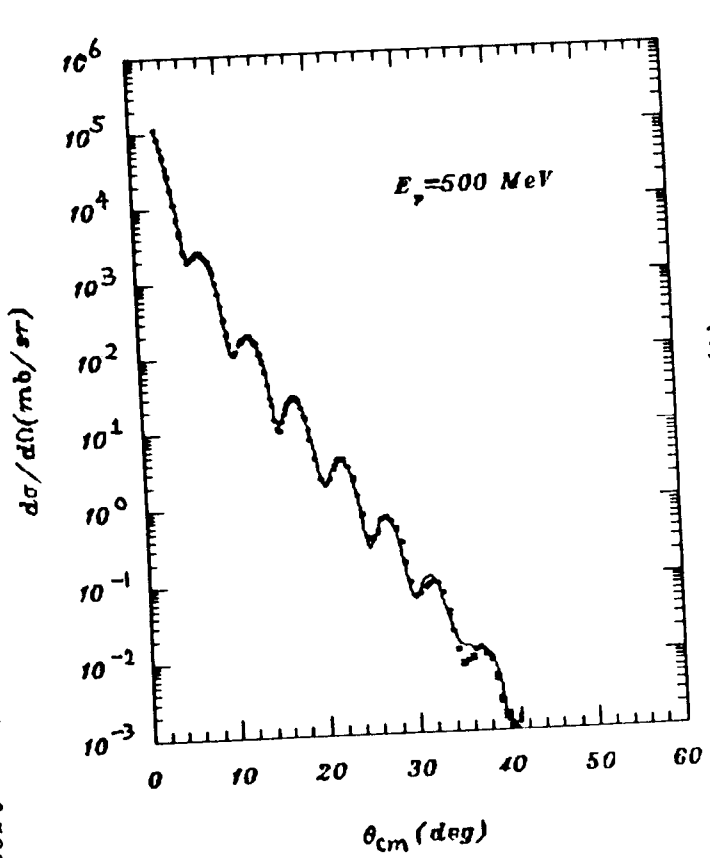




Figure 49: Elastic scattering data and ROPM calculations of 500-MeV.



Therefore, the best fit parameters were utilized.

Calculation of the inelastic scattering cross sections and analyzing powers were made using the same program ECIS87 for both versions of the optical models. For the Schrödinger based optical model, the analyses of the inelastic scattering cross sections and analyzing powers were performed using the first order vibrational model. The optical potentials are deformed according to Eq. (13) under the constraint of Eq. (14). The values of  $\beta R$  were obtained by normalizing calculated angular distribution to the measured results as indicated in Eq. (15). No adjustments were needed in the optical potentials. Using the DWBA method calculations to the low-lying states,  $3^-$  (2.614 MeV),  $5_1^-$  (3.20 MeV),  $5_2^-$  (3.71 MeV),  $2^+$  (4.09 MeV), and  $4^+$  (4.32 MeV) were made and normalized to the experimental data. A sample of these low-lying states in the form of spin up and spin down differential cross sections are shown earlier in Figure 17.

The ECIS87 Schrödinger based optical model fit to the inelastic scattering data are shown from Figure 50 to Figure 59.

The calculated cross sections and analyzing powers agree reasonably well in shape with the experimental data at both energies. The deformation lengths extracted for the  $3^-$  are found to be  $\delta_H = \beta_3 R = 0.77$  fm at both energies. Deformation lengths obtained for other states include the  $5_1^-$ ,  $\beta_{5_1} R = 0.32$  fm,  $5_2^-$ ,  $\beta_{5_2} R = 0.23$  fm,  $2^+$ ,  $\beta_2 R = 0.41$  fm and  $4^+$ ,  $\beta_4 R = 0.48$  fm. At small angles, target contamination contributions in the region of the  $5_1^-$ ,  $5_2^-$  states caused the experimental values to be higher than the DWBA expectations. The low-lying states  $2^+$  (4.09 MeV) and  $4^+$  (4.32 MeV) are decomposed from the spectrum at each angle using Gaussian functions to fit the spectrum. Since the  $2^+$  (4.09 MeV) and  $4^+$  (4.32 MeV) states are not fully resolved, the results for these states contain some additional uncertainty (See Figure 31).

The analyses of 290-MeV and 500-MeV inelastic scattering cross sections and

Figure 50:  $3^-$  (2.61 MeV) data and NOPM calculations, at  $E_p = 290$  MEV

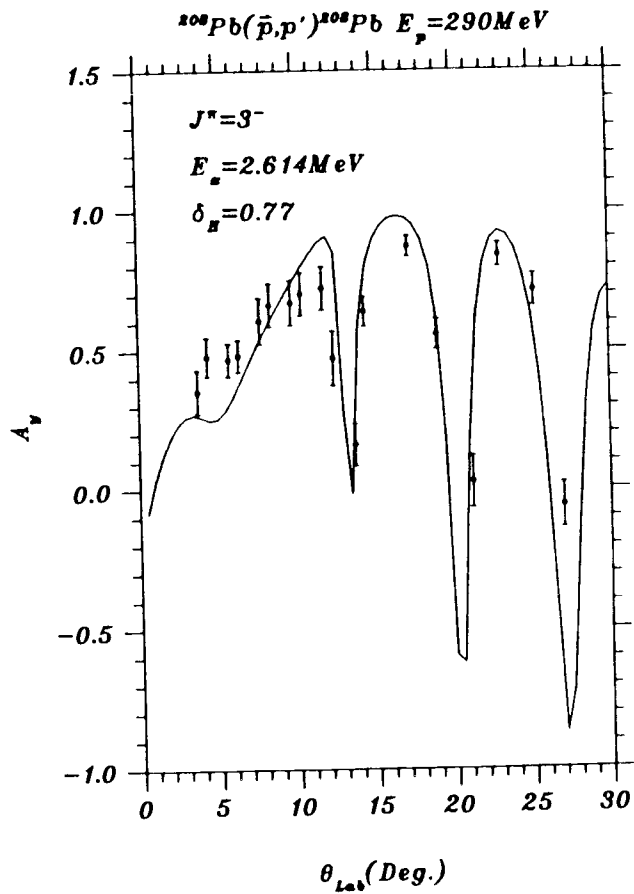
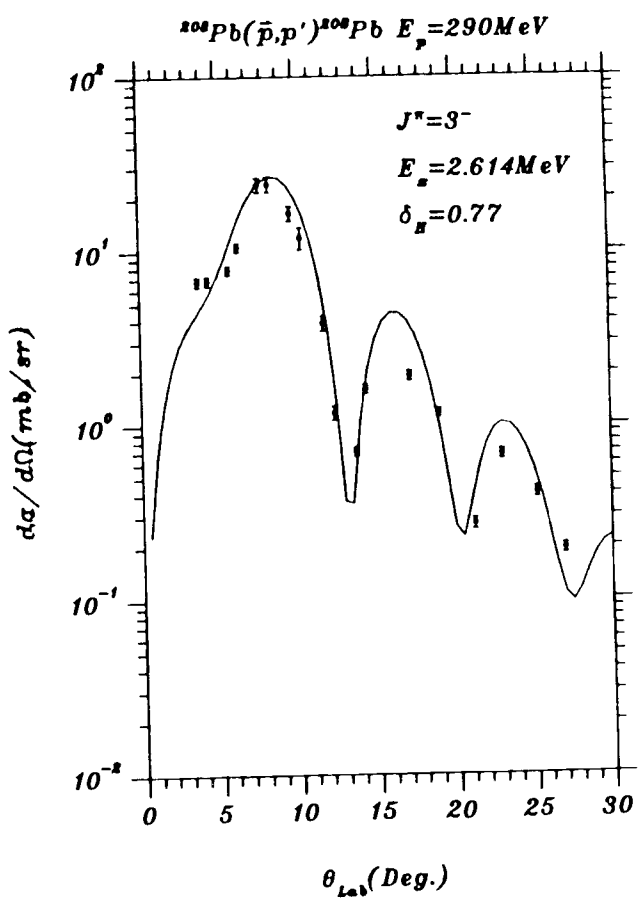


Figure 51:  $5_1^-$  (3.20 MeV) data and NOPM calculations, at  $E_p=290$  MeV

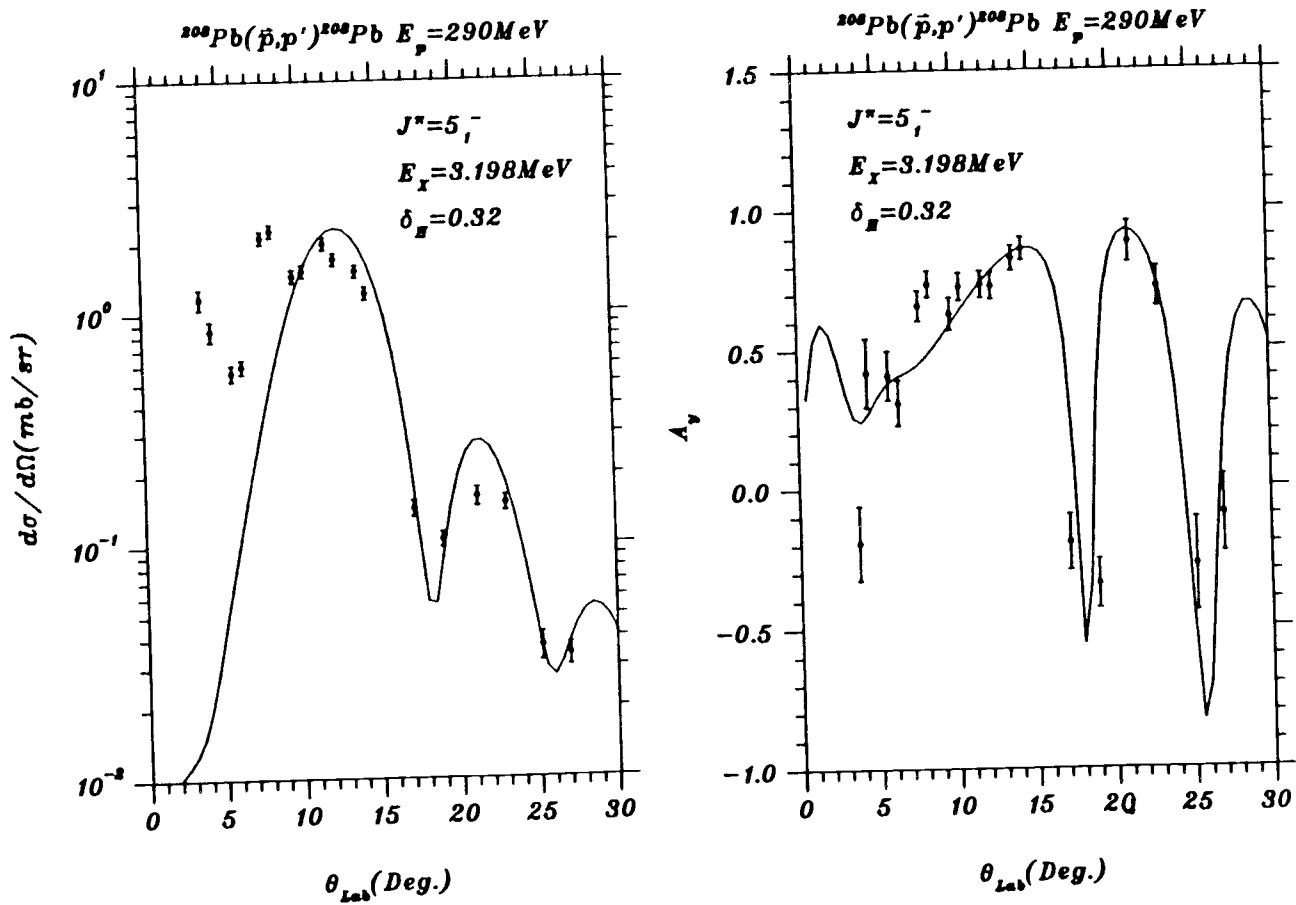
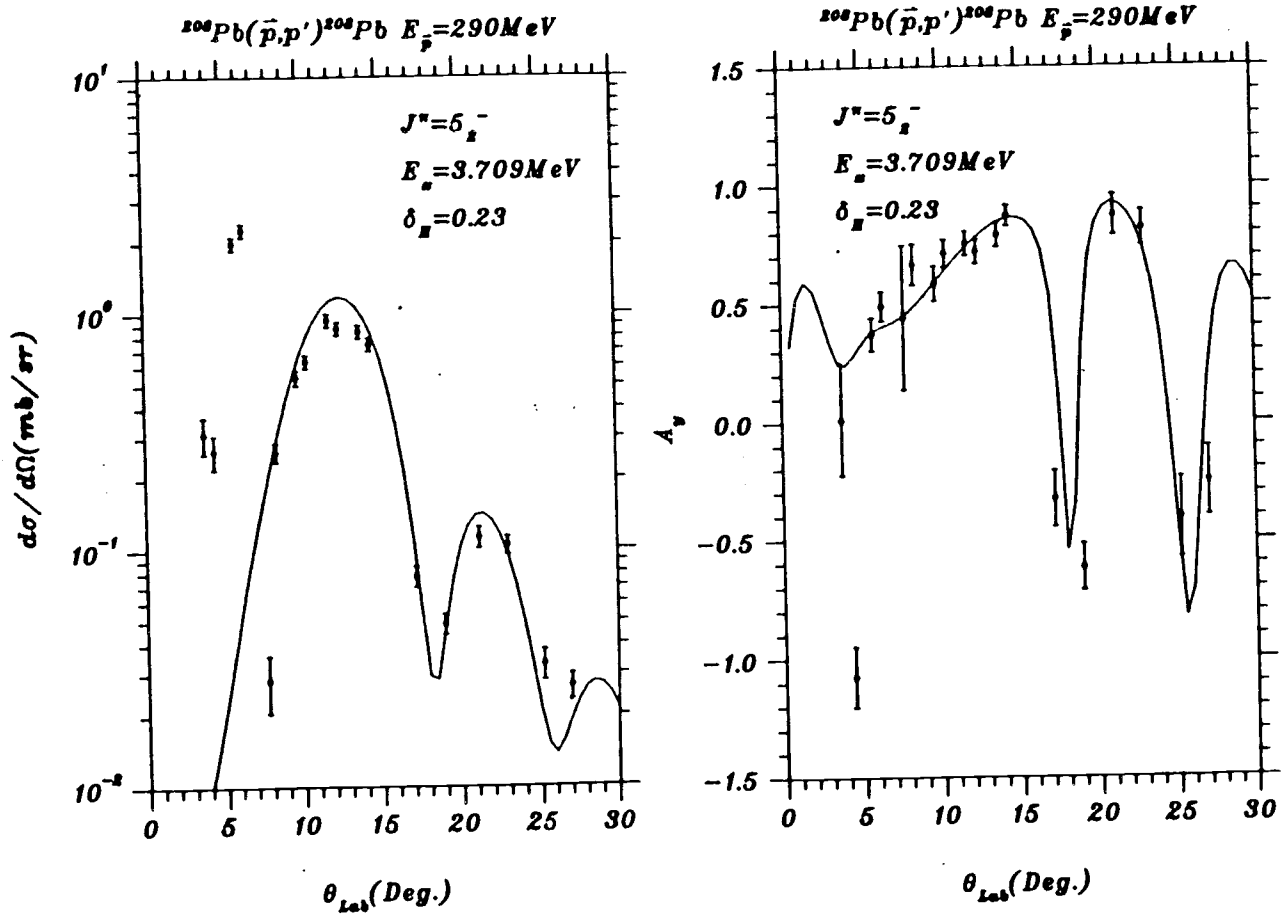


Figure 52:  $5_2^-$  (3.71 MeV) data and NOPM calculations, at  $E_p=290$  MeV



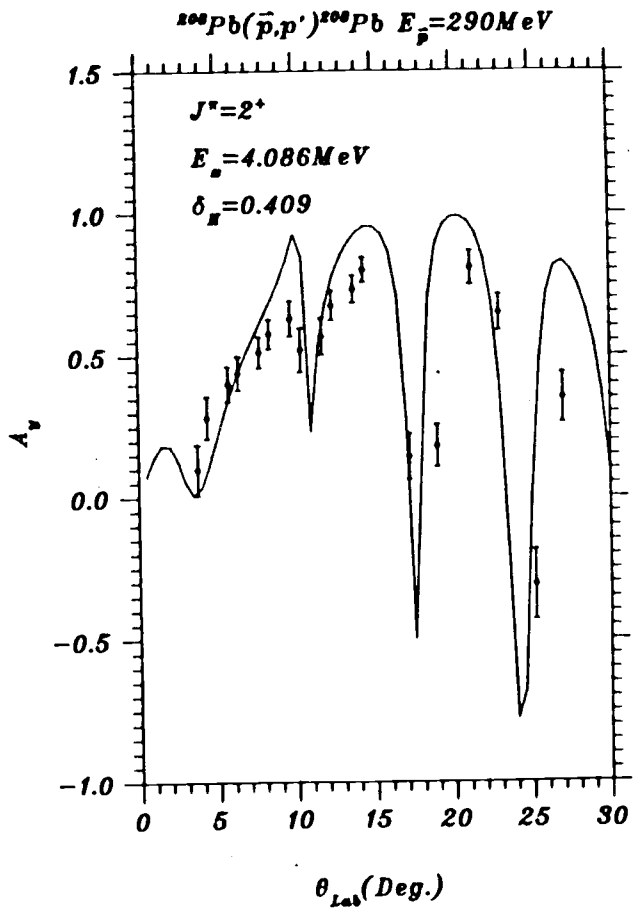
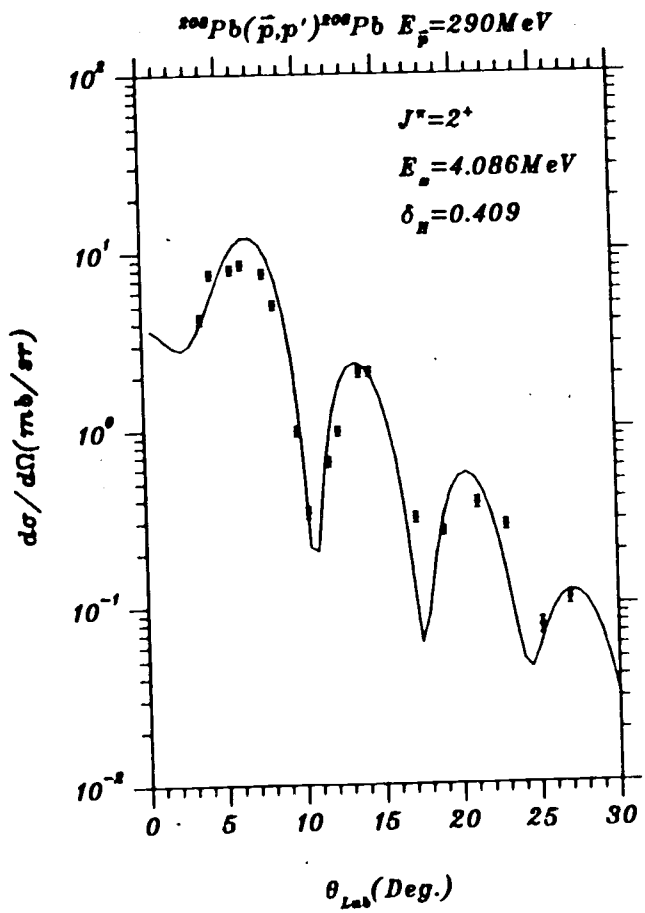


Figure 53:  $2^+$  (4.09 MeV) data and NOPM calculations, at  $E_p=290$  MeV

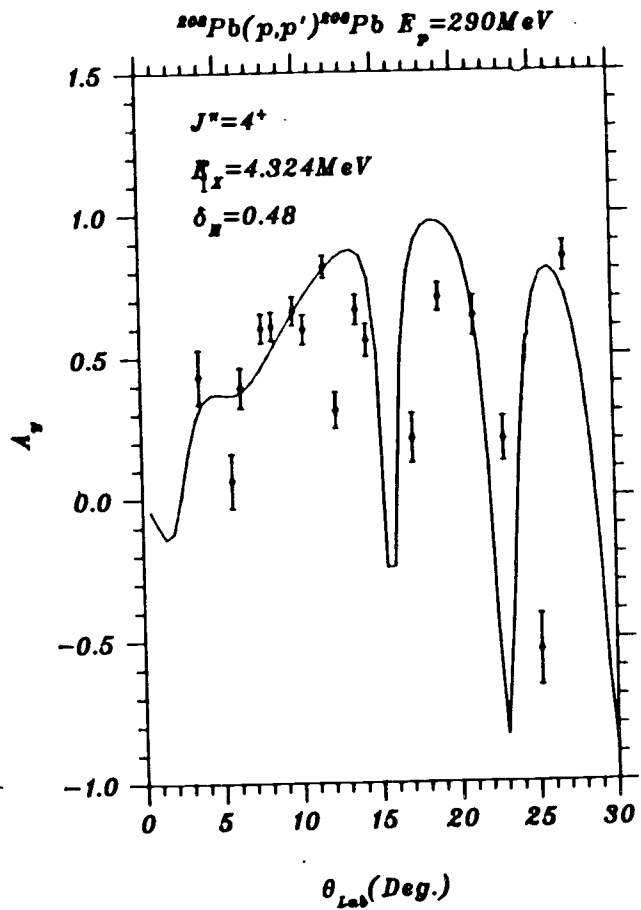
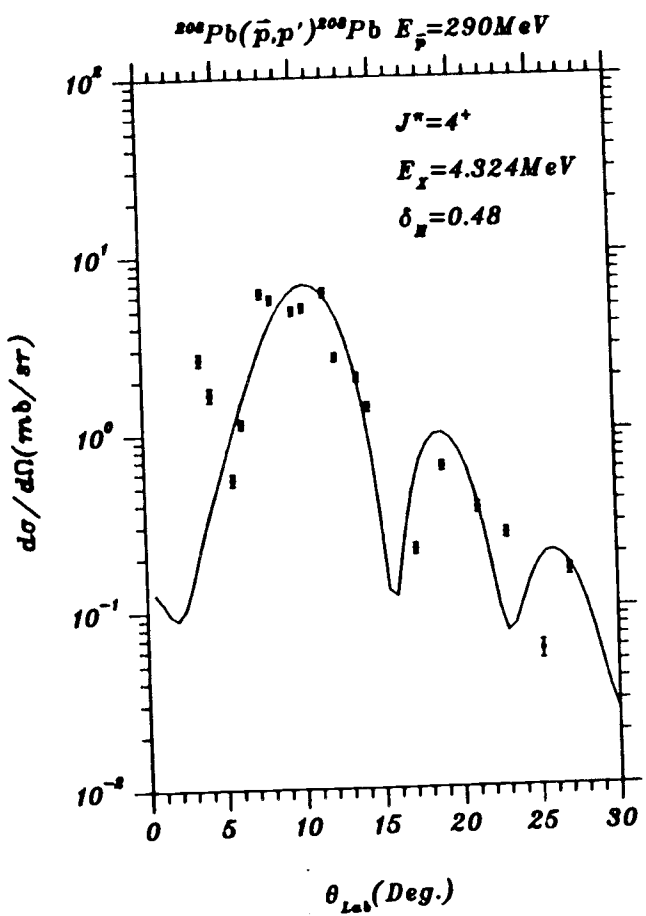


Figure 54:  $4^+$  (4.32 MeV) data and NOPM calculations, at  $E_p=290$  MeV

Figure 55:  $3^-$  (2.61 MeV) data and NOPM calculations, at  $E_p=500$  MeV

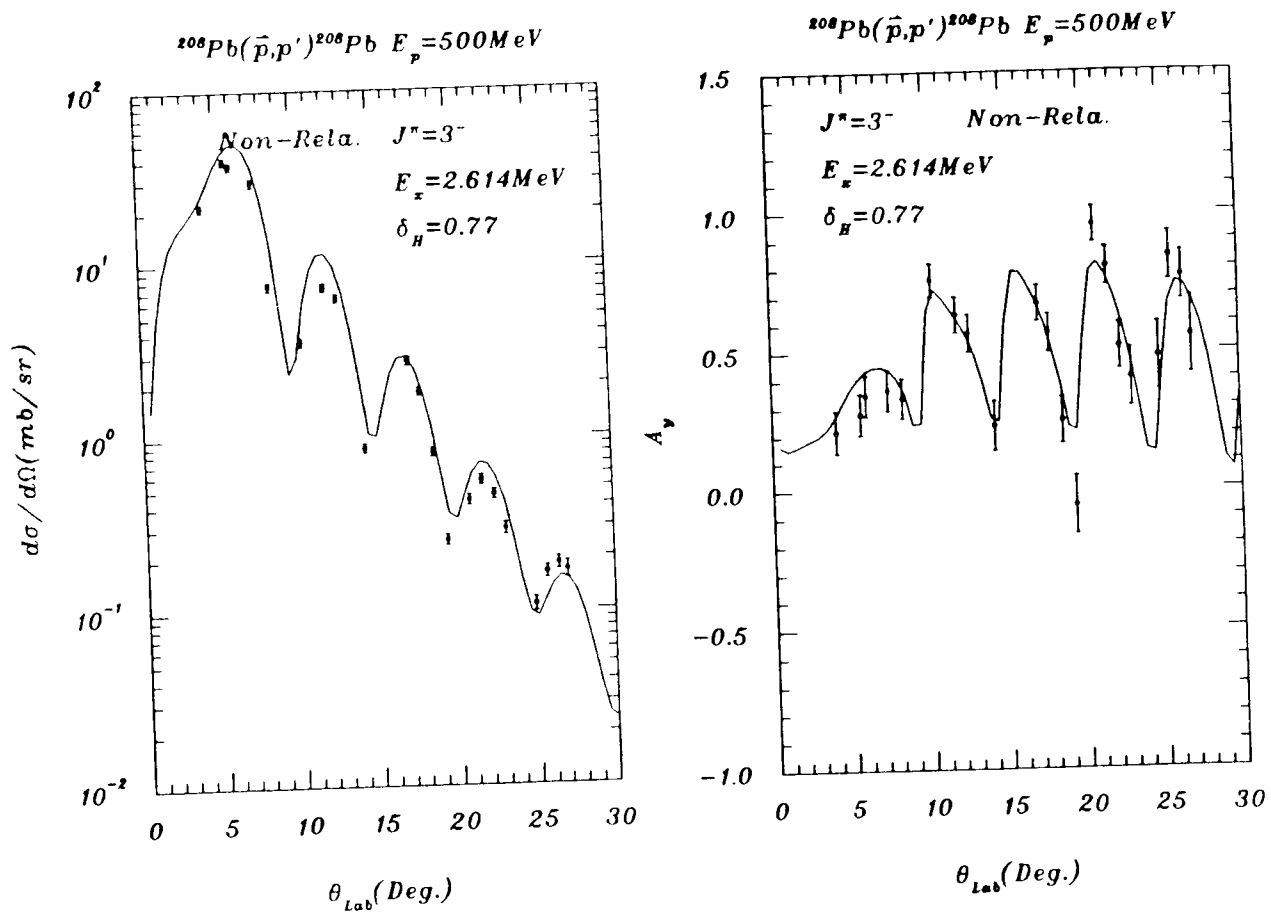




Figure 56:  $5_1^-$  (3.20 MeV) data and NOPM calculations, at  $E_p=500$  MeV

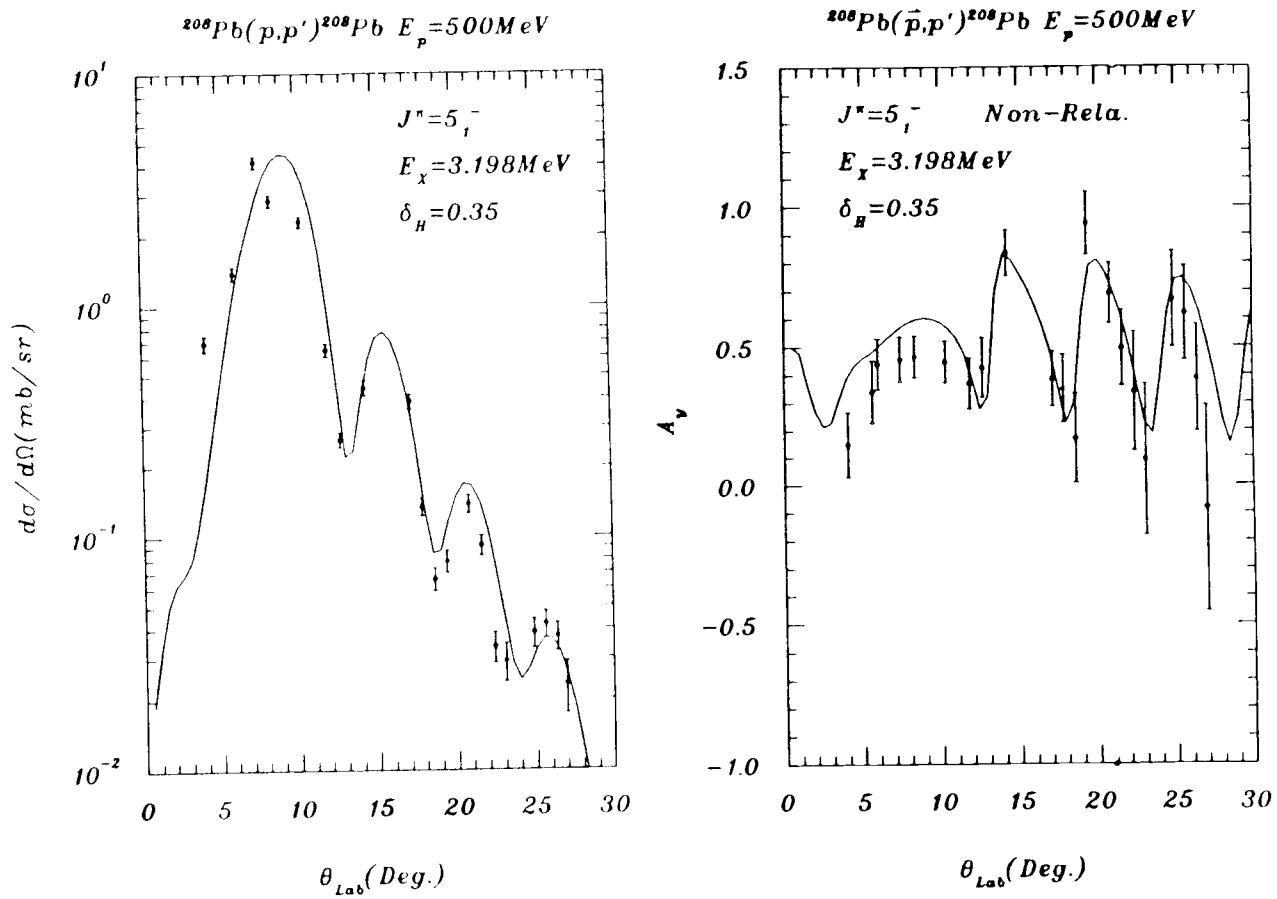


Figure 57:  $5_2^-$  (3.71 MeV) data and NOPM calculations, at  $E_p=500$  MeV

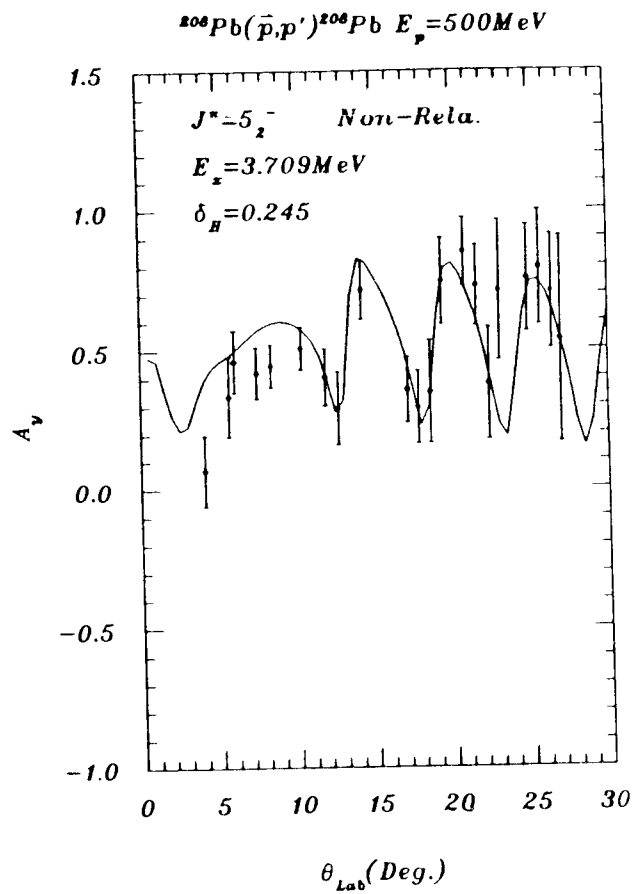
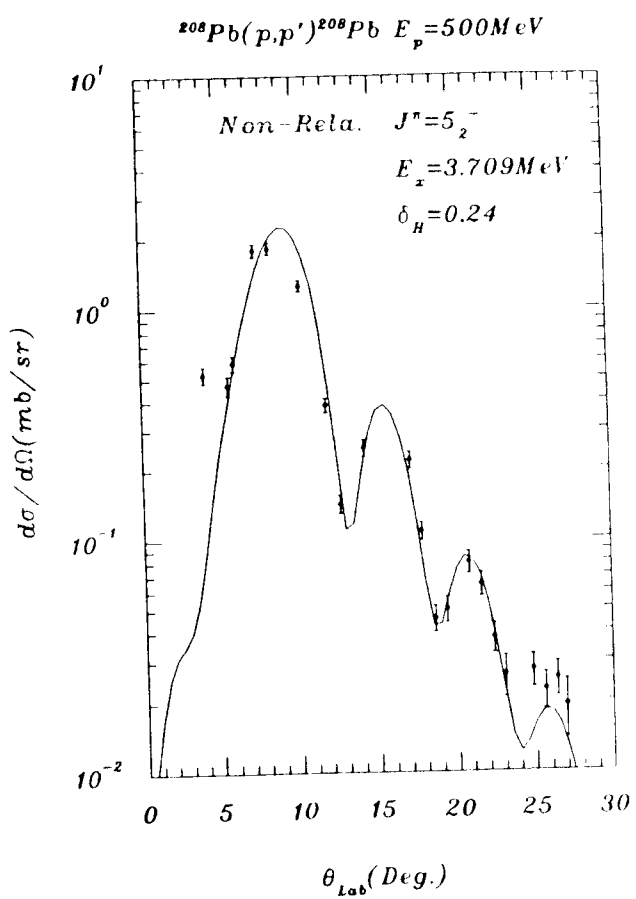


Figure 58:  $2^+$  (4.09 MeV) data and NOPM calculations, at  $E_p=500$  MeV

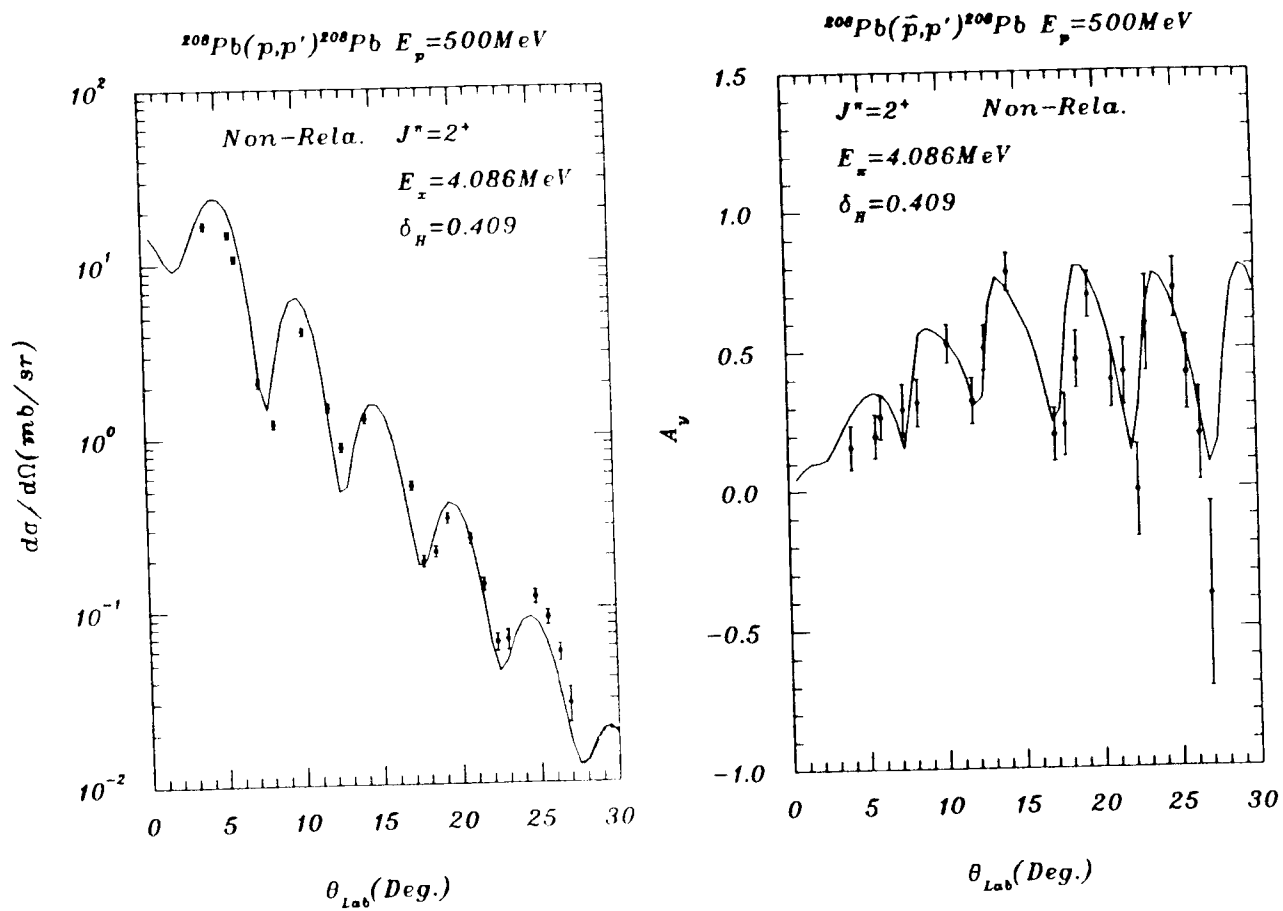
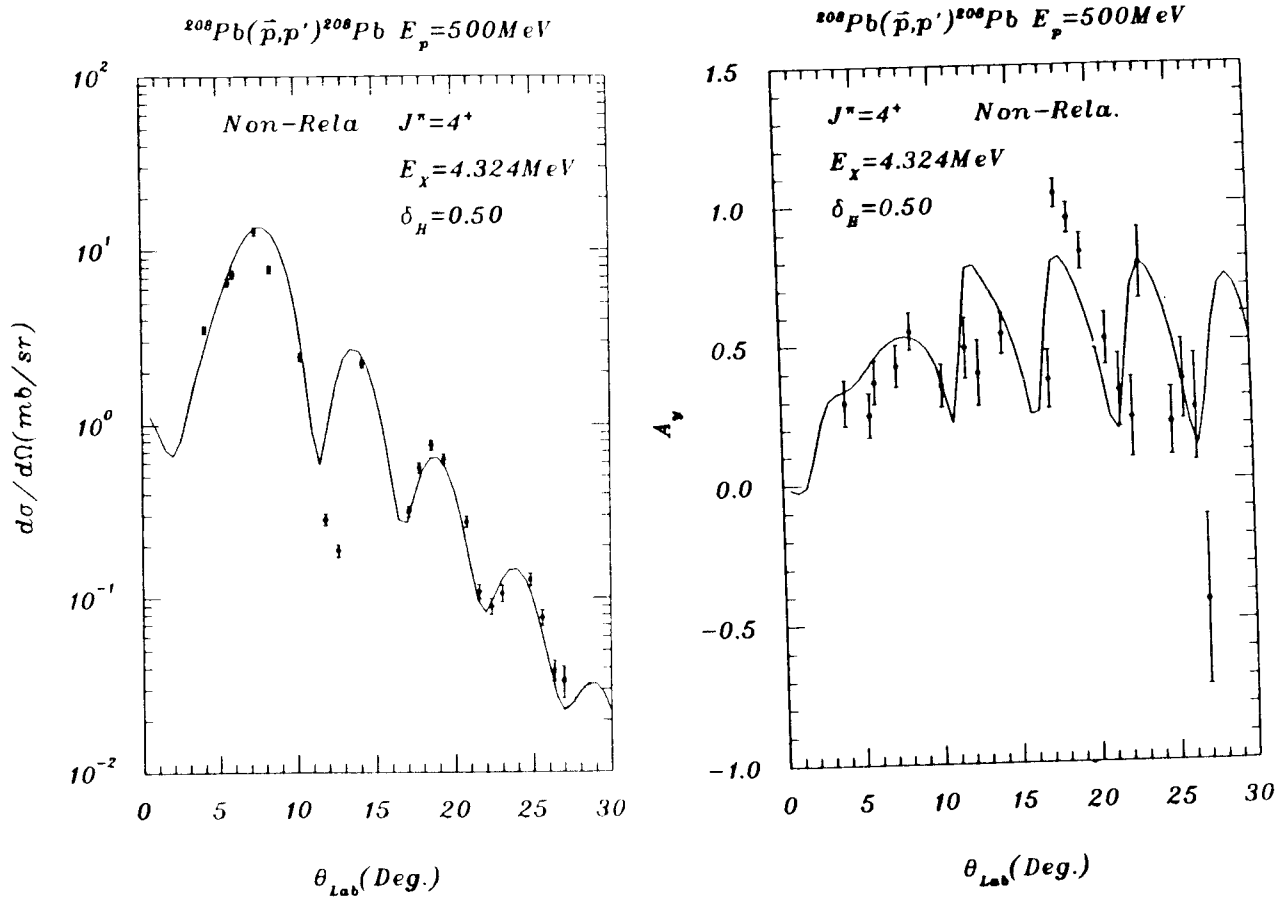


Figure 59:  $4^+$  (4.32 MeV) data and NOPM calculations, at  $E_p=500$  MeV



analyzing powers were also undertaken using a Dirac based optical model. Also using the first order vibrational model, inelastic scattering to the low-lying states  $3^-$ ,  $5_1^-$ ,  $5_2^-$ ,  $2^+$  and  $4^+$  were calculated and renormalized to our experimental data without any further optical potential parameter adjustments at both energies. At  $E_p = 290$  MeV, the Dirac optical model DWBA calculations agree in shape, with the experimental cross sections, almost as well as the Schrödinger based optical model calculations. The analyzing powers so calculated reproduce the experimental data better than the Schrödinger calculations. The deformation lengths of all states extracted from the Dirac based calculations are essentially the same in as for the Schrödinger case. Fits of 290-MeV ROPM (Relativistic Optical Model ) calculations to states  $3^-$  (2.61 MeV),  $5_1^-$  (3.20 MeV),  $5_2^-$  (3.71 MeV),  $2^+$  (4.09 MeV) and  $4^+$  (4.32 MeV) are shown in Figure 60 to 64.

At 500 MeV, the Dirac optical model DWBA calculations also reproduce the major features of the  $A_y(\theta)$  and  $d\sigma/d\Omega(\theta)$  experimental data. At large angles, however, there are some discrepancies. Possible explanations of the discrepancies may be the following: firstly, the DWBA approach to the low-lying states in the Dirac frame is simplification; secondly, the 12 parameters obtained from elastic scattering data under the Dirac frame are not sufficiently well determined; thirdly, the phenomenological Dirac approach using only scalar and vector potentials might be too simple. The 500-MeV low-lying state data and ROPM (Relativistic Optical Model) calculations are shown in Figure 65 to 69. Over all the deformation lengths obtained are the same as the ROPM results from the 290-MeV data.

## 5.5 Conclusion

Inclusive polarized proton scattering on a  $^{208}\text{Pb}$  target were performed at  $E_p = 290$  MeV and 500 MeV for scattering angle  $\theta = 4^\circ$  to  $27^\circ$ . The energy loss

Figure 60:  $3^-$  (2.61 MeV) data and ROPM calculations, at  $E_p = 290$  MeV

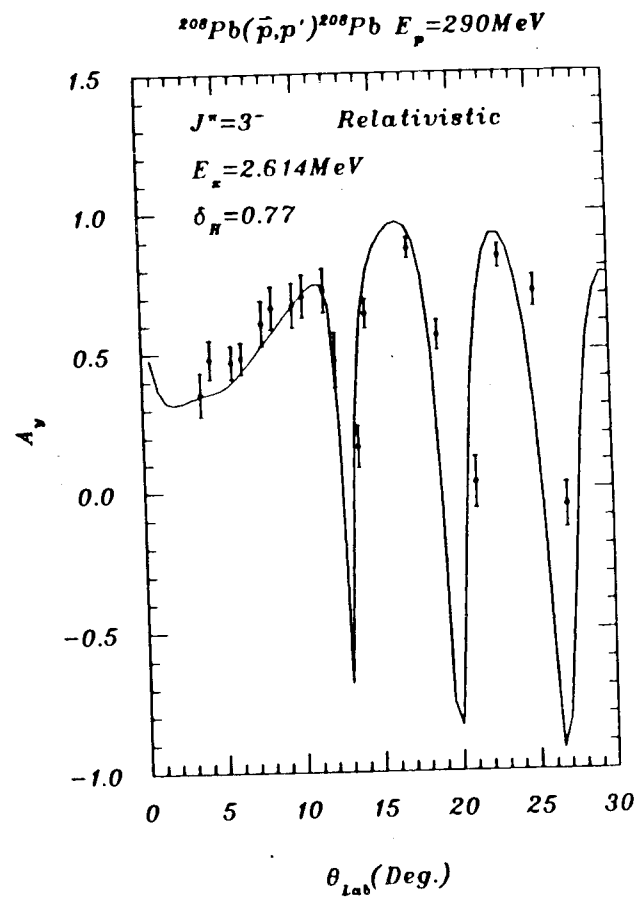
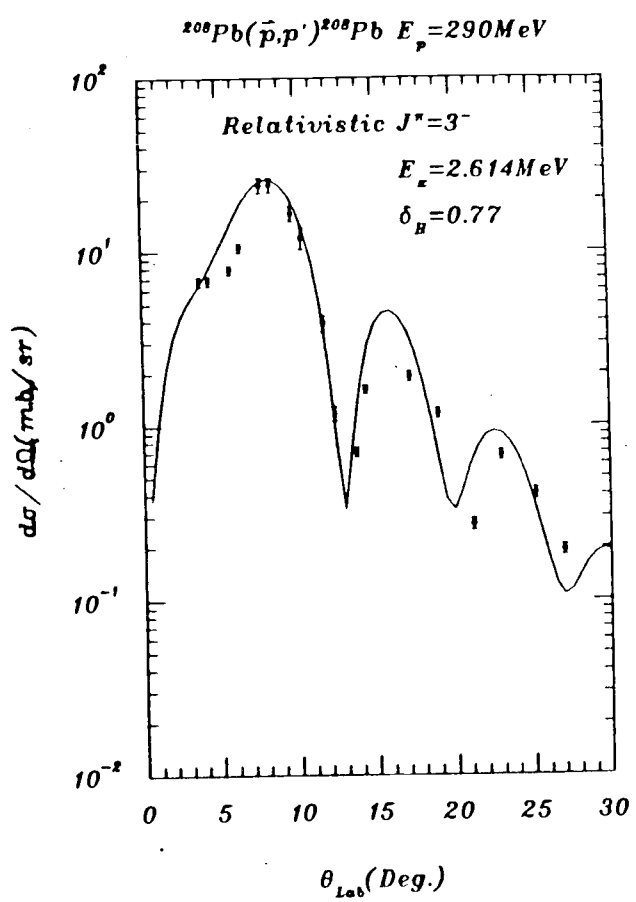


Figure 61:  $5_1^-$  (3.20 MeV) data and ROPM calculations, at  $E_p = 290$  MeV

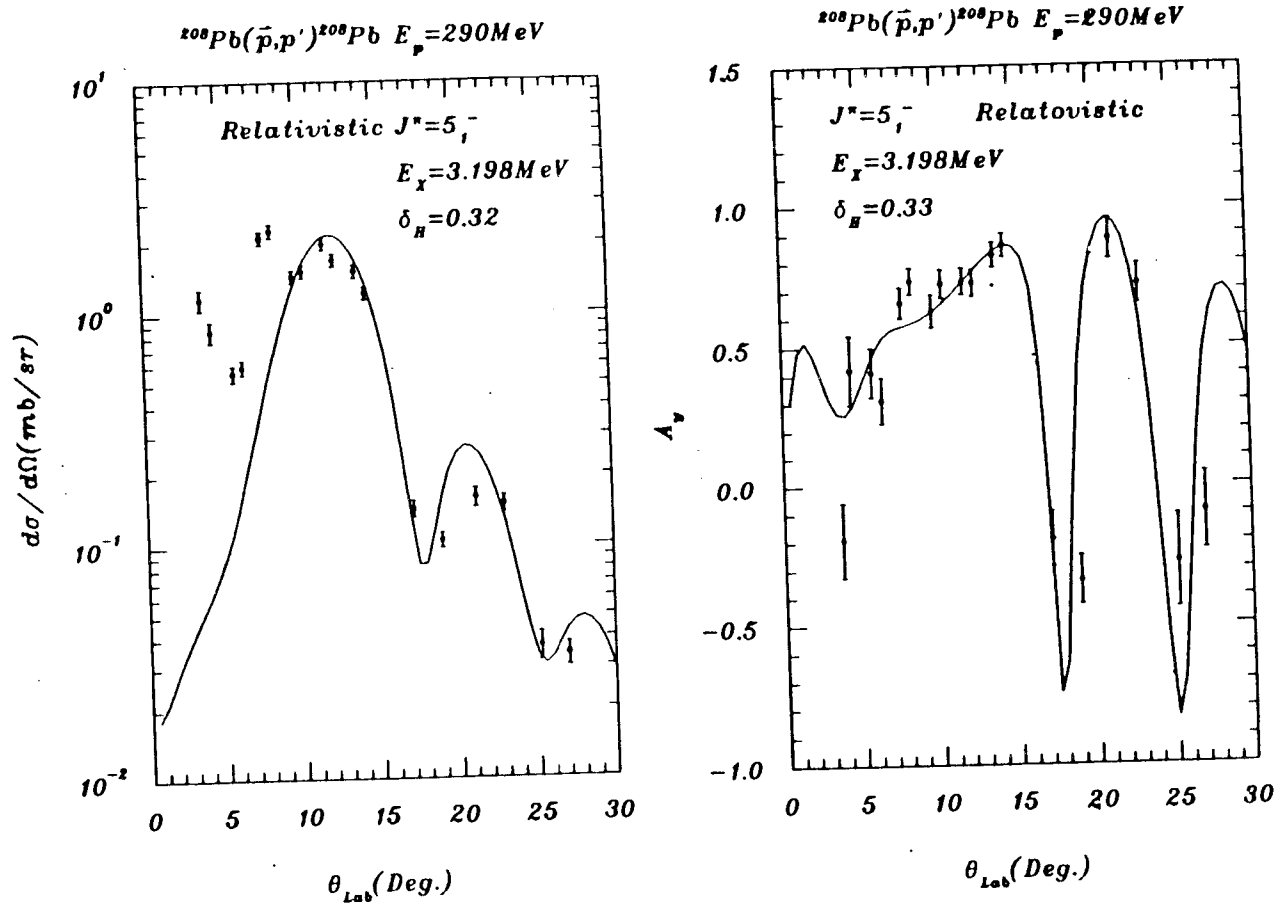
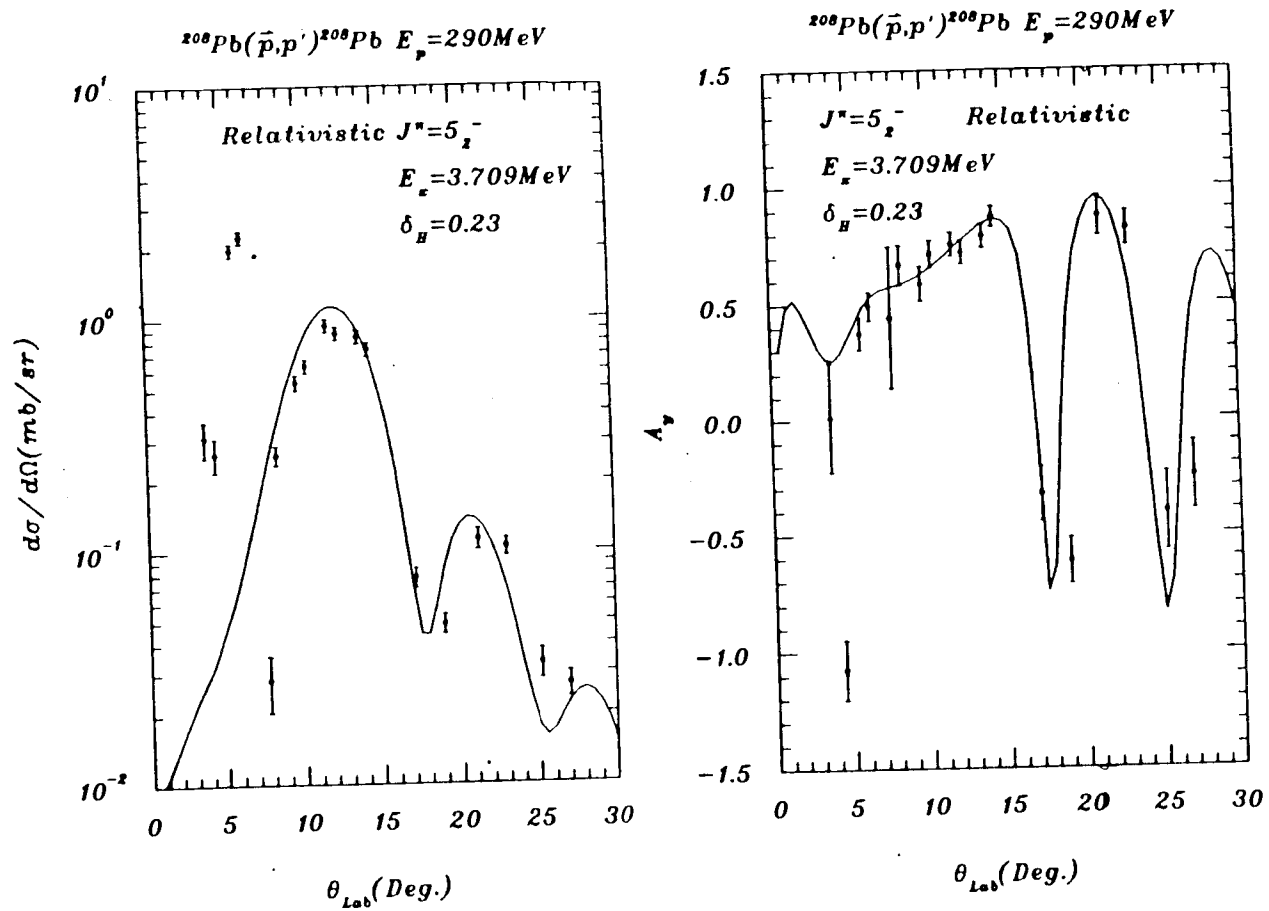


Figure 62:  $5_2^-$  (3.71 MeV) data and ROPM calculations. at  $E_p = 290$  MeV





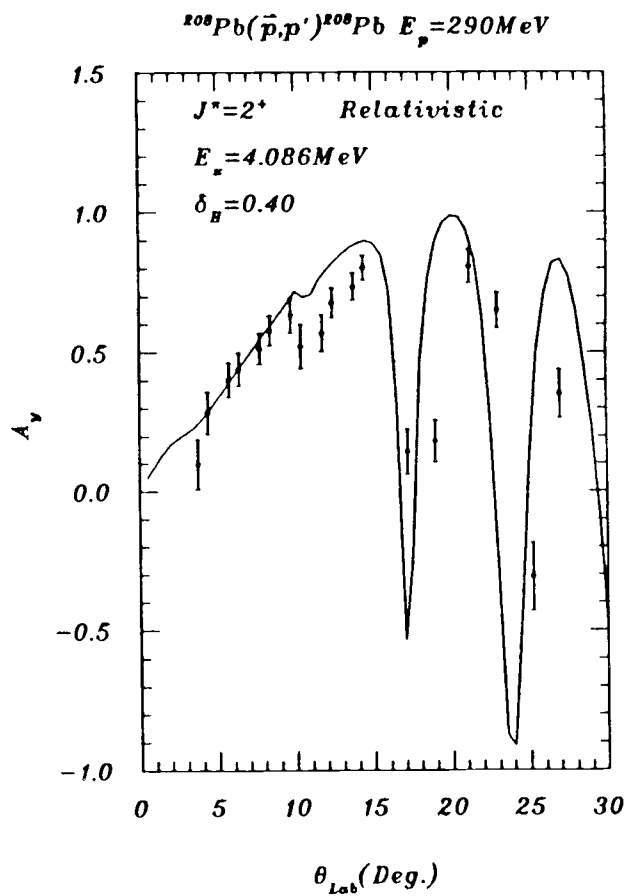
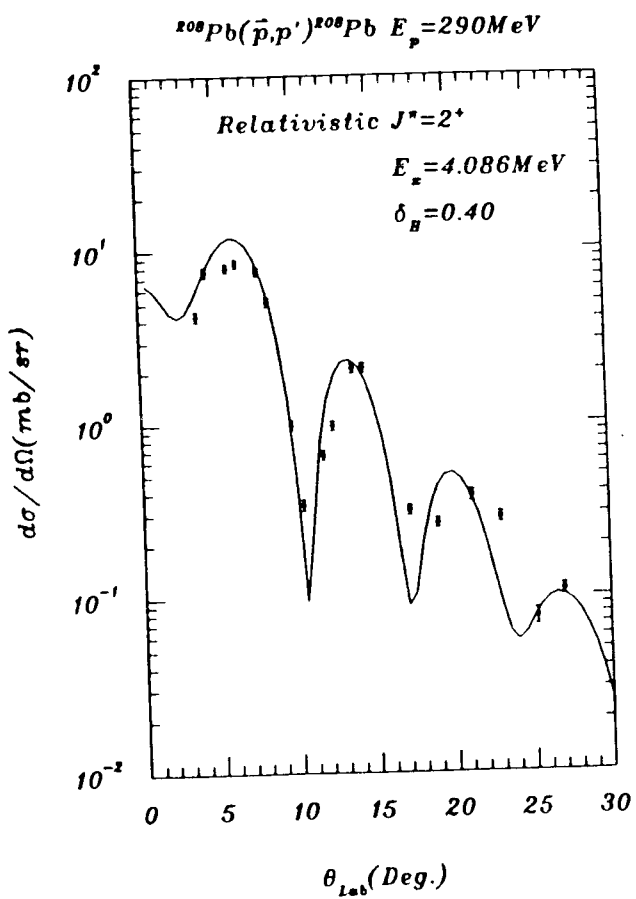


Figure 63:  $2^+$  (4.09 MeV) data and ROPM calculations, at  $E_p=290$  MEV

Figure 64:  $4^+$  (4.32 MeV) data and ROPM calculations, at  $E_p = 290$  MEV

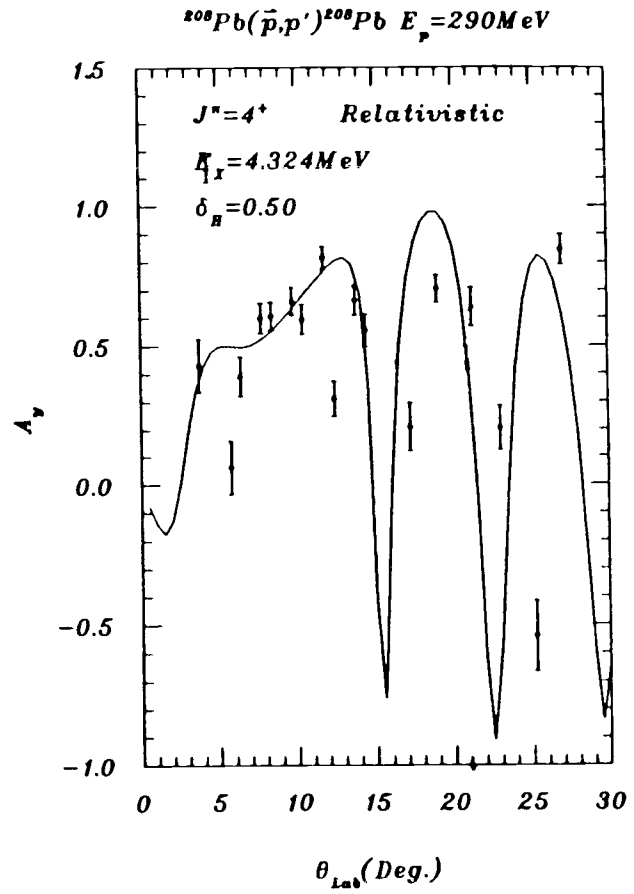
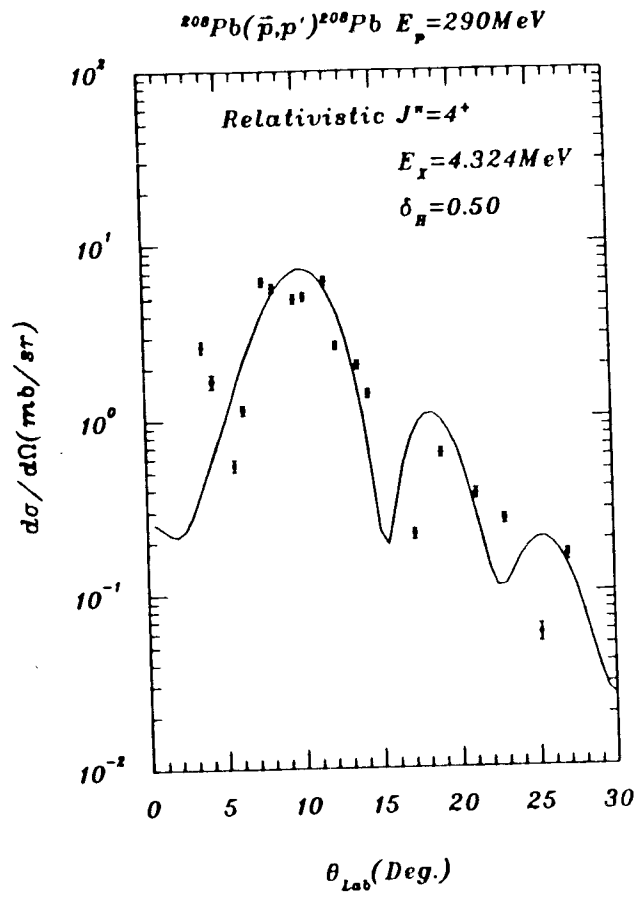


Figure 65:  $3^-$  (2.61 MeV) data and ROPM calculations, at  $E_p = 500$  MeV

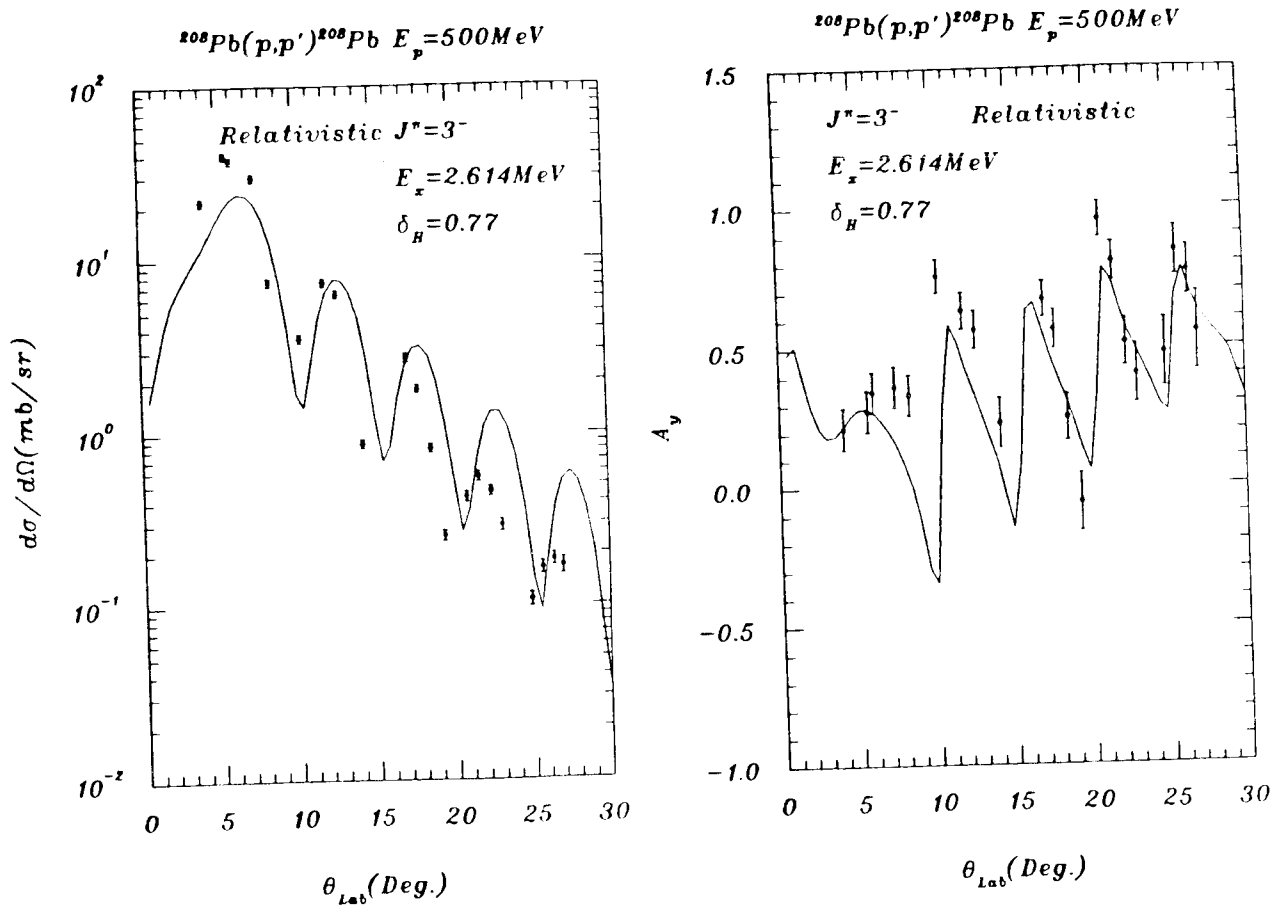


Figure 66:  $\delta_1^-$  (3.20 MeV) data and ROPM calculations, at  $E_p = 500$  MeV

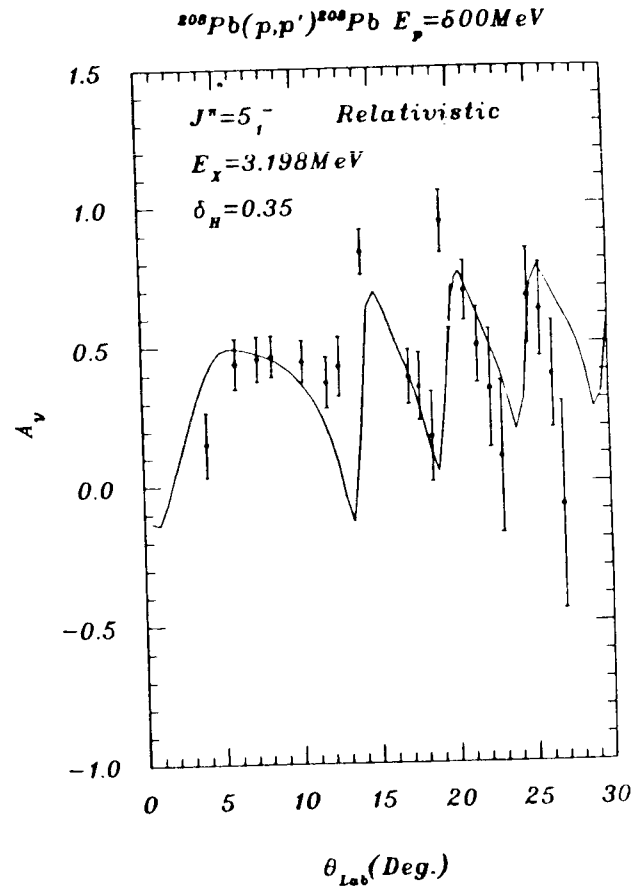
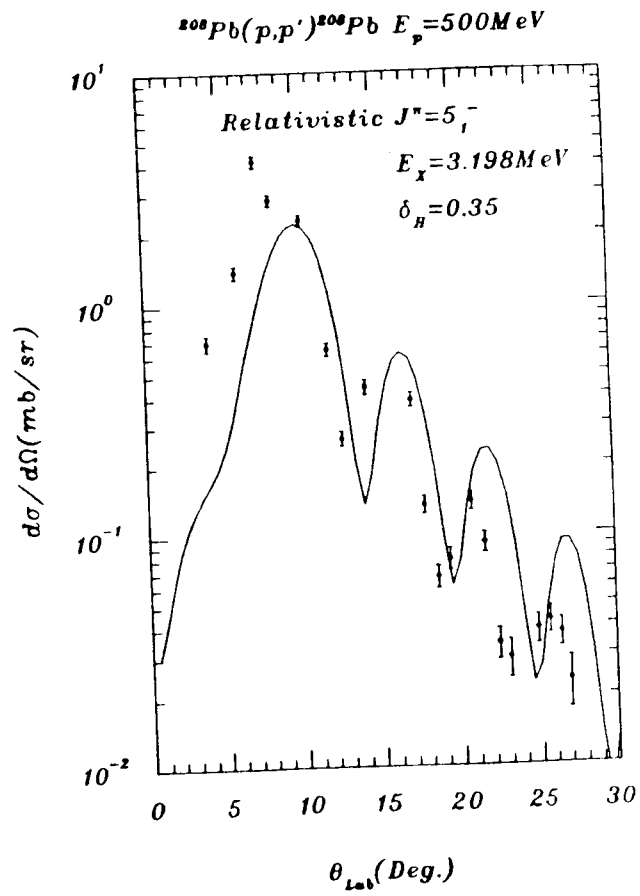


Figure 67:  $5_2^-$  (3.71 MeV) data and ROPM calculations, at  $E_p = 500$  MeV

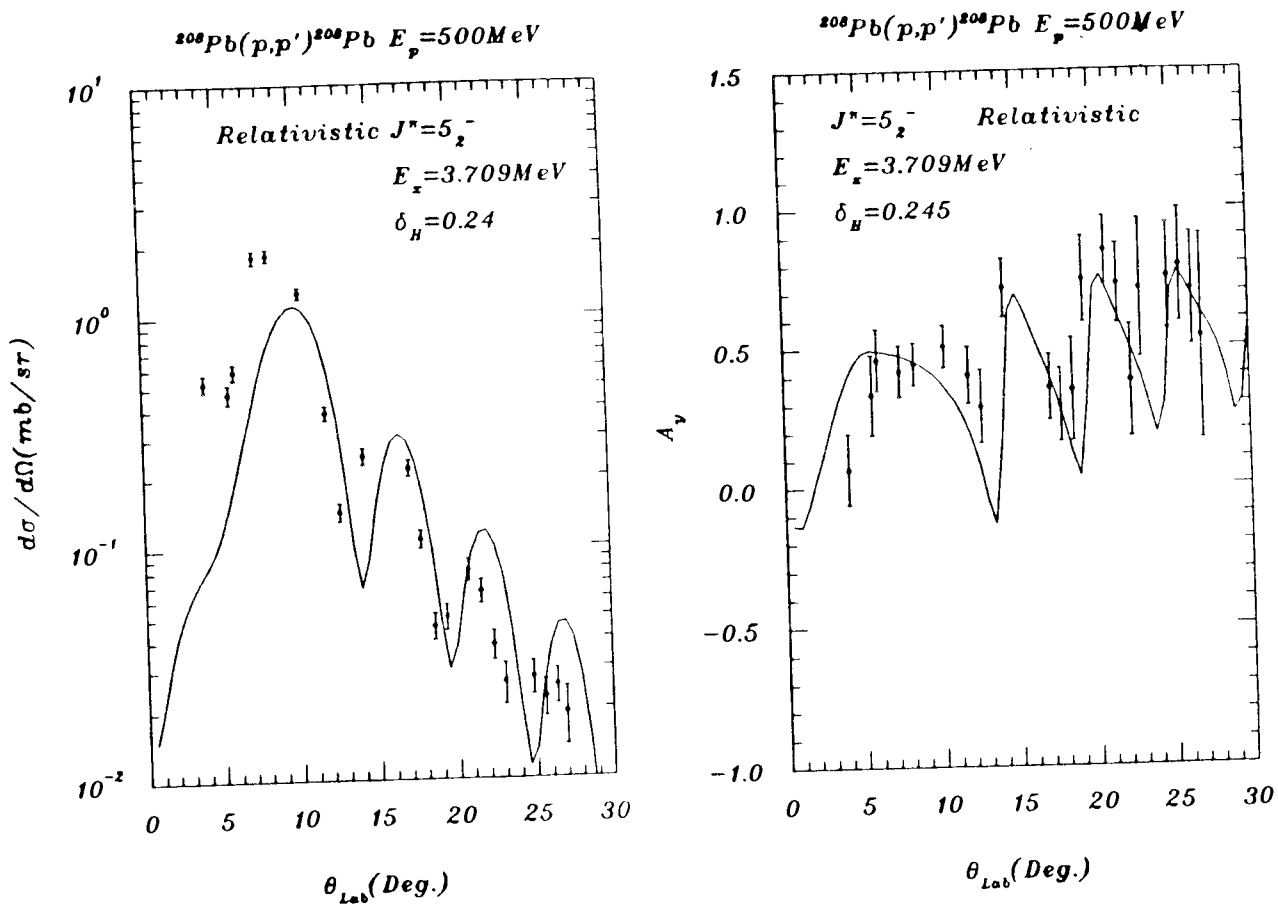


Figure 68:  $2^+$  (4.09 MeV) data and ROPM calculations, at  $E_p = 500$  MeV

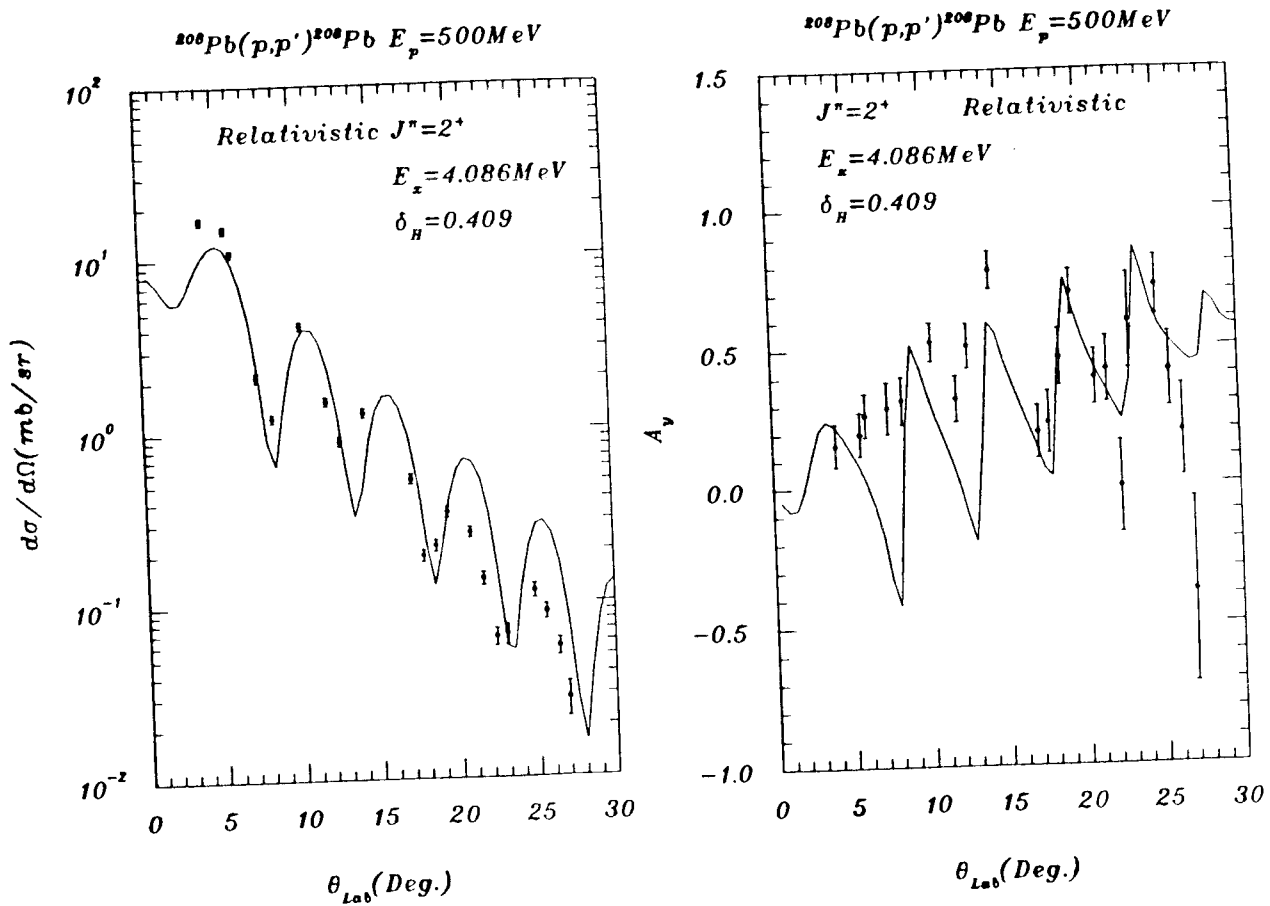
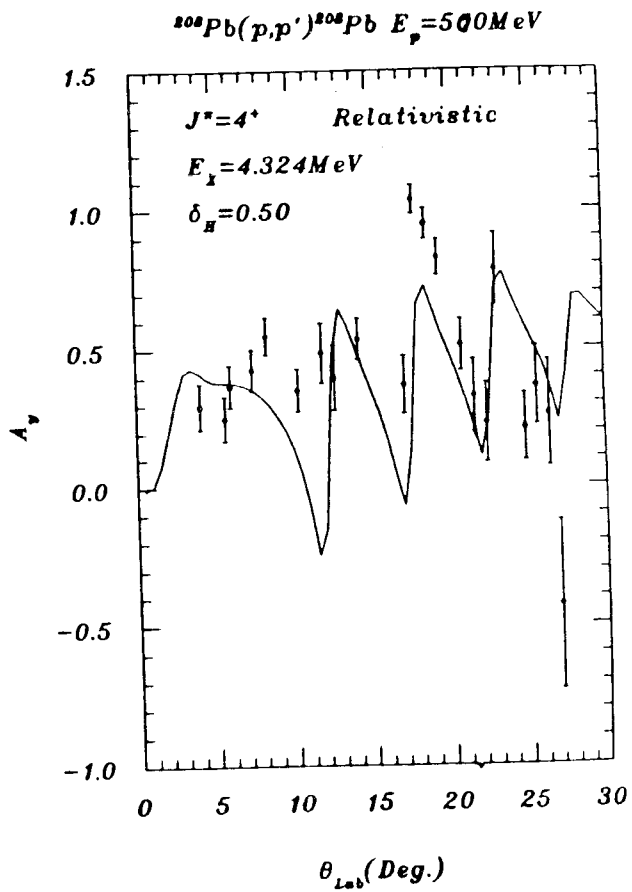
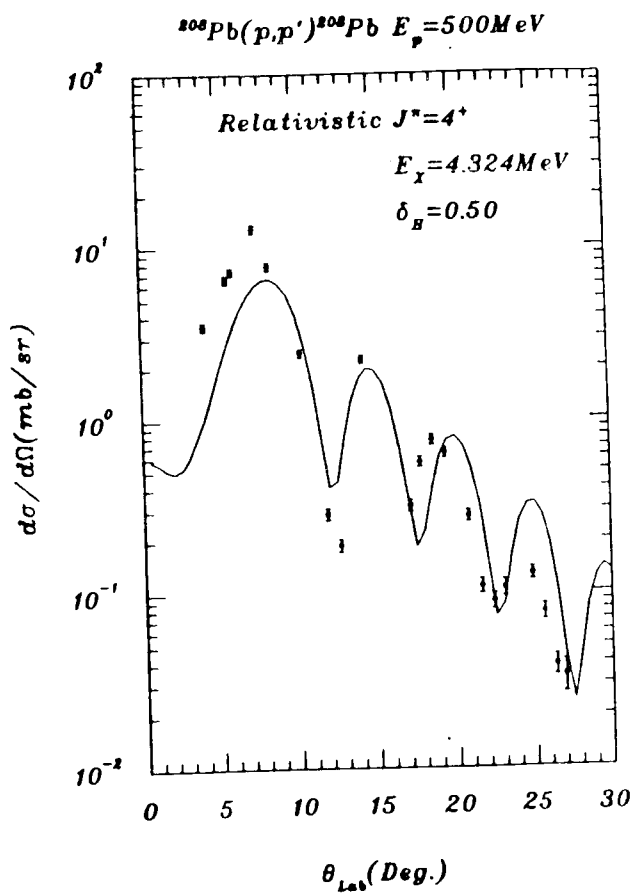


Figure 69:  $4^+$  (4.32 MeV) data and ROPM calculations, at  $E_p = 500$  MeV



covered the range 0 to 250 MeV. Double differential cross sections ( $d^2\sigma/d\Omega dE$ ) and analyzing powers ( $A_y$ ) vs excitation energy were obtained at each angle at both energies; Analyzing power angular distributions for the quasifree peaks at both energies were also formed. These results were compared with theoretical model calculations. Inelastic scattering to the low-lying states,  $3^-$  (2.61 MeV),  $5_1^-$  (3.20 MeV),  $5_2^-$  (3.71 MeV),  $2^+$  (4.09 MeV),  $4^+$  (4.32 MeV), were extracted from inclusive proton scattering spectra at both energies. The cross section and analyzing power angular distributions were compared with the optical model calculations.

The continuum peak kinematics follow the free NN scattering behavior closely, and the continuum cross section spectra can be well described in shape by free surface response model calculations. The continuum spectra at both energies were dominated by single-step scattering. Only at high excitation energies, do multiple scattering contributions start to become important. These results support the view that the impulse approximation is a suitable way to describe inclusive proton scattering to the continuum region for intermediate energy nuclear physics. Additional theoretical refinements of nuclear medium effects should be included to accurately describe the magnitude of cross section spectrum.

Analyzing powers, which involve ratios of cross sections, greatly reduce some of the complicated nuclear medium effects on the cross section spectrum. The analyzing power plotted as a function of excitation energy may exhibit many features including the response of the target medium to the spin states of the incident proton beam, multiple scattering in the high energy transfer region and the nuclear structure in the low energy transfer region. The analyzing power for quasifree scattering minimizes possible nuclear medium contributions and the multiple scattering contributions. Analyzing power angular distributions at quasifree peaks at both incident proton energies studied were compared with the free NN values as



well as values calculated in the nuclear medium. Perhaps the most interesting result is that the experimental results strongly indicate the dominance of single-step quasifree scattering and the presence of relativistic medium effects characterized by an effective mass  $m^*$  in the nuclear medium. The data are consistent with the choice of  $m^*=0.83m$  at 290 MeV and  $m^*=0.86m$  at 500 MeV [3]. The 10% deviation of effective mass from free nucleon mass represents about 25% deviation of analyzing power from free NN values in the case of  $^{208}\text{Pb}$ . Analyzing power angular distributions of the quasifree peak offer a sensitive way to observe relativistic medium effects. Further measurements with lighter target nuclei such as  $^{58}\text{Ni}$  will be useful to confirm the relativistic medium effects, because the multiple scattering will be reduced and the  $m^*/m$  will remain about the same [3]. For  $E_p = 290$  MeV to 500 MeV the  $^{209}\text{Pb}$  cross section spectra of the continuum are found to be quite well described by the non-relativistic impulse approximation such as free surface response model calculations [2].

The low-lying states can be reasonably well described by non-relativistic DWBA optical model calculations. The phenomenological Dirac optical model describes the 290-MeV data well but is less successful at 500-MeV. Further study extending the search of the Dirac optical model parameters are needed to improve the description of the low-lying states. Further investigations of the phenomenological Dirac optical model approach will also be very useful.

Table 7: Proton +  $^{208}\text{Pb}$  Relativistic Optical Model Parameters.

	300 (MeV)	500 (MeV)
$U_{\text{SR}}(\text{MeV})$	-367.997	-287.136
$R_{\text{SR}}(\text{fm})$	1.1238	1.2324
$a_{\text{SR}}(\text{fm})$	0.7104	0.6860
$W_{\text{SI}}(\text{MeV})$	64.270	40.839
$R_{\text{SI}}(\text{fm})$	1.2424	1.2179
$a_{\text{SI}}(\text{fm})$	0.6657	0.5047
$U_{\text{OR}}(\text{MeV})$	267.579	200.028
$R_{\text{OR}}(\text{fm})$	1.1281	1.1237
$a_{\text{OR}}(\text{fm})$	0.6818	0.6708
$W_{\text{OI}}(\text{MeV})$	60.261	-59.618
$R_{\text{OI}}(\text{fm})$	1.2363	1.1836
$a_{\text{OI}}(\text{fm})$	0.6733	0.5638

## Bibliography

- [1] G.R. Satchler, *Nucl. Phys.*, **A195**, 1(1972)
- [2] H. Esbenson and G.F. Bertch, *Phys. Rev.*, **C34**, 1419(1986)
- [3] C.J. Horriwitz and M.J. Iqbal, *Phys. Rev.*, **C33**, 2059(1986)
- [4] F.E. Bertrand, *Nucl. Phys.*, **A354**, 129c(1981)
- [5] D.A. Hutcheon, W.C. Olsen, H.S. Sherif, R. Dymarz, J. Cameron, J. Johanson, P. Kitching, P.R. Liljestrang, W.J. McDonald, C.A. Miller, G.C. Neilson, D.M. Sheppard, D.K. McDaniels, J.R. Tinsley, P. Schwaradt, L.W. Swenson, C.E. Stronach. *submitted to Phys. Re V.C*
- [6] L. Ray and G.W. Hoffmann, *Phys. Re V.*, **C31**, 538(1985)
- [7] D.K. McDaniels, J. Lisantti, I. Bergqvist, L.W. Swenson, X.Y. Chen, D.J. Horen, F.E. Bertrand, E.E. Gross, C. Glover, O. Häusser, K. Hicks. *Nucl. Phys.*, **A467**, 557(1987)
- [8] N.M. Hintz, D. Cook, M. Gazzaly, M.A. Francy, M.L. Barlett, G.W. Hoffmann, R. Fergerson, J. McGill, J.B. McClelland, K.W. Jones. *submitted to Phys. Re V.C*
- [9] T.De Forest, *Adv. in Phys.* **15**, 1(1966)
- [10] B.R. Whitney, I. Sick, J.R. Ficenece, R.D. Kephart, W.P. Trower. *Phys. Re V.*, **C9**, 2230(1974)
- [11] M.S. Wall and P.R. Rost *Phys. Re V.*, **150**, 811(1966)

- [12] J. Lisanntti, J.R. Tinsley, D.M. Drake, I. Bergqvist, L.W. Swenson, D.K. McDaniels, F.E. Bertrand, E.E. Gross, D.J. Horen, T.P. Sjoreen. *Phys. Lett.*, **B147**, 29(1984)
- [13] L.G. Arnold and B.C. Clark, *Phys. Rev.*, **C23**, 1949(1981)
- [14] R.D. Smith and J. Wambach, *submitted to Phys. Rev.*, C
- [15] E.L. Mathie, *TRIUMF Users Handbook*, p.IV-34, unpublished(1986)
- [16] K. Hicks, *MRS manual*, unpublished(1986)
- [17] F.E. Bertrand, E.E. Gross, D.J. Horen, R.O. Sayer, T.P. Sjoreen, D.K. McDaniels, J. Lisanntti, J. Tinsley, L.W. Swenson, J.B. McClelland, T.A. Carey, K. Jones, S.J. Seestrom-Morris. *Phys. Rev.* **C34**, 45(1986)
- [18] J. Raynal, private communications.
- [19] D.K. McDaniels, J.R. Tinsley, J. Lisanntti, D.M. Drake, I. Bergqvist, L.W. Swenson, F.E. Bertrand, E.E. Gross, D.J. Horen, T.P. Sjoreen, R. Liljestrand, H. Wilson. *Phys. Rev.*, **C33**, 1943(1986)
- [20] G.F. Bertsch and O. Scholtem, *Phys. Rev.* **C25**, 804(1982)
- [21] L.W. Swenson, X.Y. Chen, J. Lisanntti, D.K. McDaniels, I. Bergqvist, F.E. Bertrand, D.J. Horen, E.E. Gross, C. Glover, R.O. Sayer, B.L. Burks, O. Häusser, K. Hicks. *submitted to Phys. Rev.*, C
- [22] J. Lisanntti, F.E. Bertrand, D.J. Horen, B.L. Burks, C.W. Glover, D.K. McDaniels, L.W. Swenson, X.Y. Chen, O. Häusser, K. Hicks. *submitted to Phys. Rev.*, C